Dynamic and instabilities at soft interfaces

Maxence Arutkin

THÈSE DE DOCTORAT

de l'Université de recherche Paris Sciences et Lettres—
PSL Research University

Préparée à l'École supérieure de physique et chimie industrielle de la ville de Paris

Dynamique et instabilités aux interfaces molles

Ecole doctorale n°564
Physique en Île-de-France

Spécialité : Physique

COMPOSITION DU JURY :

Pr Jörg BASCHNAGEL
Université de Strasbourg
Président du jury

Pr Isabelle CANTAT
Université de Rennes
Rapporteur

Pr Anne TANGUY
INSA Lyon
Rapporteur

Dr Christophe CLANET
École Polytechnique
Membre du jury

Dr Élie RAPHAËL
ESPCI Paris
Directeur de thèse

Dr Thomas SALEZ
Université de Bordeaux
Examinateur

Dr Kay WIESE
École normale supérieure
Membre invité

Soutenue par Maxence ARUTKIN
le 05 décembre 2018

Dirigée par **Élie RAPHAËL**
et **Thomas SALEZ**

ESPCI PARIS | PSL

This doctoral dissertation is the outcome of my research in the *Gulliver* laboratory under the supervision of Élie Raphaël and Thomas Salez. Our work led to the writing of 4 papers.

UMR CNRS 7083
10, rue Vauquelin – 75231 Paris Cedex 5 – FRANCE

École Supérieure de Physique et de Chimie Industrielles de la Ville de Paris
& Paris Sciences et Lettres

Résumé

Dynamique des interfaces molles, des sillages hydrodynamiques aux anomalies de transitions vitreuses

Cette thèse se divise en deux parties, la première partie aborde la physique des sillages. Lorsqu' un objet se déplace à la surface d'un liquide des ondes sont générées et rayonnées. Lorsque l'objet se déplace à vitesse constante il résulte le fameux sillage en V de Kelvin qu'on peut observer derrière un bateau. Le rayonnement de ces ondes crée une force s'opposant au mouvement appelée resistance de vague. On établit ici la formule de Havelock de la résistance de vague pour un mouvement quelconque. Le sillage et la résistance de vague sont également étudiés en présence dâ un couplage élastohydrodynamique à l'interface. Enfin on termine avec l étude des vagues générées par une araignée d' eau lors de sa phase de propulsion.

Dans la seconde partie, on propose un modèle de chaines cooperatives en

s'inspirant de la loi empirique d'Adam et Gibbs pour la transition vitreuse. Ce modèle nous permet d'étudier des anomalies de transition vitreuse en milieu confiné notamment la réduction de temperature de transition vitreuse dans les nano-films et nanoparticules de polystyrène. Enfin on aborde des calculs de statistiques de chaines polymèriques en milieux confinés et leurs dépendances exactes dans le poids moléculaire.

Le premier chapitre est un chapitre introductif, on présente des propriétés élémentaires des vagues en eaux profondes. Après avoir établi la relation de dispersion des vagues $\omega = \sqrt{(gk)}$ on en discute ses propriétés essentielles. Cela permet ensuite de dériver les équations dynamiques de l'interface libre. On va s'intéresser plus loin au déplacement d'objet à la surface, ces objets seront modélisés par des champs de pression qui peuvent être mis en mouvement, en utilisant l'équation dynamique de l'interface libre, on peut determiner l'expression intégrale du déplacement de la surface du liquide dû au déplacement d'un champ de pression à sa surface. Cette équation est fondamentale dans l'étude des sillages et de la résistance de vague. On présente également la solution élémentaire de Cauchy-Poisson pour la surface, solution qui a permis historiquement à Kelvin de déterminer la forme mathématique du sillage. Ce chapitre permet également d'introduire le concept de résistance de vague : la perte d'énergie subit par un objet en déplacement à cause du rayonnement du sillage, en d'autres termes le coût en terme de force que va ressentir l'objet en déplacement à cause de la déformation qu'il crée à la surface. Havelock à établi une formule pour calculer cette force dans le cas du mouvement rectiligne, on établit ici que la formule de Havelock peut être généralisée a tout type de mouvement à la surface d'un fluide. On aborde aussi dans ce chapitre l'effet de la capillarité sur la relation de dispersion, et notamment l'existence

d'une vitesse de groupe minimale 23 cm.s^{-1} en deçà de laquelle une source ne rayonnerait pas d'énergie à la surface du liquide. Le mouvement circulaire d'une perturbation à la surface est également évoqué dans ce chapitre.

Le second chapitre étudie un type de sillage elasto-hydrodynamique, lorsqu'un fin film visqueux est couplé à une feuille élastique, plusieurs phénomènes intéressants peuvent apparaître, on observe notamment à la surface la génération d'ondes de surface. Historiquement l'étude des ondes elasto-hydrodynamique a été initié par l'étude des ondes générées par les avions atterrissant sur l'antarctique. Dans ce régime les ondes l'inertie du fluide domine. De nombreux résultats en mécanique des fluides peuvent être revisités, la montée capillaire, l'instabilité de Saffman-Taylor pour laquelle la présence d'une feuille élastique peut prévenir l'instabilité. Dans le domaine de la physique de la peinture, la propagation du front de pelage d'une feuille de plastique posée au-dessus d'une couche de glycérine. De plus, une force de portance agissant sur un objet en mouvement et interagissant via des forces hydrodynamiques a été prédite et confirmée expérimentalement. Des motifs rappelant le démouillage peuvent être observés lorsqu'une feuille élastique humide est en contact avec un substrat solide. Dans ce chapitre nous combinons physique du sillage et élasto-hydrodynamique, cette nouvelle classe de problèmes trouve des applications en géophysique, biophysique, propagation des ondes et en particulier pour la mesure à l'échelle nanométrique : la déformation des substrats modifie l'observation et la précision de ces expériences. Après avoir rappelé la théorie de la lubrification, nous établissons l'équation de la couche mince élasto-hydrodynamique, puis nous étudions le déplacement d'un champ de pression externe sur une feuille élastique mince recouvrant une couche mince visqueuse. Dans l'approximation de la lubrification, nous

calculons les ondes élasto-hydrodynamiques et le sillage, ainsi que la résistance aux ondes. Un équivalent du nombre de Bond où l'élasticité remplace la capillarité semble être un paramètre central sans dimension du problème et nous l'appelons le nombre de Bond élastique dans la suite. Le sillage élasto-hydrodynamique est tracé pour une large gamme de vitesses et de nombres de Bond élastiques. Nous fournissons des résultats analytiques asymptotiques pour la résistance aux ondes à basse et haute vitesse. Finalement, nous montrons que l'énergie transférée par la perturbation du fluide est entièrement dissipée par la viscosité.

Dans le dernier chapitre de la première partie, nous étudions à la fois théoriquement et expérimentalement le modèle de vague généré par les coups de patte de l'araignée d'eau. Nous verrons d'abord que le cycle de propulsion est divisé en trois phases. Ensuite, nous nous concentrons sur la première phase, l'impulsion, avec un modèle théorique et nous comparons notre prédiction à des mesures expérimentales. Grâce à l'utilisation de la méthode synthétique de Schlieren, nous pouvons mesurer avec précision la réponse dynamique de la surface libre. Plusieurs espèces d'insectes et d'arachnides exploitent les déformations statiques et dynamiques de l'eau pour vivre à l'interface air-eau. Les marcheurs d'eau sont parmi les insectes les plus connus existant à l'interface air-eau. Ce sont les insectes les plus étudiés en matière de locomotion dans un tel habitat, et notamment en raison de leur capacité à sauter en l'air en utilisant la surface de l'eau comme trampoline. Ils sont également de plus en plus utilisés comme modèle pour les micro-robots. On sait que le déplacement d'une perturbation à la surface crée un motif d'onde complexe. Les vagues et les tourbillons créés par les araignées d'eau sont la signature de l'impulsion appliquée à l'eau. Les études théoriques sur les vagues et les tourbillons ont fait de grands progrès pour les araignées d'eau. Cependant, il n'est toujours pas tranché si les

ondes de surface sont plus importantes que les vortex dans le transfert de l'impulsion donnée par la patte de l'insecte à l'eau. Le côté expérimental s'appuie principalement sur des mesures PIV (Vélocimétrie par imagerie de particules) de la surface de l'eau. Nous avons également filmé l'animal de côté, obtenant ainsi une estimation approximative du creux du ménisque. Ce chapitre quantifie avec une précision inégalée (résolution de 5μm) les déformations de la surface de l'eau lors du choc de la patte de l'araignée d'eau afin de comprendre l'importance de rendre compte des détails de l'interaction fluide-structure au cours de l'impulsion. Une étape supplémentaire au modèle de forçage impulsif proposé Bühler, où l'impulsion est localisée dans le temps et dans l'espace. Nous étendons aussi la théorie de Bühler aux eaux peu profondes et à un forçage continu (non impulsif). Ces travaux permettent une meilleure compréhension de la locomotion à l'interface air-eau, des trains d'ondes de faible amplitude sont utilisés par de nombreux insectes vivant à la surface de l'eau.

La seconde partie de la thèse, divisé également en trois chapitres, traite de la transition vitreuse et en particulier aux effets observés de la transition vitreuse dans des verres de polymères en milieux confinées. Pour décrire ces effets expérimentaux, un modèle de chaine coopérative a été étudié dans le détail. Les verriers ont longtemps su que lors du refroidissement de liquides à base d'oxydes, la viscosité évolue pour faire un verre. Une convention permettant la distinction entre un liquide et un solide amorphe vitreux a été adopté, Tammann a appelé cette température de transition Tg la température de transition vitreuse et correspondent à un liquide de viscosité 1012 Pa.s. Il est maintenant bien établi que, autour de Tg, de nombreux produits chimiques en phase condensée comme le glycérol, les polymères, les oxydes ou encore les métaux ont la même augmentation spectaculaire

de viscosité mais aussi des modifications physiques similaires spécifique à l'état vitreux. Bien que l'obtention d'un verre par refroidissement rapide soit assez simple, il a été jusqu'à présent impossible de comprendre pleinement la transition vitreuse d'un point de vue théorique. Les principales raisons sont que les propriétés dépendent de la façon dont le verre a été fabriqué, et ces propriétés évoluent avec le temps. C'est le phénomène de vieillissement.

Dans le premier chapitre de cette partie, nous rappelons les propriétés physiques des liquides et des verres surfondus. Ensuite nous introduisons des lois phénoménologiques telles que les lois d'Adam et Gibbs ou Vogel-Fulcher-Tammann exprimant le temps de relaxation en fonction de la température, ainsi que des théories comme la théorie des volumes libres. Ces théories proposent une forme mathématique empirique au temps de relaxation ou à la viscosité d'un liquide surfondu. On observe notamment qu'à la différence de la loi d'Arrhenius qui prédit une divergence de la viscosité à température nulle, ces lois empiriques diverges à une température finie supérieure à 0K, à une température appelée la température de Vogel du verre, cette température est typiquement 50 degrés en dessous de la température de transition vitreuse définie plus tôt. Le modèle simplifié de chaines coopératives permet de retrouver ces lois expérimentales. De nombreuses simulations numériques ainsi que des observations sur les matériaux granulaires suggèrent que dans un liquide surfondu les molécules sont dans un milieu encombré et que les déplacements se font par des mouvements collectifs. Ces mouvements collectifs peuvent notamment prendre la forme de chaines coopératives aléatoires où plusieurs molécules se déplacent simultanément le long d'une trajectoire libérant ainsi de l'espace permettant la relaxation au sein du liquide surfondu. Le nombre de molécule nécessaire à la relaxation dépend de la densité du milieu, au plus le milieu est

dense au plus les chaines coopératives devront être longues. On peut relier la densité à la température dans un liquide surfondu grâce au coefficient de dilatation du milieu obtenant ainsi la taille des chaines coopératives nécessaire à la relaxation en fonction de la température du milieu. Enfin en invoquant l'ergodicité on peut obtenir le temps nécessaire pour former une chaine coopérative relaxante et finalement le temps de relaxation moyen de ces chaines coopératives, qui est une fonction de la température. Avec ce modèle on retrouve les temps de relaxation phénoménologiques d'Adam et Gibbs et de Vogel-Fulcher-Tammann. Dans le second chapitre de cette partie on utilise ce modèle au cas des verres en milieu confiné, notamment les films minces et les nano-sphères de polystyrène. L'existence de chaînes coopératives d'une certaine longueur nécessaire à la relaxation pose naturellement la question suivante : Qu'observe-t-on lorsque le système étudié a une taille identique ou inférieure à la taille de ces chaines de relaxation ? De nombreuses expériences notamment utilisant des nanofilms de polystyrène ont montré qu'à partir d'une certaine taille, on observait une forte chute de la température de transition vitreuse. Cette température de transition étant constante dans un matériau de taille infinie, elle dépend fortement de la taille de l'objet lorsque celui-ci est proche ou inférieure à celle des chaines coopératives impliquée dans le processus de relaxation. Pour comprendre ce phénomène prenons le cas d'un film mince, une molécule proche de la surface libre, elle peut se déplacer soit via une chaine coopérative de la taille précédemment évoquée, ou bien faire partie d'une chaine coopérative tronquée par la présence de la surface libre, ces chaines tronquées permettent une relaxation plus rapide du liquide surfondu et par conséquent au plus le film est mince au plus il y a de chaines coopératives tronquées et au plus la relaxation dans le film est rapide. On obtient donc une viscosité ou un temps de relaxation dépendant de la taille de l'échantillon étudié. Ce modèle simple permet avec un bon

accord les résultats expérimentaux observées dans les nano-films. Le cas des nano-sphères présentent des résultats expérimentaux plus disparates, probablement dus à la fabrication difficilement contrôlable de ces objets à la différence des nano films dont la préparation est plus simple. Cependant on observe un certain accord entre les prédictions de notre modèle et les résultats expérimentaux.

Des expériences ont été menées sur les films minces suspendus (avec donc deux interfaces libres) de polystyrènes en faisant varier le poids moléculaire de ce dernier. Il a été observé que pour des petits poids moléculaire la température de transition vitreuse était indépendante du poids moléculaire et vérifier donc une dépendance en la taille de l'objet comme étudié dans le chapitre précédent en revanche au delà d'un certain poids moléculaire (514K) on observe une forte dépendance dans le poids moléculaire. Dans ce régime, la dépendance en h la taille du film devient linéaire avec une pente proportionnelle au logarithme du poids moléculaire. Ces observations suggère qu'à haut poids moléculaire un autre processus de relaxation est à l'œuvre et qu'il est d'origine polymérique. Autre observation frappante de ces expériences est que si l'on trace plusieurs courbes de température de transition vitreuse en fonction de la hauteur du film, pour plusieurs poids moléculaire les droites obtenues se croisent toute en un point faisant apparaître une hauteur et un poids moléculaire caractéristiques. Par ailleurs il faut rappeler que ces expériences ont été réalisé sur des films auto supportés avec donc deux surfaces libres, lorsque le film est sur un substrat solide, et qu'il n'y a plus qu'une seule surface libre, nous n'observons plus ce comportement pour la température de transition vitreuse. Toutes ces remarques suggèrent donc un processus de relaxation d'origine polymérique connectant deux interfaces libres. De Gennes a proposé un modèle simplifié pour expliquer ces observations. Le processus de relaxation proposé repose

sur la diffusion du volume libre le long d'une même chaîne polymérique reliant les deux interfaces, ce modèle fait intervenir à la fois un temps de relaxation élémentaire ici celui de Vogel-Fulcher-Tammann, ainsi que la statistique des chaines reliant les deux interfaces. En supposant une répartition gaussienne du volume libre le long de la chaine, on obtient ainsi un temps moyen de relaxation dépendant à la fois de la taille du substrat et du poids moléculaire. De Gennes avait d'abord proposé un « scaling », a haut poids moléculaire on retrouvait bien une dépendance linéaire en h toutefois le « scaling » ne permettait pas de trouver une dépendance dans le poids moléculaire. Nous avons donc calculé de manière précise les statistiques des chemins à l'intérieur d'un même polymère reliant les deux surfaces libres donnant ainsi la probabilité de trouver des segments de tailles L reliant les deux interfaces distantes d'une longueur h, permettant de donner ainsi une forme analytique au temps de relaxation moyen de ce processus. On observe cependant que pour un très fort confinement ($h \to 0$) ou un poids moléculaire tendant vers l'infini, la taille de ces ponts reliant la surface tend vers h^2, perdant ainsi la dépendance dans le poids moléculaire, ce qui est en désaccord avec les observations expérimentales. Ceci suggère donc que si le mécanisme proposé par De Gennes est le bon, il manque un ingrédient physique fortement dépendant du poids moléculaire à introduire dans ce modèle et qu'il ne vient pas des statistiques des ponts polymériques. Enfin il faut aussi mentionner ici que ces expériences faites avec des hauts poids moléculaires ont soulevé plusieurs controverses dues à la préparation des films réalisés à l'aide de solvant et utilisant la méthode de « spin-coating », il se pose naturellement la question de l'équilibre thermodynamique des chaines de polymère après une telle préparation.

Mots-clés Films minces, transition vitreuse, vagues, résistance de vague.

Abstract

Dynamics of soft interfaces, from hydrodynamics wakes to glass transition anomalies

This thesis is divided into two parts. In the first part, we study several properties of waves at the surface of a liquid ; in particular the wake generated at the interface by an object modelled by a pressure field. When an object with constant speed moves atop the surface, it generates a wake. The radiation of these waves results in a loss of energy for the operator putting the object in motion, which results in a resultant force opposite to the motion called the wave resistance, calculated by the Havelock formula. In the stationary regime, we propose here a demonstration of the Havelock formula for any movement on the surface. The wake and wave resistance are also studied using elastohydrodynamic coupling at the surface. We then model the waves generated by a water strider during its propulsion phase.

In the second part, we propose a model of cooperative strings inspired by the empirical law of Adam and Gibbs for the glass transition. This model allows us to study glass transition anomalies in a confined environment, in particular the reduction of glass transition temperature in thin films and nanoparticles of polystyrenes. Finally, we consider calculations of chain statistics in confined environments and their exact dependencies on molecular weight.

Keywords Thin films , glass transition, water waves, wave resistance.

Contents

Introduction

The chapters of this manuscript are provided with specific introductions, we here present a very general introduction to soft matter, water waves, polymers and diffusion.

1 Soft Matter

P.-G. de Gennes is considered the inventor of the science baptised soft matter. After a start in solid physics (magnetism, superconductivity), his career in theoretical physics of condensed matter have led way to a very wide spectrum of subjects: liquid crystals, polymers, colloids, wetting and adhesion, biophysics and neuroscience that make up soft matter physics today. Although the list of his works is very wide, the importance of his work rests especially on his research style, in constant contact with experience and the industrial world, and based on the idea that all physical phenomena can be explained in simple terms. His work was awarded by the Nobel Prize in Physics in 1991.

Soft materials are also called complex fluids, coming from the study of liquids made of simple atoms or molecules, these studies include polymers, surfactants, liquid crystals as well as colloidal dispersions. These materials have a certain flexibility or even fluidity. In polymer physics, if we go to the microscopic scale, we see a system of long, flexible and independent polymer chains. The oxygen in the air creates bridges between the chains, inducing a dramatic change of state, where we go from a liquid to a cross-linked network that resists stress: a rubber. A simple chemical operation brought a radical change in mechanical properties, and this is a characteristic feature of soft matter. Disorder characterises soft matter. Let's illustrate this property with two examples: First, liquid crystals have, just like crystals, an orientation order. On the other hand, the centres of gravity of the molecules which constitute them present a disorder of position and they flow like liquids. Then the polymers are often compared to an entangled spaghetti dish subjected to thermal agitation, the long chains sneaking by, crawling among the others. The common point to all systems of soft matter, which can serve as a definition, is that the interaction energies involved between objects (H bonds, Van der Waals interactions, etc ...) are comparable to the heat energy kT at room temperature. As the enthalpic effects are of the same order of magnitude as the entropic effects, the systems are likely to reorganise strongly under the effect of weak variations of the environment (temperature, pressure, concentration) or of weak external stresses (mechanical stress, electromagnetic

Figure 1 Old glass making technics: glass blowing.

field, etc.). Because of the large number of scales involved (energetic, spatial, temporal), the physics of soft matter is therefore intermediate between the physics of liquids and the physics of solids. Because of the complexity of the systems, the exploration of the phase space is often done in several distinct stages and can vary very strongly between two systems that are very similar from the point of view of composition. The equilibrium of the systems then has several characteristic times and can vary over several time decades to reach extremely slow times, greater than the second, in some cases. Since the enthalpic effects are of the same order as the entropic effects, it also happens that the systems remain kinetically trapped in minima during the exploration of the phase space and remain out of equilibrium. This is the case of colloidal suspensions, which vitrify at high concentration and serve as model systems for understanding the mechanisms of the glass transition.

2 Waves

The first part of this thesis deals with the disturbance created at a liquid interface, the locomotion of water strider due to the surface tension as well as elasto-hydrodynamic coupling at interface. This part is linked to the theory of water waves, which has been a source of inspiration for physicists and mathematicians for almost two centuries. The first to have derived the equation of water waves is Joseph-Louis Lagrange. Since then, countless situations have been studied, such as finite depth, uneven bottom or tidal waves. Advances in the field followed the development of mathematical tools such as Fourier analysis. Other physicists and mathematicians who contributed to the physics of water waves are Laplace, Airy, Stokes, Rayleigh,, Boussinesq, Saint-Venant or Kelvin. By looking at a duck swimming in a lake or a ship moving on a sea, one can clearly say that there is something similar about their wake. They both show a familiar V-shaped pattern. Lord

Kelvin was able to provide a theory to explain the ship-wave pattern. One of his popular achievement was to show that the wake created by a disturbance moving at a uniform pace is always delimited by a straight wedge with half-angle $\phi_K = \arcsin 1/3 \simeq 19.5°$, independent of the velocity of the disturbance. In order to explain the complex wave pattern within the wake, Kelvin developed the stationary phase method. Havelock [1] exploited Kelvin's idea that the disturbance may be replaced by a succession of impulses along the trajectory.

Figure 2 Water strider staying above water surface due to surface tension.

3 Polymers

The second part deals with the modified dynamic at interfaces for polymer supercooled liquids and glasses, as well as polymer conformation in confined geometries. A polymer is a long chain constructed by the repetition of smaller units - monomers - through covalent bounds. The repetition number is up to 10^5 for synthetic polymers and up to 10^8 for DNA in nature. Natural polymers such as wood, cotton (cellulose) have been used by human for millenaries. The first industrial process using synthetic polymers is the invention of the caoutchouc by Goodyear in 1839. Material composed of these long molecules can show completely different behaviour from material with only the monomer unit ; often these materials are flexible like rubber and can easily form thin films or fibres. From a theoretical point of view, de Gennes and Edwards have made many advances in the modelling of polymers and polymer materials, from static description to dynamic models.

First part

—

Surface waves

Chapter 1

Wake and wave resistance

Chapter 1 : Wake and wave resistance

↑ back to contents

Chapter abstract

A moving disturbance at the surface of water generates a complex wave pattern due to the dispersive property of the medium. Within linear wave theory, we derive the dispersion relations for pure gravity and capillary-gravity waves, then we solve this equation for several trajectories. We discuss Kelvin's theory of wave patterns, focusing notably on the so-called Kelvin wedge, as well as the stationary phase method to obtain the wave crests.

Finally we define the concept of wave resistance, the force acting against the motion of a boat due to wave radiation, and we detail its expression for multiple trajectories.

1.1 Introduction

A boat moving at the surface of the sea generates water waves. These waves can be very complex and irregular at first sight, however the most common type of motion describing the propagation of waves at the water surface are sinusoidal waves. On average, the water surface is plane, however there are waves moving at the surface. If we consider a given point, the water is alternately at the top or the bottom of the waves. As a first approximation, the water is considered incompressible and by the conservation of matter we conclude that a particle at the surface cannot move up and down without violating these assumptions. In fact, at the surface the particle moves in approximate circles. This is also the case deeper, although with radius decreasing with depth.

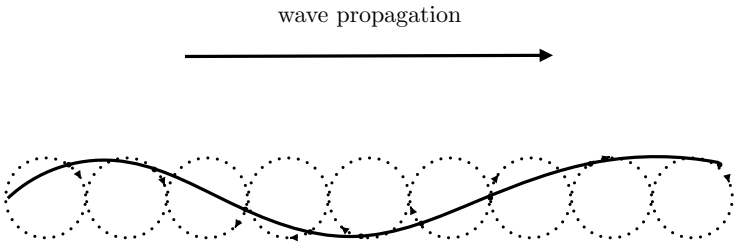

Figure 1.1 Circular motion of the particles at the water surface.

Water waves in infinite depth cannot depend on any depth length, therefore the phase velocity of a wave only depends on gravity:

$$v_\phi = \sqrt{\frac{g\lambda}{2\pi}} \ , \tag{1.1}$$

it is notable that long waves go faster than short ones. Therefore if a boat makes waves of various wavelengths, as time goes, the waves observed at a point will become shorter and shorter. In fact to arrive to this conclusion, we should look at the group velocity and we can show for water waves that it is half of the phase velocity, therefore it too will behave as the square root of the wave length. It means that the interior of a wave packet moves at v_Φ but the enveloppe containing said waves moves at half this speed.

To understand the meaning of phase velocity and group velocity, we will consider a harmonic plane wave. Such a wave can be described mathematically by a cosine:

$$\theta_1(x,t) \quad = \quad \theta_0 \cos\left(\omega_1 t - k_1 x\right) \ , \tag{1.2}$$

this signal has no physical reality since it has a infinite spatial extent and infinite lifetime. However a real wave can be expressed as a superposition of these harmonic waves. Let's

consider a sum of two harmonic plane waves with a different pulsation. The resultant waves read:

$$\theta(x,t) = 2\theta_0 \cos\left(\frac{\Delta k}{2}\left(\left(\frac{\mathrm{d}\omega}{\mathrm{d}k}\right)_{k_0} t - x\right)\right)\cos\left(\omega_0 t - k_0 x\right) , \tag{1.3}$$

this wave is modulated in amplitude, $\cos(\omega_0 t - k_0 x)$ is a wave varying rapidly in space and time and its velocity is the phase velocity v_ϕ; $\cos\left(\frac{\Delta k}{2}\left(\left(\frac{\mathrm{d}\omega}{\mathrm{d}k}\right)_{k_0} t - x\right)\right)$ is a wave varying slowly in space and time and its velocity is the group velocity $v_g = \left(\frac{\mathrm{d}\omega}{\mathrm{d}k}\right)_{k_0}$. If we consider a more complex wave packet:

$$\theta(x,t) = \frac{\theta_0}{\Delta k}\int_{-\frac{\Delta k}{2}}^{\frac{\Delta k}{2}} \mathrm{d}k e^{i(\omega(k)t - kx)} , \tag{1.4}$$

one can develop the dispersion relation:

$$\omega(k) = \omega_0 + v_g \delta k + \frac{1}{2}\left(\frac{\mathrm{d}^2\omega}{\mathrm{d}k^2}\right)\delta k^2 , \tag{1.5}$$

therefore the wave-packet takes the following form:

$$\theta(x,t) = \frac{\theta_0}{\Delta k} e^{i(\omega_0 t - kx)}\int_{-\frac{\Delta k}{2}}^{\frac{\Delta k}{2}} \mathrm{d}k e^{i\delta k(v_g t - x)} e^{i\frac{1}{2}\left(\frac{\mathrm{d}^2\omega}{\mathrm{d}k^2}\right)\delta k^2 t} , \tag{1.6}$$

we observe that if the group velocity were independent of k, the enveloppe of the waves would be stationary. However in the complex case of surface waves, the wave packet is deformed. If a wave packet has a size of Δx_0 at $t = 0$, it will have at time t a size $\Delta x(t) = \Delta x_0 + \left(\frac{\mathrm{d}^2\omega}{\mathrm{d}k^2}\right)\Delta k t$. Water waves have all these characteristics.

It is fundamental to understand the water wave pattern. Since the group and phase velocities are no longer the same, the waves produced are no longer a cone, as in the case of sound waves in the air or light in the vacuum. The wave pattern created is much more complex. Everyone recognizes the specific V-shape of a moving disturbance at a constant speed over the water. For a duck swimming or a cargo moving in the ocean, we observe the same pattern with a constant angle. This entire pattern of waves can be analyzed knowing that the phase velocity goes like $\sqrt{\lambda}$. And instead of having wavefronts along a cone, we obtain this beautiful pattern, with fronts moving parallel to the motion of the boat, as well as wave fronts on either side at other angles.

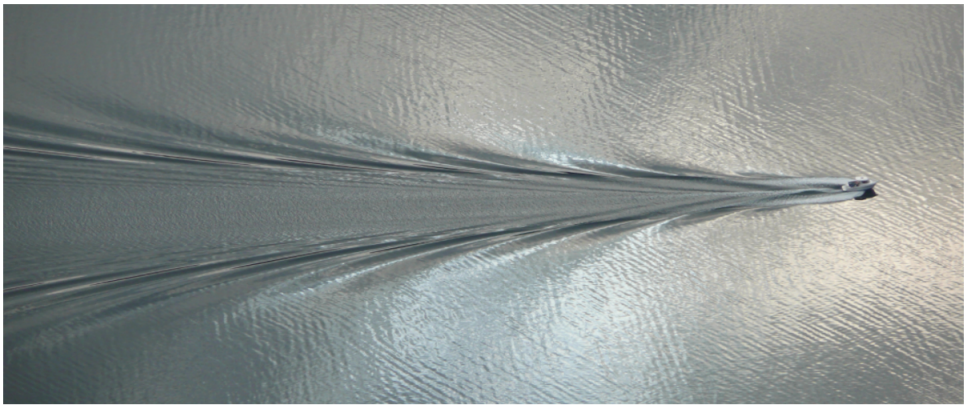

Figure 1.2 The universal V-shape pattern of a moving disturbance at the water surface.

1.2 Waves equation

In this section we establish the dynamical equation for water waves with infinite depth within the framework of *linear wave theory*, we discuss the effect of capillarity and eventually we give the surface displacement solution in presence of a moving disturbance at the surface. These basic concepts are widely discussed in many references [2, 3, 4, 5, 6].

1.2.1 Deep water gravity waves

The free surface of a liquid in equilibrium under the action of gravity is a plane. If a boat disturbs the surface, it moves from equilibrium and motion will appear in the liquid. This perturbation will be propagated at the surface as waves, the gravity waves. We consider an incompressible, inviscid and infinite deep water volume, delimited by a free surface in the plane $z = 0$. We define $\zeta(\boldsymbol{r}, t)$ to be the displacement from the equilibrium position (i.e. the plane $z = 0$). We take the $z-$axis vertically upwards. The assumption of irrotational flow results in a number of simplifications of great utility. The fact that $\boldsymbol{\nabla} \wedge \boldsymbol{v} = \boldsymbol{0}$ ensures the existence of a volocity potential $\varphi(\boldsymbol{r}, z, t)$ such as:

$$\boldsymbol{v} \;=\; \boldsymbol{\nabla}\varphi \;, \tag{1.7}$$

where $\boldsymbol{v}(\boldsymbol{r}, z, t)$ is the velocity field in the liquid. Incompressibility ensures that the continuity equation is reduced to:

$$\boldsymbol{\nabla} \cdot \boldsymbol{v} \;=\; 0 \;, \tag{1.8}$$

combining incompressibility with Eq. (1.7), the differential equation to be satisfied by the velocity potential is of course the Laplace equation:

$$\Delta\varphi \;=\; 0 \;, \tag{1.9}$$

where Δ is the Laplace operator. We shall consider waves on an unlimited water surface and we suppose that the wavelength is small in comparison with the depth of the liquid. The boundary condition at the sides and the bottom shall be omitted. Since the wave amplitude is assumed to be small, the displacement of the surface ζ is small. Under the same approximation we shall say that the vertical component of the velocity of the surface points is the time derivative of ζ:

$$\partial_t \zeta \;=\; \partial_z \varphi\big|_{z=0} \;, \tag{1.10}$$

this equation is known as the kinematic condition on the free surface. If we consider that the amplitude of the oscillations in the waves is small compared to the wavelength, the term $(\boldsymbol{v}\cdot\boldsymbol{\nabla})\boldsymbol{v}$ may be neglected: considering a harmonic mode with amplitude a gives that the ratio of the two terms in the material derivative of the Euler equation reads: $|(\boldsymbol{v}\cdot\boldsymbol{\nabla})\boldsymbol{v}|/|\partial_t \boldsymbol{v}| \sim [(a\omega)^2/\lambda]/(a\omega^2) = a/\lambda \ll 1$. Together with another consequence of the irrotational character of the flow, it leads to the important dynamical equation called *Bernoulli's law* for points located at the free surface:

$$\partial_t \varphi + \frac{1}{2}|\boldsymbol{v}|^2 + \frac{p}{\rho} + g\zeta \;=\; 0 \;, \tag{1.11}$$

where p is the pressure field at the surface, g the gravity. In the linear theory of waves, since the surface displacement is small, we can neglect as well the term in $|\boldsymbol{v}|^2$. Combining the kinematic boundary condition and *Bernoulli's law* one gets an equation on the potential at the free surface. Thus we have the following system of equations that determine the motion of the fluid inside the gravitational field:

$$\Delta_{\boldsymbol{r}} \varphi \;=\; 0 \;, \tag{1.12}$$

$$\left(\rho \partial_t^2 \varphi + \rho g \partial_z \varphi\right)_{z=0} \;=\; 0 \;. \tag{1.13}$$

To illustrate the properties of the water waves, let us consider gravity waves propagating in the x direction and uniform in the y axis. With these assumptions one can easily gets the following solution which decreases inside the liquid $z \to -\infty$:

$$\varphi(x,z,t) \;=\; A e^{kz} \cos\left(kx - \omega t\right) \;, \tag{1.14}$$

where ω is called the circular frequency and k is the wave number. And satisfying the boundary condition Eq. (1.13) we obtain the dispersion relation for the gravity waves:

$$\omega^2 \;=\; kg \;. \tag{1.15}$$

Therefore in the case of pure gravity waves the phase velocity is :

$$v_\phi \;=\; \sqrt{\frac{g}{k}} \;. \tag{1.16}$$

and the group velocity is:

$$v_g = \frac{1}{2}\sqrt{\frac{g}{k}} . \tag{1.17}$$

We observe that the group velocity is exactly half the group velocity. Let us mention here that the case of finite depth h will be treated in a further chapter on biolocomotion. It is interesting to see from Eq. (1.14) that the velocity of the particle inside the fluid decreases as we go deeper in the liquid. From the velocity potential one gets the trajectory of particles inside the fluid:

$$x - x_0 = -A\frac{k}{\omega}e^{kz_0}\cos(kx_0 - \omega t) , \tag{1.18}$$

$$z - z_0 = -A\frac{k}{\omega}e^{kz_0}\sin(kx_0 - \omega t) . \tag{1.19}$$

as mentioned in the introduction, the fluid particles move in a circle with raidus decreasing exponentially with depth after a surface perturbation.

1.2.2 Capillary-gravity waves

Fluid surfaces tend to have an equilibrium shape, under the gravitational field as well as the surface tension force when the wavelength of the perturbation reaches a size similar to the capillary length $\kappa = \sqrt{\frac{\gamma}{\rho g}}$. In the presence of gravity and capillarity, and assuming that the curvature of the interface remains small, the pressure at the interface reads:

$$p = p_0 + \rho g\zeta - \gamma\Delta\zeta , \tag{1.20}$$

where p_0 is the atmospheric pressure, ρ is the density of the liquid, g is the acceleration of gravity, and γ is the surface tension of the interface. *Bernoulli's law* combined with the kinematic boundary condition Eq. (1.11) leads to:

$$\left(\partial_t^2\varphi + \rho g\partial_z\varphi - \gamma\partial_z\Delta\varphi\right)_{z=0} = 0 , \tag{1.21}$$

where $\Delta = \partial_x^2 + \partial_y^2$, and where we have used the kinematic boundary condition of Eq. (1.10). Eventually, letting Eq. (1.14) into Eq. (1.21), one obtains the dispersion relation for capillary-gravity waves with infinite depth:

$$\omega(k) = \sqrt{gk + \frac{\gamma k^3}{\rho}} , \tag{1.22}$$

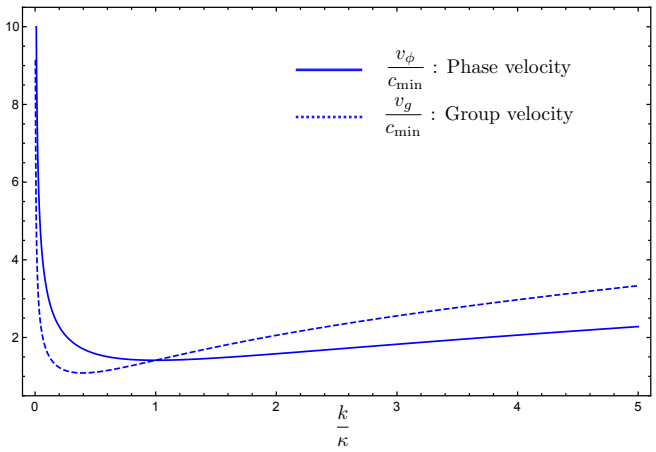

Figure 1.3 Dispersion relation for capillary gravity waves, we plotted the phase and the group velocity. At large wave number it is capillary branch whereas at small wave number it is the gravity branch. The most striking effect of the capillarity is the existence of a minimum in the dispersion relation.

where $v_\phi = \omega/k$ is the phase velocity. Surprisingly, the phase velocity for capillary-gravity waves has a minimum value:

$$c_{\min} = \left(\frac{4g\gamma}{\rho}\right)^{1/4} \sim 0.23 \text{ cm.s}^{-1} , \tag{1.23}$$

reached at $k = \kappa$, where $\kappa^{-1} = \sqrt{\gamma/(\rho g)}$ is the capillary length (see Fig. 1.3). This indicates that there are two possible values of k for any prescribed value of the phase velocity above $c_{\min}$.

1.3 Wake solution

In this section our aim is to provide the well known wake solution for a linear trajectory at constant speed the straight uniform wake, then the interesting case of the circular uniform wake which explains the spiral wake of the whirling beetles, and eventually the general wake solution for any trajectories.

1.3.1 Straight uniform wake

One of the most beautiful phenomena observed at the water surface is the pattern produced by a boat or any moving object at constant speed at the surface. Surprisingly the wave pattern is always the same, at least far away from the disturbance. The first explanation for this pattern was given by Lord Kelvin. But before going back to Kelvin's explanation, we are going to establish here the general form of the surface displacement.

In this part we theoretically investigate the wave pattern created by a ship moving at the surface of an inviscid and irrotational fluid, of constant and uniform density ρ, extending infinitely in the x and y directions. We also suppose the fluid to be infinitely deep, a very common assumption. In fact, assuming that the depth is much greater than the horizontal dimensions of the boat or the wavelengths involved in the wake pattern is sufficient. We model the presence of the ship by a supplementary pressure field $P_{\text{ext}}(\boldsymbol{r}, t)$ applied on the fluid from above, in addition to the atmospheric pressure P_0. The results presented hold in a linearized theory: the waves are supposed to be of small amplitude on a fluid initially at rest, so that every second-order term involving the velocity field $\boldsymbol{v}$ or the surface elevation ζ can be neglected. This enables us to make an extensive use of the Fourier transform. We then parametrize the ship's motion by a function $\boldsymbol{r_0}(t) = Vt\boldsymbol{e_x}$. We denote by V the velocity of the ship at the surface of the fluid. Since the ship is moving, the pressure field at time t can be described simply:

$$P_{\text{ext}}(\boldsymbol{r}, t) = P_{\text{ext}}(\boldsymbol{r} - Vt\boldsymbol{e_x}), \tag{1.24}$$

where $P_{\text{ext}}(\boldsymbol{r'})$ is the pressure field in the comoving frame of the boat. By the properties of the Fourier transform under variable translation, we deduce:

$$\hat{P}_{\text{ext}}(\boldsymbol{k}, t) = \hat{P}_{\text{ext}}(\boldsymbol{k}) e^{-ik_x Vt}. \tag{1.25}$$

With the 2D Fourier transform defined as:

$$\hat{f}(k_x, k_y) = \iint_{-\infty}^{+\infty} f(x, y) e^{-i(k_x x + k_y y)} \mathrm{d}y \mathrm{d}x \ , \tag{1.26}$$

$$f(x, y) = \frac{1}{4\pi^2} \iint_{-\infty}^{+\infty} \hat{f}(k_x, k_y) e^{i(k_x x + k_y y)} \mathrm{d}k_x \mathrm{d}k_y \ , \tag{1.27}$$

Using the Fourier transform on Eq. (1.21) and Eq. (1.10) we obtain a differential equation on the Fourier transform of the surface displacement:

$$\partial_t^2 \hat{\zeta}(\boldsymbol{k}, t) + \omega(k)^2 \hat{\zeta}(\boldsymbol{k}, t) = -\frac{1}{\rho} k \hat{P}_{\text{ext}}(\boldsymbol{k}) e^{-ik_x Vt}. \tag{1.28}$$

Its worth noticing that the dispersion relation $\omega(k)$ can be for gravity or capillary-gravity waves. In the comoving frame, the wake is stationary. Therefore the Eq. (1.28) is simply reduced to:

$$\hat{\zeta}(\boldsymbol{k}) = -\frac{k \hat{P}_{\text{ext}}(\boldsymbol{k})}{\rho \omega(k)^2 - k_x^2 V^2} \ , \tag{1.29}$$

therefore inverting the Fourier transform in the frame of reference of the moving boat, the stationary surface displacement reads:

$$\zeta(\boldsymbol{r}) \quad = \quad -\iint \frac{\mathrm{d}^2\boldsymbol{k}}{4\pi^2\rho}\frac{\hat{P}_{\mathrm{ext}}(\boldsymbol{k})e^{i\boldsymbol{k}\cdot\boldsymbol{r}}}{\omega(k)^2-k_x^2V^2} \tag{1.30}$$

This integral is ill-defined, the poles of the integrand are on the domain of integration. This ambiguity can be removed by imposing a radiation condition that there are no waves coming from infinity. A both mathematical and numerical method equivalent to this procedure is to consider that the amplitude of the disturbance has increased slowly for $t \in [-\infty, 0]$:

$$P_{\mathrm{ext}}(\boldsymbol{r},t) \quad = \quad e^{\epsilon t}P_{\mathrm{ext}}(\boldsymbol{r}) \ , \tag{1.31}$$

the amplitude of the pressure disturbance in the moving frame, where $\epsilon \to 0$. This procedure will shift the poles as in the presence of viscosity. The surface displacement is therefore completely defined by the following integral:

$$\zeta(\boldsymbol{r}) \quad = \quad -\lim_{\varepsilon\to 0}\iint \frac{\mathrm{d}^2\boldsymbol{k}}{4\pi^2\rho}\,\frac{k\hat{p}_{\mathrm{e}}(\boldsymbol{k})\,e^{i\boldsymbol{k}\cdot\boldsymbol{r}}}{\omega(k)^2-V^2k_x^2+2i\varepsilon Vk_x} \ . \tag{1.32}$$

This procedure is very important to numerically plot the wake, and will be applied in the following chapters.

1.3.2 Circular uniform motion

In this section, we derive the wave pattern created by a disturbance that has been moving for an infinitely long time at constant speed $V = R\Omega$ along a circle centered on 0 and of radius R therefore:

$$\boldsymbol{r}_0(t) = R\begin{pmatrix}\cos(\Omega t)\\ \sin(\Omega t)\end{pmatrix}. \tag{1.33}$$

Using Eq. (1.28) which involves the Fourier transform of ζ. The pressure field is supposed axisymmetric. Under this hypothesis, one gets:

$$\partial_{t^2}\hat{\zeta}(\boldsymbol{k},t)+\omega(k)^2\hat{\zeta}(\boldsymbol{k},t) = -\frac{1}{\rho}k\hat{P}_{ext}(k)e^{-i\boldsymbol{k}\cdot\boldsymbol{r_0}(t)}. \tag{1.34}$$

The right-hand side of this equation displays a periodicity with circular frequency Ω. Therefore in order to solve this equation, we will expand in Fourier series both the right-hand side and the solution. We set for a given wave vector $\boldsymbol{k}$, the angle θ between $\boldsymbol{k}$ and (Ox). Since $\boldsymbol{k}\cdot\boldsymbol{r_0}(t) = kr\cos(\theta-\Omega t)$, it yields:

$$e^{-i\boldsymbol{k}\cdot\boldsymbol{r}_0(t)} \quad = \quad \frac{1}{2\pi}\sum_{n\in\mathbb{Z}}e^{in(\Omega t-\theta)}\int_{-\pi}^{\pi}e^{in(\theta-\phi)}e^{-ikr\cos(\theta-\phi)}\,\mathrm{d}\phi \ ,$$

(1.36)

after integration one gets:

$$e^{-i\boldsymbol{k}\cdot\boldsymbol{r}_0(t)} = \sum_{n\in\mathbb{Z}} e^{in(\Omega t-\theta)}(-i)^n \mathcal{J}_n(kR) \ , \tag{1.37}$$

where $\mathcal{J}_n$ is the Bessel function of the first kind and of order n, using this result in Eq. (1.34) yields:

$$\partial_t^2\hat{\zeta}(\boldsymbol{k},t) + \omega(k)^2\hat{\zeta}(\boldsymbol{k},t) = \frac{-k\hat{P}_{ext}(k,t)}{\rho}\sum_{n\in\mathbb{Z}} e^{in(\Omega t-\theta)}(-i)^n\mathcal{J}_n(kR). \tag{1.38}$$

$\hat{\zeta}$ is expanded into a Fourier series:

$$\hat{\zeta}(\boldsymbol{k},t) = \sum_{n\in\mathbb{Z}} e^{in\Omega t}c_n(\boldsymbol{k}). \tag{1.39}$$

The linearity of the differential equation permit to treat each harmonic separately, therefore Eq. (1.38) yields:

$$c_n(\boldsymbol{k}) = \frac{ke^{-in\theta}(-i)^n\mathcal{J}_n(kR)\hat{P}_{ext}(k)}{\rho(n^2\Omega^2-\omega(k)^2)}. \tag{1.40}$$

Inverting the Fourier transform of the surface displacement, one gets the solution of the uniform circular wake:

$$\zeta(\boldsymbol{r},t) = \sum_{n\in\mathbb{Z}}(-1)^n e^{in(\phi-\Omega t)}\int_0^{+\infty}\frac{k^2}{2\pi\rho}\frac{\hat{P}_{ext}(k)\mathcal{J}_n(kr)\mathcal{J}_n(k\mathcal{R})}{n^2\Omega^2-\omega(k)^2}\,\mathrm{d}k. \tag{1.41}$$

This equation has permitted to model the wake of a whirling beetle, see [7].

1.3.3 Unsteady wake solution

We now parametrize the ship's motion by a function $\boldsymbol{r}_0(t)$ that is not necessarily linear in time or collinear to a straight line. The pressure field can be written as following:

$$P_{\text{ext}}(\boldsymbol{r},t) = P_{\text{ext}}(\boldsymbol{r}-\boldsymbol{r}_0(t)), \tag{1.42}$$

By the properties of the Fourier transform under variable translation, we deduce:

$$\hat{P}_{\text{ext}}(\boldsymbol{k},t) = \hat{P}_{\text{ext}}(\boldsymbol{k})e^{-i\boldsymbol{k}\cdot\boldsymbol{r}_0(t)}. \tag{1.43}$$

Using the Fourier transform on Eq. (1.21) and Eq. (1.10), we solve the differential equation on the surface displacement, using the following initial conditions:

$$\hat{\zeta}(\boldsymbol{k}, t=0) = 0\ , \tag{1.44}$$
$$\partial_t \hat{\zeta}(\boldsymbol{k}, t=0) = 0\ . \tag{1.45}$$

These conditions will be useful at the end of the differential equation's resolution for identifying the constants involved. One readily notices that we have an explicit basis of the solution space at our disposal:

$$y_1(t) = e^{i\omega(k)t}, \tag{1.46}$$
$$y_2(t) = e^{-i\omega(k)t}. \tag{1.47}$$

What we know of second-order differential equations tells us that we can look for solutions of the form:

$$\hat{\zeta}(\boldsymbol{k}, t) = \lambda(t) y_1(t) + \mu(t) y_2(t), \tag{1.48}$$

λ and μ being two smooth functions which depend on $\boldsymbol{k}$. We can find the exact solution under the prescribed initial conditions by solving the system involving the fundamental matrix of the basis of solutions:

$$\begin{pmatrix} y_1 & y_2 \\ y_1' & y_2' \end{pmatrix} \begin{pmatrix} \lambda' \\ \mu' \end{pmatrix} = \begin{pmatrix} 0 \\ -\frac{k\hat{P}_{\text{ext}}(\boldsymbol{k}) e^{-i\boldsymbol{k}\cdot\boldsymbol{r_0}(t)}}{\rho} \end{pmatrix}, \tag{1.49}$$

Therefore:

$$\begin{pmatrix} \lambda' \\ \mu' \end{pmatrix} = -\frac{1}{2i\omega(k)} \begin{pmatrix} -i\omega(k) e^{-i\omega(k)t} & -e^{-i\omega(k)t} \\ -i\omega(k) e^{i\omega(k)t} & e^{i\omega(k)t} \end{pmatrix} \begin{pmatrix} 0 \\ -\frac{k\hat{P}_{\text{ext}}(\boldsymbol{k}) e^{-i\boldsymbol{k}\cdot\boldsymbol{r_0}(t)}}{\rho} \end{pmatrix}. \tag{1.50}$$

After integration, one gets:

$$\lambda(t) = c(\boldsymbol{k}) - \frac{k}{2i\omega(k)\rho} \int_0^t e^{-i\omega(k)\tau} \hat{P}_{\text{ext}}(\boldsymbol{k}, \tau)\, \mathrm{d}\tau, \tag{1.51}$$
$$\mu(t) = d(\boldsymbol{k}) + \frac{k}{2i\omega(k)\rho} \int_0^t e^{i\omega(k)\tau} \hat{P}_{\text{ext}}(\boldsymbol{k}, \tau)\, \mathrm{d}\tau, \tag{1.52}$$

and accordingly:

$$\begin{aligned} \hat{\zeta}(\boldsymbol{k}, t) = & \left(c(\boldsymbol{k}) - \frac{k}{2i\omega(k)\rho} \int_0^t e^{-i\omega(k)\tau} \hat{P}_{\text{ext}}(\boldsymbol{k}, \tau)\, \mathrm{d}\tau \right) e^{i\omega(k)t}, \\ & + \left(d(\boldsymbol{k}) + \frac{k}{2i\omega(k)\rho} \int_0^t e^{i\omega(k)\tau} \hat{P}_{\text{ext}}(\boldsymbol{k}, \tau)\, \mathrm{d}\tau \right) e^{-i\omega(k)t}. \end{aligned} \tag{1.53}$$

The initial conditions yield:

$$c(\boldsymbol{k}) + d(\boldsymbol{k}) = 0, \tag{1.54}$$
$$i\omega(k)c(\boldsymbol{k}) - i\omega(k)d(\boldsymbol{k}) = 0, \tag{1.55}$$

and therefore $c(\boldsymbol{k}) = d(\boldsymbol{k}) = 0$. Then:

$$\hat{\zeta}(\boldsymbol{k}, t) = -\int_0^t \sin(\omega(k)(t-\tau))\frac{k\hat{P}_{\text{ext}}(\boldsymbol{k}, \tau)}{\rho\omega(k)}\,\mathrm{d}\tau. \tag{1.56}$$

This is the solution of the surface displacement for any given trajectory in Fourier space. If at some time the trajectory $\boldsymbol{r}_0$ start to be linear on time and collinear to a straight line one can show using the dominated convergence theorem that the inverse Fourier transform Eq. (1.56) converges to Eq. (1.30) by taking the limit $t \to \infty$.

1.4 Ship wave pattern

As mentioned earlier, the pattern surprisingly is the same for a duck swimming in a lake or for a cargo in the ocean. Our aim here is to explain and describe this pattern. In 1887, Lord Kelvin presented a first solution for this problem. He realised that the essential feature of the pattern could be extracted from a suitable limit of the intractable integral Eq. (1.30). For that purpose he developed the stationary phase method (see A.1).

1.4.1 Kelvin angle

Before we describe the detailed solution proposed by Kelvin, we can first demonstrate with simple arguments the region occupied by the wave pattern and delimited by a constant angle ϕ_{K}. To do so, we consider a boat moving at a constant velocity V in a straight line. If we observe the wake from the boat, the wake appears to be stationary. Let be

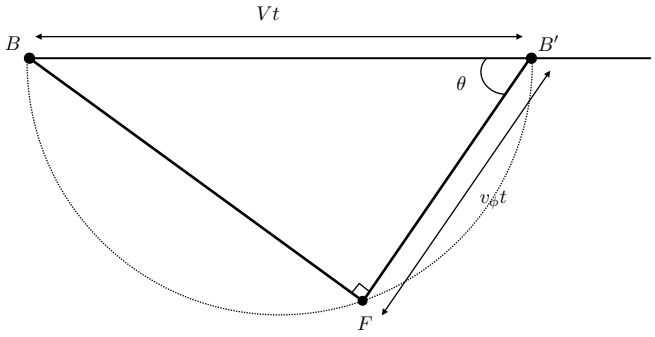

Figure 1.4 Schematic illustrating the construction of the Kelvin angle. The boat is at B, and was at B' at a time t earlier. The wavefront has reached the point F.

the boat at B (see Fig. (1.4)), with the water flowing at speed V from left to right. At a time t earlier, waves were generated at point B'. The distance $BB' = Vt$. The wave front travels at a constant speed v_ϕ away from B' in the direction determine by the angle θ. This wave has a wave number k so that $v_\phi = v_\phi(k)$. In the reference frame of the boat, the stationarity of the waves implies that the shifted pulsation due to a Doppler effect is zero $\omega - \boldsymbol{k} \cdot \boldsymbol{V} = 0$ and thus we have:

$$v_\phi(k) = V \cos(\theta) \ , \tag{1.57}$$

therefore all the wavefront coming from B' lies on the dashed circle of diameterVt. The final ingredient is the property of the dispersion relation. The group velocity, which characterizes the velocity of the enveloppe and the energy is half the phase velocity. Therefore the wavefront of the enveloppe is smaller, the radius of its wavefront is divided by two. We see on Fig. (1.5) that the wedge has a constant angle $\sin(\phi_{\rm K}) = \frac{AO_g}{BO_g}$. It

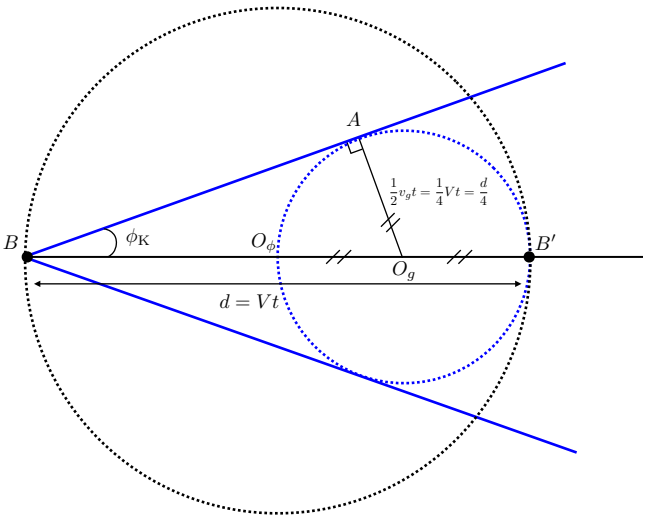

Figure 1.5 Due to the dispersion relation the waves are restricted by a wedge of angle $\phi_{\rm K}$.

is therefore straightforward from the geometrical construction that $\phi_{\rm K} = \arcsin\left(\frac{1}{3}\right) \sim 19.7°$. This simple analysis cannot predict more than the angle of the wake. Kelvin's

calculation used a famous result by Cauchy and Poisson, the surface elevation of the point impulse problem. Knowing the solution of this problem $\eta(\boldsymbol{r}, t)$, Kelvin's idea was to superimpose this elementary solution along the trajectory of the boat. To model the boat by a point implicitly supposes that we are looking at the wake far away from the boat, this assumption being justified by the observation that, indeed, far from the disturbance the wake is identical for a duck or a cargo. Assuming that the boat has been in motion for all previous time, the Kelvin formulation of the problem can be written as:

$$\zeta(\boldsymbol{r}, t) = \int_{-\infty}^{t} \mathrm{d}s \ \eta(\boldsymbol{r}, s) \ . \tag{1.58}$$

1.4.2 Cauchy–Poisson solution

We present here a derivation of the Cauchy-Poisson problem. We wish to determine the surface elevation of a localized impulse in ($\boldsymbol{r} = 0$) at $t = 0$. As in the section 1.2, the velocity potential $\varphi(\boldsymbol{r}, t)$ must be a solution of the Laplace equation:

$$\Delta\varphi \;=\; 0\;, \tag{1.59}$$

and the boundary condition at the free surface:

$$(\partial_t^2\varphi + g\partial_z\varphi)_{z=0} \;=\; 0\;. \tag{1.60}$$

The external pressure field is zero for $t > 0$ and we consider a unitary pressure impulse at $t = 0$. Using the Fourier transform of the velocity potential, we have the result:

$$\hat{\varphi}(\boldsymbol{k}, z, t) \;=\; -\frac{1}{\rho}e^{kz}\cos(\omega(k)t)\;. \tag{1.61}$$

The Fourier transform of the kinematic boundary condition given by Eq. (1.10) is $k\,\varphi(\boldsymbol{k}, z = 0, t) = \partial_t\hat{\eta}(\boldsymbol{k}, t)$. The Fourier transform of the surface is therefore:

$$\hat{\eta}(\boldsymbol{k}, t) \;=\; -\frac{k}{\rho\omega(k)}\sin(\omega(k)t) \tag{1.62}$$

One can notice the radial symmetry of the solution of Cauchy-Poisson. By inverting the Fourier transform we obtain after computing the radial integral the result for the velocity potential and the surface elevation:

$$\varphi(r, z, t) \;=\; -\frac{1}{2\pi\rho}\int_0^\infty \mathrm{d}k\; e^{kz}\,\mathcal{J}_0(kr)\cos(\omega(k)t)k\;, \tag{1.63}$$

$$\eta(r, t) \;=\; -\frac{1}{2\pi\rho}\int_0^\infty \mathrm{d}k\; \mathcal{J}_0(kr)\frac{\sin(\omega(k)t)k^2}{\omega(k)}\;. \tag{1.64}$$

An approximation of this integral can be obtained from Kelvin's method (see Appendix A.1). Since $\mathcal{J}_0(x)$ is a fluctuating function which tends as z increases to have the same period as $\sin(z)$, therefore the integrals above will for the most part cancel except for stationary phase:

$$t\frac{\mathrm{d}\omega}{\mathrm{d}k} \;=\; r\;, \quad \text{or} \tag{1.65}$$

$$kr \;=\; \frac{gt^2}{4r}\;. \tag{1.66}$$

When kr is large we use the asymptotic development of the Bessel function (it can be as well demonstrated by the stationary phase method):

$$\mathcal{J}_0(kr) \sim \sqrt{\frac{2}{\pi kr}} \sin\left(kr + \frac{\pi}{4}\right) \ . \tag{1.67}$$

At the surface, the velocity potential can therefore be written as:

$$\varphi(r,t)|_{z=0} \ \sim \ -\frac{\sqrt{g}}{(2\pi)^{3/2}\sqrt{r}} \int_0^\infty \mathrm{d}k \ \cos\left(\omega t - kr - \frac{\pi}{4}\right) \ . \tag{1.68}$$

Using the stationary phase method explained in Appendix (A) we find:

$$\varphi(r,t)|_{z=0} \ \sim \ -\frac{\sqrt{g}}{2\pi\sqrt{rt|\frac{\mathrm{d}^2\omega}{\mathrm{d}k^2}|}} \ \sin\left(\omega t - kr\right) \ . \tag{1.69}$$

Eventually when $\frac{gt^2}{2r}$ is sufficiently large, we have the surface elevation asymptotic form that reads:

$$\eta(r,t) \ \sim \ -\frac{gt^3}{2^{7/2}r^4} \sin\left(\frac{gt^2}{4r}\right) \ . \tag{1.70}$$

This solution was first found by Cauchy-Poisson using other analytical techniques [6, 3, 5].

1.4.3 Kelvin's theory

In the preceding section, we obtained an approximation of the surface displacement for a point impulse at the water surface, using the stationary phase method repeatedly. These approximations are valid at all points far from the boat. In this section we carry out the solution of the ship wave problem using Kelvin's proof. Kelvin did this proof for a boat moving on a straight line at constant speed, in fact using his method more complex trajectories can be determined, especially for a circular course. More details can be found in the very detailed book of Stoker on water waves [5].
The boat is now modeled by a point impulse along a path $C = (X_t, Y_t)$ over the surface for $t \in [0, T]$ in order to avoid the divergence of the integral in Eq. (1.58). On Fig. (1.6) the parameter t represents the time required for the boat to go from any point $B(X_t, Y_t)$ to the origin. But for simplicity, we assume that the boat is at the origin at time $t = 0$ and therefore the point B moves backwards along the boat trajectory as t increases. The vector $\boldsymbol{t}$ is tangent to the path C at the point B and is opposite the direction of the boat:

$$\boldsymbol{t} \ = \ \left(\dot{X}_t, \dot{Y}_t\right) \ , \tag{1.71}$$

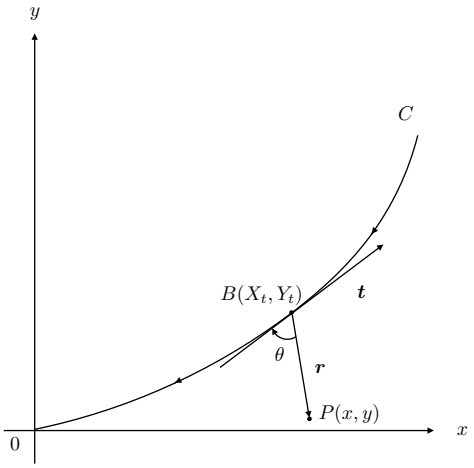

Figure 1.6 Path of the boat on the water surface.

The speed of the boat is therefore simply given by:

$$V(t) = \sqrt{\dot{X}_t^2 + \dot{Y}_t^2} \, . \tag{1.72}$$

The point $P(x, y)$ is the point where we compute the surface elevation. This point can be defined from the boat by the vector:

$$\boldsymbol{r} = (x - X_t, y - Y_t) \, . \tag{1.73}$$

We also define on the figure the angle θ between $\boldsymbol{r}$ and $\boldsymbol{t}$. The effect of an impulse is determined by the solution of Cauchy-Poisson stated in Eq. (1.70). Therefore the integration of all the point impulse effects over time, gives the ship wave pattern:

$$\zeta(\boldsymbol{r}, t) = \zeta_0 \int_0^t \mathrm{d}s \, \frac{s^3}{r^4} \sin\left(\frac{gs^2}{4r}\right) \, , \tag{1.74}$$

with $zeta_0$ a constant. In order to apply the stationary phase method, we write Eq.(1.74) in the form:

$$\zeta(\boldsymbol{r}, t) = \mathrm{Im}\left[\int_0^t \mathrm{d}s \; f(s) e^{ig(s)}\right] \, , \tag{1.75}$$

where the two functions are defined as follows:

$$f(t) = \frac{\zeta_0 t^3}{r^4} \, , \tag{1.76}$$

$$g(t) = \frac{gt^2}{4r} \, . \tag{1.77}$$

The stationary points are given by $g'(t) = 0$. This derivatives leads to an important relation that holds for any kind of trajectory:

$$\frac{\mathrm{d}r}{\mathrm{d}t} = \frac{2r}{t} . \tag{1.78}$$

The time derivative of the distance $r = |\boldsymbol{r}|$ is computed using Eq. (1.73). One easily finds:

$$r\frac{\mathrm{d}r}{\mathrm{d}t} = -\boldsymbol{r}\cdot\boldsymbol{t} . \tag{1.79}$$

Thus

$$\frac{\mathrm{d}r}{\mathrm{d}t} = V\cos(\theta) , \tag{1.80}$$

combining Eq. (1.78) coming from the stationary phase computation and Eq. (1.80), that is the time derivative of the distance from the boat, we obtain the stationary phase condition in the following form:

$$r = \frac{1}{2}Vt\cos(\theta) . \tag{1.81}$$

This relation gives the points that are influenced by a given point on the boat's trajectory. The points P that are influenced by the emission of water wave at the point B (see Fig. 1.6) lies on a circle of diameter $\frac{Vt}{2}$ with the diameter of the circle following the tangent at the trajectory in B as shown on the figure: To calculate the curves of constant phase it is

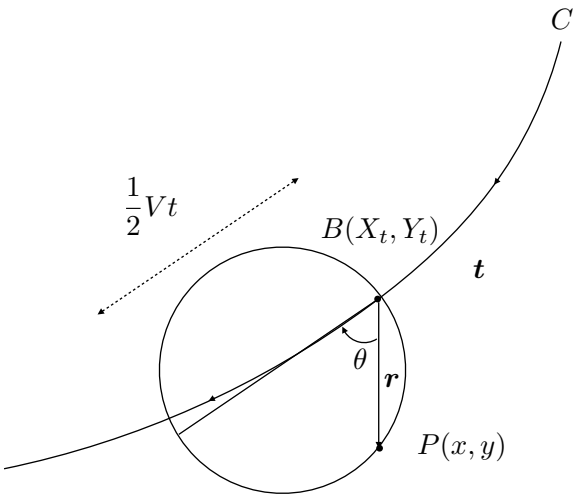

Figure 1.7 Wave front emitted by the boat in B.

convenient to express the stationary phase condition using the following parameter:

$$\lambda = \frac{V^2t^2}{2r} , \tag{1.82}$$

where λ has the dimension of a length. Using this parameter the stationary phase conditions are thus:

$$Vt = \lambda \cos(\theta) \ , \tag{1.83}$$

$$r = \frac{1}{2}\lambda \cos^2(\theta) \ . \tag{1.84}$$

It is important to note that this relation holds for all kind of trajectories of the boat as long as we can use the stationary phase approximation.

Straight motion

If the boat has uniform straight motion, its trajectory is simply $C = (Vt, 0)$, therefore the point P on the Fig. (1.7) is simply $P = (Vt - r\cos(\theta), -r\sin(\theta))$. Using the reformulation of the stationary phase conditions Eq. (1.84) we obtain directly a parametric equation for the wave crests and troughs:

$$x = \lambda \left(\cos(\theta) - \frac{1}{2}\cos^3(\theta) \right) \quad , \quad y = -\frac{1}{2}\lambda \cos^2(\theta)\sin(\theta) \ . \tag{1.85}$$

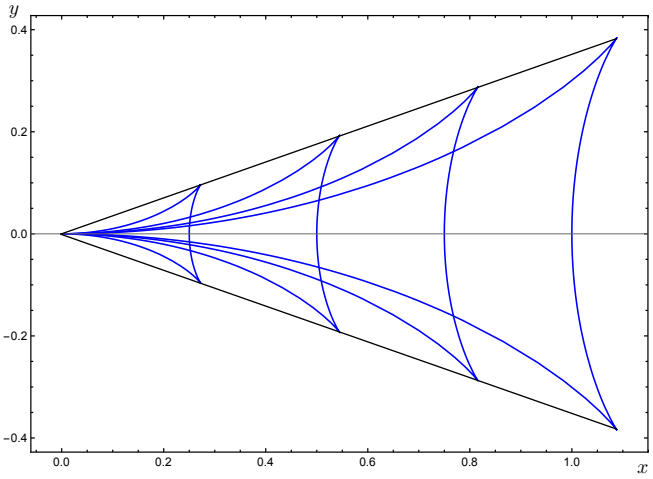

Figure 1.8 Plot of the ship wave pattern for the following set of parameters $\lambda = \{0.5, 1, 1.5, 2\}$. Each curve represents a pattern of constant phase in the water waves.

We observe on Fig. (1.8) both diverging and transverse waves. The cusps can be easily computed from the parametric equations given above in Eq. (1.85).

Circular motion

We can carry out the calculation of the curve of constant phase for circular motion. The path of the boat in this case is simply $C = (R\sin(\beta), R(1-\cos(\beta)))$ with the angle $\beta = \frac{Vt}{R}$.

R is the radius of the boat's circle trajectory. Thus the coordinates of point P are given by:

$$x = X_t - r\cos(\beta+\theta) \quad , \quad y = Y_t - r\sin(\beta+\theta)\ . \tag{1.86}$$

Eventually using the dimensionless parameter $\gamma = \lambda/R$, one finds that the angle is given by:

$$\beta = \gamma\cos(\theta)\ . \tag{1.87}$$

Yielding the parametric equation for the constant phase:

$$x/R = \sin(\beta\cos(\theta)) - \frac{\beta}{2}\cos^2(\theta)\cos(\theta+\beta\cos(\theta))\ , \tag{1.88}$$

$$y/R = 1-\cos(\beta\cos(\theta)) - \frac{\beta}{2}\cos^2(\theta)\sin(\theta+\beta\cos(\theta))\ . \tag{1.89}$$

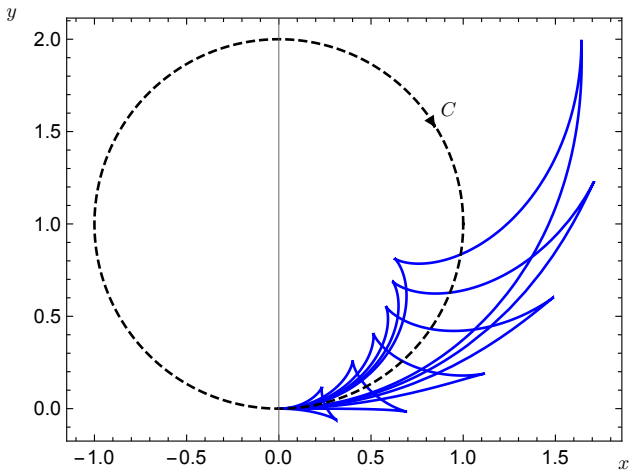

Figure 1.9 Plot of the ship wave pattern for the following set of parameter $\beta = \{0.5, 1, 1.5, 2, 2.5, 3\}$. Each curve represents a pattern of constant phase in the water waves, for a trajectory C of the boat on a unitary circle.

1.5 Wave resistance

The most common manifestation of wave resistance is for submarines ; close to the surface, the maximal velocity of a submarine is around 20 knots whereas deep under water, it can reach 30 knots. This dramatic effect is only explained by wave resistance. We also have in mind the American swimmer who won the 50 meters free-still by staying under water and thus generated less wave resistance. Another famous manifestation of wave resistance has been reported in the nineteenth century by a navigator in an expedition at

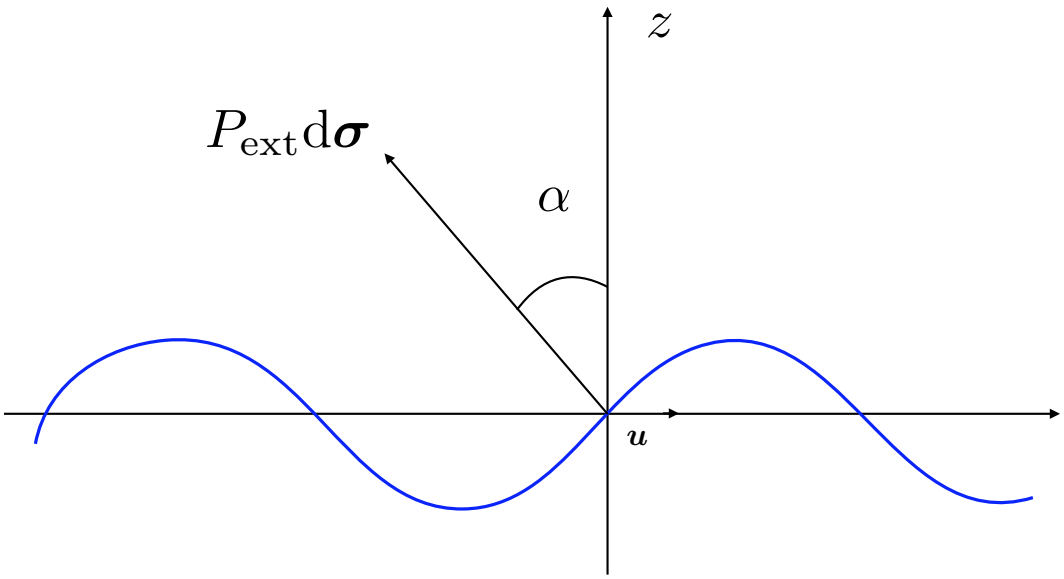

Figure 1.10 Havelock method to compute wave resistance.

the North Pole. When they approached the ice field, the boat experienced a considerable slowdown. This effect was known as the dead water effect, it was in fact an important wave resistance due to the creation of surface waves at the interface of fresh water and salty water, this layer of fresh water coming from the melting of the ice.

1.5.1 Havelock formula

When a boat travels at the free surface of water, it generates waves carrying energy to infinity. This loss of energy by radiation opposes a resistance to the boat's motion. The wave resistance R_w is the force associated to the loss of energy due to radiation of water waves. According to Havelock [1], we may imagine a rigid cover fitting the surface everywhere. The pressure $P_{\text{ext}}(x)$ is applied to the liquid surface by means of this cover; hence the wave resistance is simply the total resolved pressure in the x direction. Using the notation introduced in Fig.1.10, one has

$$P_{\text{ext}}\mathrm{d}\boldsymbol{\sigma}\cdot\boldsymbol{u} = -P_{\text{ext}}\sin(\alpha). \tag{1.90}$$

In the approximation of small amplitudes and slopes, one gets the Havelock's formula:

$$\boldsymbol{R_w} = -\iint P_{\text{ext}}(\boldsymbol{u}\cdot\boldsymbol{\nabla})\zeta\ \mathrm{d}\sigma\ \boldsymbol{u}\ , \tag{1.91}$$

$\boldsymbol{u}$ being a unitary vector collinear to the velocity.

The second definition is given by the radiated energy, when a disturbance moves at

a constant velocity, it generates waves at the surface that are radiated to infinity. The power dissipated can be assimilated to the power of a force acting against the disturbance's motion. The power dissipated is given by [8]:

$$P_w = \iint P_{\text{ext}} \nabla_n \phi \, \mathrm{d}\sigma \ , \tag{1.92}$$

where ∇_n denotes the derivative along the vector normal to the surface. In a steady regime, the kinetic boundary condition reads:

$$\nabla_n \phi = \boldsymbol{v} \cdot \boldsymbol{\nabla} \zeta. \tag{1.93}$$

Therefore, if we assume that this power is the power of a force acting against the disturbance's motion, we are left with

$$\boldsymbol{R}_w \ \cdot \boldsymbol{v} = -P_w, \tag{1.94}$$

which leads as well to Havelock's formula:

$$\boldsymbol{R_w} = -\iint P_{\text{ext}} (\boldsymbol{u} \cdot \boldsymbol{\nabla}) \zeta \ \mathrm{d}\sigma \ \boldsymbol{u} \ . \tag{1.95}$$

The solution of the surface displacement is much simpler in Fourier space, therefore it is useful to express the wave resistance as an integral in the Fourier space:

$$\boldsymbol{R_w} = -\frac{i}{4\pi^2} \iint \mathrm{d}^2\boldsymbol{k} \ (\boldsymbol{u} \cdot \boldsymbol{k}) \hat{\zeta}(\boldsymbol{k}, t) \hat{P}^*_{\text{ext}}(k, t) \boldsymbol{u} \ . \tag{1.96}$$

1.5.2 General regime

For an arbitrarily moving object, the water surface is in general time-dependent. Therefore, the moving disturbance will experience a force with a non-zero vertical component. Using Havelock's approach, one can compute the power of the force acting on the moving disturbance. First, we compute the power of the horizontal force. This is exactly the power computed in the previous section; following the exact same reasoning, Eq.1.91 gives:

$$P_w = -\iint P_{\text{ext}} (\boldsymbol{v} \cdot \boldsymbol{\nabla}) \zeta \mathrm{d}\sigma \ . \tag{1.97}$$

One may next compute the power of the vertical force. For an unsteady regime, the surface deformation is time-dependent in the presence of the pressure field. We compute the vertical work of the pressure field on the surface. Between t and $t + \mathrm{d}t$, the surface moves vertically of $\partial_t \zeta(\boldsymbol{r}, t)\mathrm{d}t$ under the action of the pressure field. Therefore, the vertical work of the pressure field acting on the surface is:

$$\delta W_v = -\iint P_{\text{ext}} \ \partial_t \zeta(\boldsymbol{r}, t) \ \mathrm{d}t \ \mathrm{d}\sigma, \tag{1.98}$$

and the power reads:

$$P_v = -\iint P_{\text{ext}}(x,y)\ \partial_t\zeta(\boldsymbol{r},t))\ \mathrm{d}\sigma. \tag{1.99}$$

This power is zero in the ship's frame of reference if we consider a steady regime in this frame (i.e. $\partial_t\zeta(x,y,t)=0$). Now that we have the power of the vertical and horizontal force acting on the moving disturbance, we check that its corresponds to the opposite of the power dissipated in the water waves. The kinematic condition at the free surface is :

$$\frac{\mathrm{d}\zeta}{\mathrm{d}t} = \partial_t\zeta + (\boldsymbol{v}\cdot\boldsymbol{\nabla})\zeta = \partial_z\phi. \tag{1.100}$$

Therefore, it is straightforward to obtain:

$$P(t) = -(P_w + P_v)\ , \tag{1.101}$$

with $P(t)$, the power given by the boat to the fluid, defined in [8] (Eq.1.92). To conclude, one may notice that with an arbitrarily moving disturbance, the power radiated in the water waves results in two acting forces on the object: a vertical and a horizontal force. The horizontal one is called wave resistance. One can notice that at a standstill, the moving disturbance does not experience wave resistance, but only vertical oscillations ([9]. Therefore Eq. (1.95), Havelock's formula is the effective wave resistance while the speed is non-zero.

1.5.3 Wave resistance of an uniform straight motion

If we consider a disturbance moving at a constant velocity $\boldsymbol{V} = V\boldsymbol{e}_x$, therefore using Eq. (1.29) we find the general formula for the wave resistance of a boat moving at a constant velocity:

$$R_{\text{w}} \quad = \quad \iint \frac{\mathrm{d}k_x\,\mathrm{d}k_y}{4\pi^2\rho}\,\frac{1}{k}\,\frac{ik_x\left|\hat{P}_{\text{ext}}(k_x,k_y)\right|^2}{v_\phi^2(k)-V^2(k_x/k)^2}\ . \tag{1.102}$$

In order to plot the wave resistance, we use the dimensionless gaussian pressure field:

$$\hat{P}_{\text{ext}}(k) = \frac{f_0}{\rho g L^3}e^{-\frac{k^2}{4\pi^2}} \tag{1.103}$$

we note $Fr = \frac{V}{\sqrt{gL}}$ the Froude number of our system and we use $r = R_w 2\pi^3/f_0^2$ the dimensionless wave resistance.

$$r = \iint \mathrm{d}k\mathrm{d}\theta \frac{ik^2\cos(\theta)e^{-\frac{k^2}{2\pi^2}}}{1-Fr^2k\cos(\theta)^2} \tag{1.104}$$

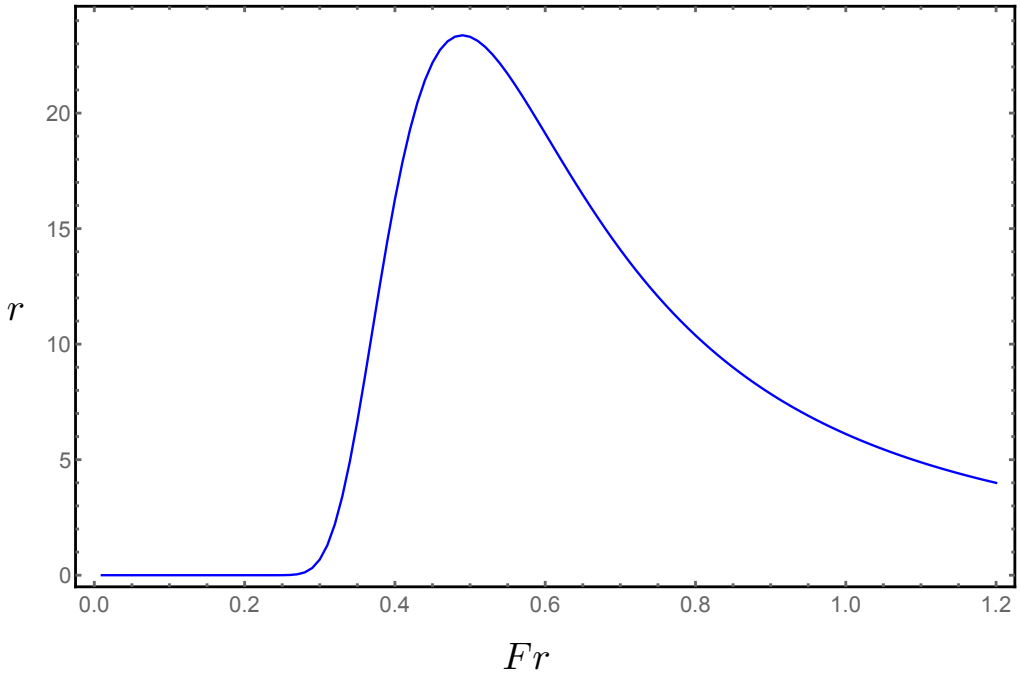

Figure 1.11 Dimensionless wave resistance as a function of the Froude number for gravity waves.

after integration one gets:

$$r = \frac{1}{Fr^6}\int_0^{\pi/2} \frac{\mathrm{d}\theta}{\cos(\theta)^5} e^{-\frac{1+\tan(\theta)^2}{2\pi^2 Fr^4 \cos(\theta)^2}} \tag{1.105}$$

1.5.4 Wave resistance of an uniform circular motion

Now if we consider a disturbance moving at constant speed $V = R\Omega$ along a circle centered on 0 and of radius R, using Eq. (1.41) we have:

$$R_w = \sum_{n>0} \frac{n}{R} \frac{\left(k_n \mathcal{J}_n(k_n R)\hat{P}(k_n)\right)^2}{\left(\frac{\mathrm{d}\omega^2}{\mathrm{d}k}\right)_{k_n}} , \tag{1.106}$$

where k_n is the unique solution of the equation $\omega(k_n) = n\Omega$.

1.5.5 Free deceleration

Within the framework of this generalized Havelock formula, we can now theoretically solve the problem of the free deceleration of a moving body at the water surface. One can consider for example the deceleration of a nitrogen droplet over water ([10]). Following the Havelock formula, the experienced wave resistance is given by:

$$\boldsymbol{R}_w = -\frac{i}{4\pi^2}\iint \mathrm{d}^2\boldsymbol{k}\ \hat{\zeta}(\boldsymbol{k},t)\hat{P}^*_{\mathrm{ext}}(\boldsymbol{k},t)\boldsymbol{k}. \tag{1.107}$$

Therefore for a decelerated motion at the free surface using Eq. (1.56) for an axisymmetric pressure field one gets:

$$\boldsymbol{R}_w = -\int_0^t \mathrm{d}\tau \int_0^\infty \frac{\mathrm{d}k}{2\pi}\frac{k^3|\hat{P}_{\mathrm{ext}}(k)|^2}{\rho\omega(k)}\sin(\omega(k)(t-\tau))\mathcal{J}_1(k(r_0(t)-r_0(\tau)))\boldsymbol{u}_x. \tag{1.108}$$

Using Newton's law on the nitrogen droplet, the trajectory of the droplet verifies:

$$m_d\frac{\mathrm{d}^2 r_0}{\mathrm{d}t^2} = -R_w(\{r_0(t)\}). \tag{1.109}$$

By solving this integro-differential equation, one could get the exact trajectory of an object decelerating at a fluid interface by radiating waves.

1.6 Conclusion

In this introductive chapter we have presented elementary properties of water waves in deep water. We have derived and discussed the fundamental properties of the dispersion relation and derived from the dynamical equation the integral expression of the surface displacement resulting from a boat at constant speed. Following the historical demonstration, we have presented the elementary solution of a point impulse known as the Cauchy-Poisson problem, and used it to derive the wake pattern as Kelvin first did historically. Eventually we presented the main results of this chapter, we established that the Havelock formula for the wave resistance is still valid for any kind of motion or trajectories at the surface, the usual demonstration in the literature assume a steady straight motion.

Chapter 2

Elasto-hydrodynamic wake and wave resistance

Chapter 2 : Elasto-hydrodynamic wake and wave resistance

↑ back to contents

Chapter abstract

We study theoretically the effects of an external pressure disturbance moving at a constant speed along a thin lubricated elastic sheet. In the comoving frame, the imposed pressure field creates a stationary deformation of the free interface that spatially disappears in the far-field region. The shape of the wake and the way in which it decays depend on the speed and size of the external pressure field, as well as the rheological properties of the elastic and liquid layers. The wave resistance and the viscous dissipation are analyzed in detail.

2.1 Introduction

When a thin viscous film is coupled to an elastic layer, several interesting phenomena occur, and particularly at an interface where we observe a different behavior than that observed in the bulk material, and in particular the generation of surface waves. We shall highlight here that the seminal studies on elastohydrodynamic wakes were motivated by the waves generated by the Antarctic landing planes [11, 12], in this observations the

observed regime is dominated by the fluid inertia.

Many hydrodynamic results can be revisited introducing an elasto-hydrodynamic interaction. For example the capillary rise [13], or the viscous Saffman-Taylor fingering [14, 15, 16], for which the presence of an elastic sheet can prevent instability. In the domain of the physics of painting, the propagation of the peel front in a plastic sheet placed on top of a layer of glycerin or the flexible scraping of viscous fluids were studied [17]. Also a lift force acting on an object moving and interacting via hydrodynamic forces [18, 19, 20, 21, 22] was predicted and confirmed experimentally [23]. Reminiscent patterns of dewetting can be observed when a wet elastic sheet is in contact with a solid substrate [24, 25].

In this chapter we combine wake physics and elastohydrodynamics [26, 27], this new class of problems has applications in geophysics, biophysics, wave propagation and particularly for the measurement at nano-scale: the deformation of the substrates [28] modify the observation and the accuracy of these experiments. After recalling lubrication theory, we establish the equation of the elastohydrodynamic thin film, then we study the displacement of an external pressure field over a thin elastic sheet covering a thin viscous film. In the approximation of lubrication, we calculate the elastohydrodynamic waves and the wake, as well as the wave resistance. An equivalent of the Bond number where elasticity replaces capillarity seems to be a dimensionless central parameter of the problem and we call it the elastic Bond number in the following. The elastohydrodynamic wake is plotted for a wide range of speeds and elastic Bond numbers. We provide asymptotic analytical results for wave resistance for both low and high speed. Eventually, we show that the energy transferred by the perturbation of the fluid is entirely dissipated by the viscosity.

2.2 Elastohydrodynamic thin film equation

In numerous flows like painting, lubrication of pieces or between bones for exemple, the streamlines are parallel. An important result of such flows is that the friction force between two bodies can be reduced dramatically. Leonardo da Vinci noticed 400 years ago that "*All things and anything whatsoever, however thin it be, which is interposed in the middle between objects that rub together lighten the difficulty of this friction.*" Under some hypotheses on the velocity fields, we can neglect non-linear terms: this is the approximation of lubrication. We establish the elastohydrodynamic thin film equation with a thin elastic sheet atop the fluid: a thin viscous film of thickness h_0 placed over a flat horizontal substrate, and covered by a thin elastic sheet of constant thickness $d \ll h_0$.

2.2.1 Thin film problem

Before deriving the elastohydrodynamic thin film equation, we specify the model and its assumptions in the lubrication approximation. Our stating point is a liquid film of height

$z = h(\boldsymbol{r}, t)$ deposited on a flat surface and covered by a thin elastic sheet of constant thickness d.

2.2.2 Lubrication approximation

The film has a typical height h_0 much smaller than the horizontal extent of the film l_0 therefore one can introduce a dimensionless parameter:

$$\epsilon = h_0/l_0 \ . \tag{2.1}$$

Then we define the space and time dimensionless variables through $h = h_0\tilde{h}$ and:

$$\begin{aligned} x &= l_0\,\tilde{x} && (2.2a)\\ y &= l_0\,\tilde{y} && (2.2b)\\ z &= l_0\,\tilde{z} && (2.2c)\\ t &= t_0\,\tilde{t}\ , && (2.2d) \end{aligned}$$

where t_0 is a typical time scale yet to be determined. A 3D incompressible fluid verifies:

$$\boldsymbol{\nabla}\cdot\boldsymbol{v} \;=\; \partial_x v_x + \partial_y v_y + \partial_z v_z \;=\; 0\ , \tag{2.3}$$

which, together with Eqs. (2.1) and (2.2a), notably implies that the dimensionless velocities are introduced as:

$$\begin{aligned} v_x &= v_0\,\tilde{v}_x && (2.4a)\\ v_y &= v_0\,\tilde{v}_y && (2.4b)\\ v_z &= \epsilon\, v_0\,\tilde{v}_z\ , && (2.4c) \end{aligned}$$

where $v_0 = l_0/t_0$ is a typical velocity scale yet to be determined. If we consider the Navier-Stokes equation:

$$\partial_t\boldsymbol{v} + \boldsymbol{v}\cdot\boldsymbol{\nabla}\boldsymbol{v} = -\frac{1}{\rho}\boldsymbol{\nabla}p + \eta\Delta\boldsymbol{v} \quad , \tag{2.5}$$

where η is the cinematic viscosity. At the leading order in ϵ one gets the two following equations:

$$\begin{aligned} \boldsymbol{\nabla}p &= \mu\,\partial_z^2\boldsymbol{v} && (2.6a)\\ \partial_z p &= 0\ , && (2.6b) \end{aligned}$$

where μ is the dynamic viscosity, $\boldsymbol{\nabla}$ is now the gradient in the plane xy and $\boldsymbol{v}(\boldsymbol{r}, z, t)$ the horizontal velocity field. We assume no slip at both the substrate-liquid and the

liquid-elastic interfaces, so that the boundary conditions read:

$$\boldsymbol{v}|_{z=0} = \mathbf{0} \tag{2.7a}$$
$$\boldsymbol{v}|_{z=h} = \mathbf{0} \, . \tag{2.7b}$$

Integrating Eq. (2.6a) together with Eqs. (2.6b) and (2.7) leads to a Poiseuille flow of the form:

$$\boldsymbol{v}(\boldsymbol{r}, z, t) = \frac{1}{2\mu} (z^2 - hz) \boldsymbol{\nabla} p \, . \tag{2.8}$$

Furthermore, conservation of volume can be expressed as:

$$\partial_t h = -\boldsymbol{\nabla} \cdot \boldsymbol{Q} \, , \tag{2.9}$$

where $\boldsymbol{Q} = \int_0^h \mathrm{d}z \, \boldsymbol{v}$ is the horizontal flux. Combining Eqs. (2.8) and (2.9) finally leads to the general thin-film equation:

$$\partial_t h - \frac{1}{12\mu} \boldsymbol{\nabla} \cdot \left(h^3 \boldsymbol{\nabla} p \right) = 0 \, . \tag{2.10}$$

2.2.3 Linear elastohydrodynamic thin film equation

The pressure field is given by the addition of the bending stress and the hydrostatic pressure and thus reads:

$$P_{\mathrm{tot}} = B \nabla^4 h + \rho g h \, , \tag{2.11}$$

with $B = Ed^3/[12(1-\nu^2)]$ the bending stiffness, E and ν are respectively the Young's modulus and Poisson's ratio [29], g is the acceleration of gravity, and ρ is the density of the liquid. In this model we neglect the stretching of the thin elastic sheet. By replacing Eq. (2.11) in Eq. (2.10) one obtains the elastohydrodynamic thin film equation:

$$\partial_t h - \frac{B}{12\mu} \boldsymbol{\nabla} \cdot \left(h^3 \boldsymbol{\nabla}^5 h \right) - \frac{\rho g}{12\mu} \boldsymbol{\nabla} \cdot \left(h^3 \boldsymbol{\nabla} h \right) = 0 \, . \tag{2.12}$$

The characteristic length are h_0 for the vertical z-direction and the gravito-elastic length $\kappa_{\mathrm{el}}^{-1} = (B/\rho g)^{1/4}$ for the xy plane. The natural time scale of this problem reads:

$$\tau = \frac{12\mu}{(\rho g \kappa_{\mathrm{el}}^2 h_0^3)} \, , \tag{2.13}$$

therefore we construct the characteristic velocity scale $v_{\mathrm{el}} = \kappa_{\mathrm{el}}^{-1} \tau^{-1}$. We introduce dimensionless variables in order to re-express Eq. (2.14): $\tilde{x} = \kappa_{\mathrm{el}} x$, $\tilde{y} = \kappa_{\mathrm{el}} y$, $\tilde{h} = h/h_0$, $\tilde{t} = t/\tau$. Considering small deformations $\zeta = \tilde{h} - 1 \ll 1$, Eqs. (2.14) and (2.11) are linearized and we obtain the dimensionless elastohydrodynamic thin-film equation [30] on the surface

displacement $\zeta(\tilde{x}, \tilde{y}, \tilde{t})$:

$$\partial_{\tilde{t}}\zeta = \tilde{\Delta}^3\zeta + \tilde{\Delta}\zeta, \tag{2.14}$$

where $\tilde{\Delta}$ denotes the dimensionless Laplacian operator in 2D Cartesian coordinates. In the rest of this chapter, we will omit the symbol $\tilde{}$ for dimensionless quantities.

2.3 Elastohydrodynamic wake

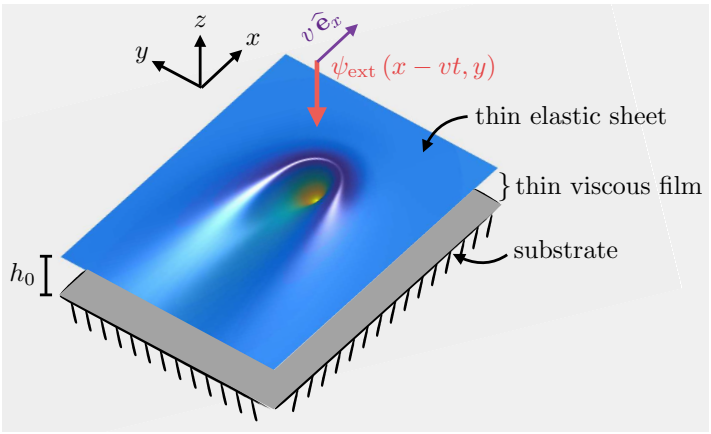

Figure 2.1 Plot of the elastohydrodynamic wake. The elastic film reacts to an external pressure field $\psi_{\text{ext}}(x - vt, y)$ moving at constant speed $v \geq 0$ along the x direction.

A thin viscous film of thickness h_0 is over a flat solid substrate, and covered by a thin elastic sheet of constant thickness $d \ll h_0$. As depicted in Fig. 2.1, an external pressure field $\psi_{\text{ext}}(x - vt, y)$ moves along the horizontal axis x at constant velocity. As a result, we observe the displacement $h\,(x, y, t)$ of the liquid-elastic interface. We are interested here to stationary surface profiles in the comoving frame, the disturbance is static in this reference frame, and we define the surface displacement in this frame $f(x, y, t) = \zeta\,(u, y)$ where $u = x - v\,t$. The dimensionless external pressure $\Psi = \psi$, with $P_{\text{ext}} = \kappa_{\text{el}}^2 \iint dx\,dy\,\psi_{\text{ext}}$ as the characteristic pressure scale and the dimensionless number $\Gamma_{\text{el}} = P_{\text{ext}}/\,(\rho g h_0)$ appear naturally. Therefore the total hydrostatic pressure field in presence of the external load reads:

$$P_{\text{tot}} = B\nabla^4 h + \rho g h + \psi_{\text{ext}}\ . \tag{2.15}$$

In this context, eq. (2.14) becomes:

$$\Delta^3\zeta + \Delta\zeta + v\frac{\partial}{\partial u}\zeta = -\Gamma_{\text{el}}\Delta\Psi\ , \tag{2.16}$$

where Δ is the dimensionless Laplacian operator in 2D Cartesian coordinates and in the

comoving frame. Finally, let us introduce the two relevant dimensionless parameters of the problem: the elastic Bond number $B_{\mathrm{el}} = (a\,\kappa_{\mathrm{el}})^2$, and a denotes the characteristic horizontal size of the external pressure field. By definition, the wake is the solution $\zeta\,(u,y)$ of eq. (2.16), for a given disturbance field $\Gamma_{\mathrm{el}}\Psi$ and reduced speed v. Invoking the two-dimensional Fourier transforms, defined as:

$$\hat{f}(k_x,k_y) = \iint_{-\infty}^{+\infty} f(u,y)e^{-i(k_x u+k_y y)}\mathrm{d}y\mathrm{d}u\ , \tag{2.17}$$

$$f(u,y) = \frac{1}{4\pi^2}\iint_{-\infty}^{+\infty} \hat{f}(k_x,k_y)e^{i(k_x u+k_y y)}\mathrm{d}k_x\mathrm{d}k_y\ , \tag{2.18}$$

and applying them to the dimensionless profile and the external pressure field, $\widehat{\zeta}\,(k_x,k_y)$ and $\widehat{\Psi}\,(k_x,k_y)$, eq. (2.16) becomes:

$$\left[ik_x v-(k_x^2+k_y^2)^3-(k_x^2+k_y^2)\right]\widehat{\zeta}\,(k_x,k_y)=\Gamma_{\mathrm{el}}(k_x^2+k_y^2)\,\widehat{\Psi}\,(k_x,k_y)\ . \tag{2.19}$$

Consequently, the solution reads:

$$\zeta\,(u,y)=\frac{\Gamma_{\mathrm{el}}}{4\pi^2}\iint\frac{(k_x^2+k_y^2)e^{i(k_x u+k_y y)}\widehat{\Psi}\,(k_x,k_y)}{ik_x v-(k_x^2+k_y^2)\left[1+(k_x^2+k_y^2)^2\right]}dk_x dk_y\ . \tag{2.20}$$

In order to plot the wake produced by the displacement of the pressure field, we choose two pressure fields, first a Dirac pressure field:

$$\Psi\,(u,y)=\delta(u,v)\ , \tag{2.21a}$$

$$\widehat{\Psi}\,(k_x,k_y)=1\ , \tag{2.21b}$$

and an axisymmetric Lorentzian pressure field:

$$\Psi\,(u,y)=\frac{\sqrt{B_{\mathrm{el}}}}{2\pi\left(u^2+y^2+B_{\mathrm{el}}\right)^{3/2}}\ , \tag{2.22a}$$

$$\widehat{\Psi}\,(k_x,k_y)=\exp\left[-\sqrt{B_{\mathrm{el}}\left(k_x^2+k_y^2\right)}\right]\ . \tag{2.22b}$$

The combination of Eqs. (2.20), (2.22) and (2.21) leads to the surface pattern. A parametric study has been performed, scanning a wide range of values for the reduced speed v and elastic Bond number B_{el}, as summarized in Fig. 2.2. This is analogous to the visco-capillary study presented in this article about wake and wave resistance on a viscous film. We recover the setup studied in this article [31] by removing the elastic sheet atop the fluid. In this condition the total pressure field is the combination of the external pressure

field, the hydrostatic pressure due to gravity and the capillary pressure:

$$P_{\text{tot}} = -\gamma \nabla^2 h + \rho g h + \psi_{\text{ext}} \ . \tag{2.23}$$

therefore the wake without elastic sheet reads:

$$\zeta\left(u,y\right) = \frac{\Gamma_{\text{el}}}{4\pi^2} \iint \frac{(k_x^2+k_y^2) e^{i(k_x u + k_y y)} \widehat{\Psi}\left(k_x,k_y\right)}{i k_x v - (k_x^2+k_y^2)\left[1+k_x^2+k_y^2\right]} dk_x dk_y \ . \tag{2.24}$$

The three main differences between the two cases are the order of the partial differential equation (2.16), and the two dimensionless parameters: the reduced speed v normalized by the elastic speed $v_{\text{el}} = \kappa_{\text{el}}^{-1}\,\tau^{-1}$ and the elastic Bond number $B_{\text{el}} = \left(a\,\kappa_{\text{el}}\right)^2$, here replacing the capillary speed $c = \kappa^{-1}\,\tau^{-1}$ and the Bond number $B_{\text{o}} = (a\kappa)^2 = \rho g a^2/\gamma$, respectively, of the study on viscous wake and wave resistance [31].

Fig 2.2 shows the wake created by the disturbance for several regimes. We observe at low velocity an almost symmetric deformation corresponding to the static deformation of the surface by the pressure field. When the velocity reaches the elastic speed v_{el}, we observe a bump ahead of the pressure field and a stretched cavity behind. Eventually, at high velocity, the wake is surrounded by oscillations. The elastic Bond number plays a role on the surrounding oscillations, the smaller the disturbance (i.e. smaller elastic Bond numbers or higher rigidity), the more oscillations we observe.

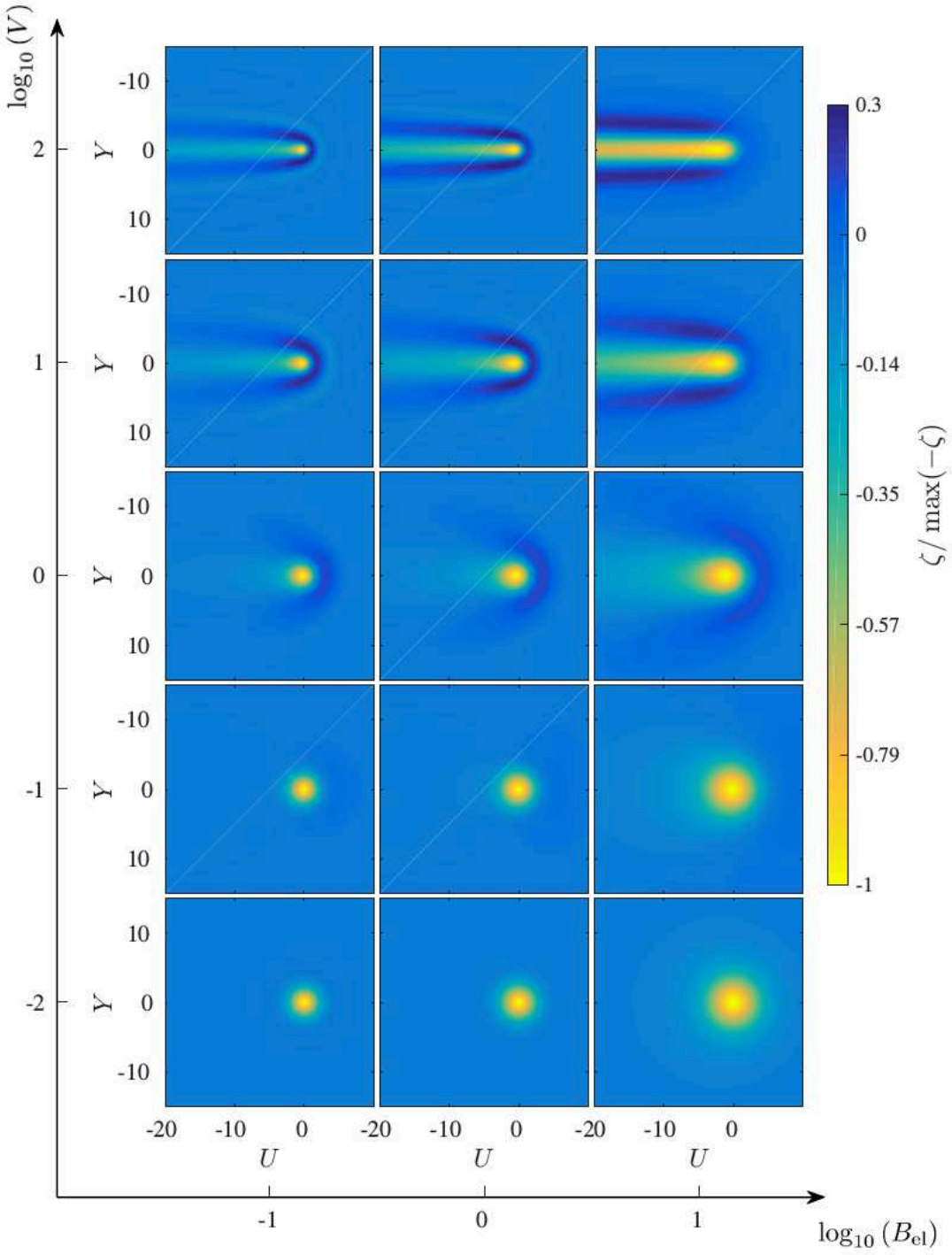

Figure 2.2 Normalized wake view from atop created by a Lorentzian pressure field. Computed from Eqs. (2.20) and (2.22), for different values of the elastic Bond number B_{el} and the reduced speed v. In the comoving-frame, variables, the pressure field is centered at $u = 0$. In this reference frame, the film travels from right to left at constant speed v.

2.4 Wave resistance

As the pressure disturbance moves atop the elastic sheet, it generates the previously-discussed surface deformation which is intimately coupled to the motion of the underlying liquid. As discussed previously, the moving disturbance creates a displacement of the elastic sheet coupled to the fluid underneath. To maintain a constant speed, the operator needs to provide the energy lost by deforming the surface, as there is a force opposing to the motion of the moving disturbance as defined in section 1.5. The wave resistance is set to be r and is given by Havelock's formula, usually used in the inviscid theory of waves [32, 33], but still valid for a viscous fluid [8]:

$$r = \iint \psi_{\text{ext}} \frac{\partial h}{\partial x} dx\, dy \ . \tag{2.25}$$

The power vr must be furnished by the operator in order to maintain a constant disturbance speed v [31]. With the notations introduced above, the dimensionless wave resistance R reads:

$$R = \frac{r\kappa_{\text{el}}}{\rho g h_0^2} = \Gamma_{\text{el}} \iint \Psi(u,y)\partial_u \zeta \, \mathrm{d}u \, \mathrm{d}y \ . \tag{2.26}$$

Then, the substitution of Eq. (2.20) within Eq. (2.26) yields:

$$R = \frac{\Gamma_{\text{el}}^2 v}{4\pi^2} \iint \frac{k_x^2(k_x^2+k_y^2)\left|\widehat{\Psi}\left(k_x,k_y\right)\right|^2}{k_x^2 v^2 + (k_x^2+k_y^2)^2\left(1+(k_x^2+k_y^2)^2\right)^2} \, \mathrm{d}k_x \, \mathrm{d}k_y \ . \tag{2.27}$$

Using polar coordinates $k_x = k\cos\theta$ and $k_y = k\sin\theta$, and assuming an axisymmetric pressure field $\widehat{\Psi}(\rho)$, after integration over θ we retrieve the following expression:

$$R = \frac{\Gamma_{\text{el}}^2}{2\pi v} \int_0^\infty \left[1 - \frac{k(k^4+1)}{\sqrt{v^2+k^2(k^4+1)^2}}\right] \left|\widehat{\Psi}(k)\right|^2 k^3 \mathrm{d}k \ . \tag{2.28}$$

We numerically compute the wave resistance using Eqs. (2.22) and (2.28). The results are presented in Fig. 2.3.

As expected, the wider the pressure field (small elastic Bond number), the lower the wave resistance. Therefore the wave resistance has an upper bound given by the Dirac pressure field, indeed a Dirac pressure field excites all the wave length whereas a larger one will cut the large wavelength [33].

For the Lorentzian pressure field we observe at low speed a linear increase of the wave resistance with v. Then the wave resistance reaches a maximal value and eventually at high speed it decreases in v^{-1}. The Dirac case shows the same behavior at low velocity, but after reaching its maximal value, the wave resistance decreases with a more gentle slope of $v^{-1/5}$.

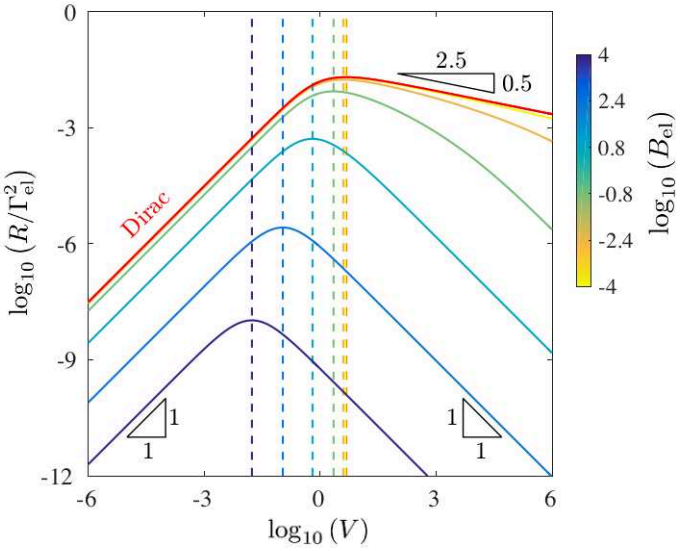

Figure 2.3 Normalized wave resistance R/Γ_{el}^2, as given by eqs. (2.22) and (2.28), as a function of the reduced speed V, for various elastic Bond numbers B_{el}. The Dirac limit ($B_{el} \to 0$) is indicated. The vertical dashed lines indicate the position of maximal wave resistance (see eq. (2.37)) for each value of B_{el}.

2.4.1 Asymptotic regime

In order to have the asymptotic regime at low speed, we do a series development of Eq. (2.28) around $v = 0$, one gets:

$$R = \frac{\Gamma_{el}^2 v}{4\pi} \int_0^\infty \frac{k|\Psi(k)|^2}{(k^4+1)^2} \mathrm{d}k + o(v) \tag{2.29}$$

Using the Dirac pressure field, we get the following asymptotic expression from Eq. (2.29) as $v \to 0$:

$$R \sim \frac{\Gamma_{el}^2 v}{32} \ . \tag{2.30}$$

Using the Lorentzian pressure field of Eq. (2.22), the wave resistance reads:

$$R \sim \frac{\Gamma_{el}^2 v}{4\pi} \mathcal{F}(B_{el}) \ , \tag{2.31}$$

where:

$$\mathcal{F}(B_{el}) = \int_0^{+\infty} \frac{k \exp\left(-2\sqrt{B_{el}}k\right)}{\left(k^4+1\right)^2} \mathrm{d}k \ . \tag{2.32}$$

Therefore we recover the linear dependence in v at low speed for both Lorentzian and Dirac pressure field.
In the limit of a large pressure field with respect to the gravito-elastic length, $B_{el} \gg 1$,

one obtains:

$$\mathcal{F}(B_{\text{el}}) \sim \frac{1}{4B_{\text{el}}} \ . \tag{2.33}$$

In the high-speed regime of Fig. 2.3, one has two distinct scaling behaviors with v. Indeed, for the Dirac case, using the asymptotic development of eq. (2.28) as $v \to \infty$, one gets:

$$R \sim -\frac{\Gamma_{\text{el}}^2 \Gamma(-2/5)\Gamma(9/10)}{20\pi^{3/2}} \frac{1}{v^{1/5}} \ , \tag{2.34}$$

where $\Gamma(z)$ is the Gamma function:

$$\Gamma(z) = \int_0^{+\infty} t^{z-1} e^{-t} \mathrm{d}t \ . \tag{2.35}$$

For the Lorentzian pressure field of eq. (2.22), one obtains:

$$R \sim \frac{3\Gamma_{\text{el}}^2}{16\pi B_{\text{el}}^2} \frac{1}{v} \ . \tag{2.36}$$

Eqs. (2.34) and (2.36) show that the wave resistance for a finite-size pressure field (which is more realistic) decays much faster than for the Dirac pressure field.

2.4.2 Maximal wave resistance

All the wave resistance curves in Fig. 2.3 show a maximum. We set $v^*(B_{\text{el}})$ the speed at which this maximum is reached. By balancing the two asymptotic regimes we obtain a scaling for this maximal velocity and the corresponding wave resistance. First we consider the Lorentzian pressure field, that yields:

$$v^* \sim \sqrt{\frac{3}{4\mathcal{F}(B_{\text{el}})B_{\text{el}}^2}} \ . \tag{2.37}$$

Therefore at high elastic Bond numbers, corresponding to a wide pressure field, one finds:

$$v^* \sim \sqrt{\frac{3}{B_{\text{el}}}} \ , \tag{2.38}$$

thus the amplitude of the wave resistance at this particular point is:

$$R(v^*) \sim \frac{\sqrt{3}\Gamma_{\text{el}}^2}{16\pi B_{\text{el}}^{3/2}} \ . \tag{2.39}$$

The maximal wave resistance for $B_{\mathrm{el}} \to 0$, corresponding to a Dirac pressure field, is obtained by balancing the low-speed and high-speed asymptotic expressions of the wave resistance of the Dirac pressure field:

$$v^* \sim \left(-\frac{8\Gamma(-2/5)\Gamma(9/10)}{5\pi^{3/2}} \right)^{5/6} , \tag{2.40}$$

the corresponding wave resistance is:

$$R(v^*) \sim \frac{\Gamma_{\mathrm{el}}^2}{32} \left(-\frac{8\Gamma(-2/5)\Gamma(9/10)}{5\pi^{3/2}} \right)^{5/6} . \tag{2.41}$$

The asymptotic behaviors for low and high elastic Bond number, given by Eqs. (2.38) and (2.40) for v^*, and Eqs. (2.39) and (2.41) for $R(v^*)$, are represented in Figure. 2.4. These results are summarized in Fig. 2.4. We predict that the maximal wave resistance decreases as $B_{\mathrm{el}}^{-3/2}$ for wide pressure field, and saturates to a finite value in the Dirac limit. The corresponding speed v^* decreases as $B_{\mathrm{el}}^{-1/2}$ at large B_{el}, and saturates as well in the Dirac limit. This maximum could be important in the designing of nano-rehological experiments.

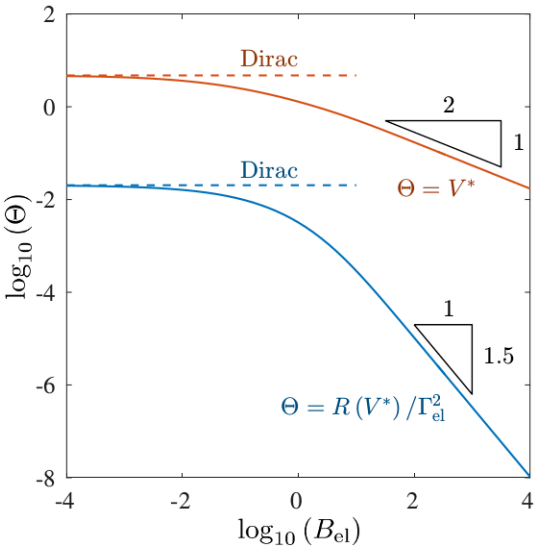

Figure 2.4 Normalized maximal wave resistance $R(v^*)/\Gamma_{\mathrm{el}}^2$ (blue) and its corresponding speed v^* (red), as functions of the elastic Bond number B_{el} see Eqs. (2.32) and (2.37). The dashed lines represent the Dirac limits given by Eqs. (2.40) and (2.41).

2.4.3 Viscous dissipation

The product vr is the required power to displace the surface profile at constant speed, we can show that it also corresponds to the power dissipated within the viscous thin film.

The power dissipated in the fluid reads:

$$P_v = \iiint \mathrm{d}^3\tau \ \mu \boldsymbol{v} \cdot \Delta \boldsymbol{v} \tag{2.42}$$

Using Eq. (2.8), the power is thus:

$$P_v = \iiint \mathrm{d}^3\tau \ \boldsymbol{v} \cdot \boldsymbol{\nabla} p \ , \tag{2.43}$$

then we integrate over z the velocity field:

$$P_v = \iint \mathrm{d}^2\sigma \ \boldsymbol{Q} \cdot \boldsymbol{\nabla} p \ , \tag{2.44}$$

$$= - \iint \mathrm{d}^2\sigma \ p \boldsymbol{\nabla} \cdot \boldsymbol{Q} \ . \tag{2.45}$$

We now use the volume conservation defined by Eq. (2.9),

$$P_v = \iint \mathrm{d}^2\sigma \ p \partial_t h \ , \tag{2.46}$$

in presence of an external pressure field we thus have:

$$P_v = \iint \mathrm{d}^2\sigma \ \left(B\nabla^4 h + \rho g h + \Psi_{\mathrm{ext}} \right) \partial_t h \ , \tag{2.47}$$

$$= v \iint \mathrm{d}^2\sigma \ \Psi_{\mathrm{ext}} \partial_x h \tag{2.48}$$

$$= rv \tag{2.49}$$

indeed one can check through integration by parts that:

$$\iint \mathrm{d}^2\sigma \ \nabla^4 h \ \partial_x h = 0 \ , \tag{2.50}$$

$$\iint \mathrm{d}^2\sigma \ h \ \partial_x h = 0 \ . \tag{2.51}$$

Therefore the power dissipated by viscosity is equal to the power of the wave resistance. We can conclude that the energy transferred to the fluid by the external pressure field is completely dissipated by viscosity.

2.5 Conclusion

We presented a theoretical investigation of the effects of a moving pressure disturbance above a thin elastic sheet placed atop a narrow viscous film. From the elastohydrodynamic lubrication model, we computed both the wake and the associated wave resistance experienced by the operator. A central dimensionless parameter of this study appeared to be the elastic Bond number. Then we have performed the asymptotic analysis of the

low-speed and high-speed regimes and find a scaling for the maximum of the wave resistance, a reference point that could be important for designing nano-rheological setup. Eventually we shown that the energy transfer to the fluid by deforming the interface is fully dissipated by viscous damping.

Chapter 3

Walking on water

Chapter 3 : Walking on water

↑ back to contents

Chapter abstract

In this chapter, we study both theoretically and experimentally the wave pattern generated by the leg strokes of the water strider. First we will see that the propulsion cycle is divided into three phases. Then we focus on the first phase, the leg stroke, with a theoretical model and we compare our prediction to experimental measurements. Through the use of the synthetic Schlieren method we are able to accurately measure the dynamic response of the free surface.

3.1 Introduction

Several insect and arachnid species exploit water's static and dynamic deformations [34] to live at the air-water interface. Water striders are among the best known insects existing at the air-water interface. They are the most studied insects regarding locomotion in such a habitat [35, 36, 37], and notably due to their ability to jump in the air using the water

surface as a trampoline [38, 39]. They have also been increasingly used as a template for microbots [40, 41, 42, 43].
We know that the displacement of a disturbance at the surface creates a complex wave pattern [44]. The waves and vortices created by the water striders are the signature of the momentum applied to the water. Theoretical studies on waves and vortices has made great advances for water striders [45, 46, 35, 47, 48]. However it is still unclear as to

Figure 3.1 Cover page of Nature representing the Bush experiments [45] on water strider propulsion (2003).

whether surface waves are more important than vortices in transferring the momentum imparted by the leg to the water. The experimental side principally relies on the works of [45, 49] and [50] who made PIV (particle imaging velocimetry) measurements of the water surface. They also filmed the animal from the side, thereby obtaining a rough estimate of the dip of the meniscus. However, none of them recorded the surface wave signature in detail nor made PIV records from the side. As for vortices, the computations of [47] predict that the vortices are detaching from the water surface under given conditions, in conflict with the experiments of [50] showing that vortices do not detach. Unfortunately, these experiments were carried out in very shallow water (with 1.2 mm depth and a 0.3 mm ink layer at the bottom) making difficult the reconciliation of the experiments with the infinite depth assumption of the available theoretical work.
The present chapter quantifies with unmatched precision (5 μm resolution) the water surface deformations during the water-strider leg strike in order to understand the importance of accounting for the details of the fluid-structure interaction, as opposed to the impulsive forcing model by Bühler, where the strike is localised in time and space. We furthermore extend Bühler's theory to shallow water and to a continuous non-impulsive forcing. Our work has implications beyond the locomotion at the air-water interface, as small amplitude wave-trains are used by many insects living at the water surface [51, 52, 53].

3.2 Denny's paradox

The mechanism by which the water strider stands on the water surface is classically explained as a result of surface tension. When a water strider puts one of its legs on the water surface, it creates a dimple. The vertical component of the resulting capillary force resists to the mass of the insect, and the water strider is supported. The capillary force that supports the water strider is proportional the the surface of the legs and scales roughly linearly with the size of the animal, whereas the mass will scale as the volume of the animal. As a consequence, standing on water is limited to small organisms. When the insect moves across the water surface, the legs transfer momentum to the water. M. Denny thought that the momentum associated with the waves created by the gerris could be the transferred momentum. However we know from Fig. (1.3) and Eq. (1.23) that for capillary-gravity waves, their is a minimum wave speed $c_{\min} = 23$ cm.s^{-1} for a water-air interface. For Denny, this minimum of speed of surface waves sets a minimum speed at which the leg must move in order to make waves. From this statement Denny thought they were a paradox since such insects have leg speeds below $c_{\min}$.
Obviously this paradox does not hold for several reasons. The first one is that we can transfer energy with legs moving below $c_{\min}$, the previous statement only holds for a stationary regime, and a leg stroke is not a stationary regime. However this paradox has triggered a lot of interest in the study of water strider locomotion. Particularly in a study by Bush [45], a series of experiments reveals that the strider transfers momentum to the water via water waves but also through hemispherical vortices shed by its driving legs. In the study, they show that the momentum carried by the vortices is around 10^{-5} kg.m.s^{-1}, the same order of magnitude than the gerris' momentum. So even if some small insects are not able to produce water waves, they still could produce vortices to transfer energy to the fluid.

3.3 Gerris trajectories

Using a camera, we can record the trajectory and speed of a water strider. It appears from the experiments that the locomotion phase can be divided into three phases. First we have the propulsion phase lasting around 15 ms, which will be detailed extensively later. Secondly, we observe a plateau of constant speed during approximately 15 ms, during which the water strider almost doesn't touch the interface, and this time corresponds to a free fall of 1 mm high, and eventually when all the legs of the gerris reach the water surface again, they are decelerated at a rate of around 7m.s^{-2}. This corresponds to a typical wave resistance deceleration. Indeed, following [33], we can show that the wave resistance of a very small (compared to the capillary length) pressure field scales like:

$$R^* = \frac{Mg}{\kappa^{-1}\gamma} g \tag{3.1}$$

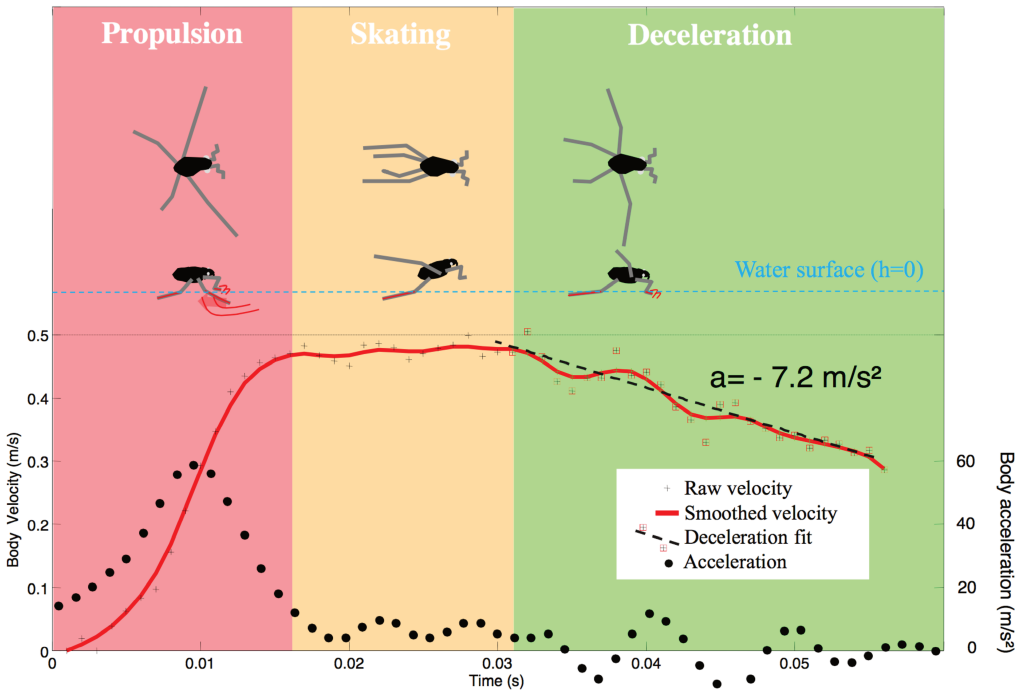

Figure 3.2 Body velocity of a water strider during its propultion phase above the water.

this is the typical amplitude of the wave resistance for a Dirac pressure field [33]. For a water-air interface, and the typical size and weight of a gerris [54] we find $R^* \sim 7.14\text{m.s}^{-2}$, the deceleration phase seems to be completely due to wave resistance. If one wanted to determine the exact time dependence for the speed or position of the gerris during this phase, they would have to solve Eq. (1.109) giving the exact trajectory of a free decelerating body via water wave radiation.

3.4 Surface response to an impulsive pressure field

In this section, we recall and extend to finite depth Bühler's calculation for the fluid interface response to an impulsive leg stroke (given by a delta function in time) of the water strider. In particular we provide an analytical expression for the surface displacement and generalize Bühler's results to finite depth in order to match typical experimental conditions. In addition, we extend Bühler's impulsive approach to a rapid leg stroke (finite time τ_{imp}). In the following, we denote $\boldsymbol{r} = (x, y, z)$ and $\boldsymbol{x} = (x, y)$.

3.4.1 Infinite depth

Consider an incompressible, inviscid, infinitely deep liquid whose free surface at rest is located at $z = 0$. As mentioned earlier, the original model by Bühler is based on the assumption that the stroke can be considered impulsive and localized. Furthermore, we assume that the impulsive force is horizontal, aligned with the x axis. The impulsive force field applied to the fluid is taken to be of the form:

$$\boldsymbol{F}(\boldsymbol{r}, t) \quad = \quad \boldsymbol{f}(\boldsymbol{r})\delta(t) \ , \tag{3.2}$$

where the spatial part $\boldsymbol{f}$ reads:

$$\boldsymbol{f}(\boldsymbol{r}) = f_0\delta(x)\delta(y)\delta(z+h)\boldsymbol{e}_x \ , \tag{3.3}$$

and where h typically corresponds to the depth of the meniscus created by the water strider at rest. Note however that in the present model the free surface is taken to be flat at $t = 0$, by that neglecting the static deformation of the interface. The resulting pressure field p can be computed from the Poisson equation:

$$\Delta p \quad = \quad \boldsymbol{\nabla} \cdot \boldsymbol{f} \ , \tag{3.4}$$

subject to the boundary conditions $p(x, y, z = 0) = 0$ and $\boldsymbol{\nabla} p|_{r\to\infty} \to \boldsymbol{0}$, where $r = |\boldsymbol{r}|$. Equation (3.4) results from taking the divergence of the linearized Euler equation together with the incompressibility condition. We know that the Green function of the Poisson equation in an unbounded 3D domain is:

$$G_0(\boldsymbol{r}, \boldsymbol{r}') = -\frac{1}{4\pi||\boldsymbol{r} - \boldsymbol{r}'||} \tag{3.5}$$

The Green's function $\tilde{G}(\boldsymbol{r}, \boldsymbol{r}')$ of the problem is solution of Eq. (3.4) with right hand-side equal to $\delta(\boldsymbol{r} - \boldsymbol{r}')$. It can be computed using the method of images to ensure a vanishing solution at the interface, thus it is equal to the unbounded Green function given by Eq. (3.5) minus the equal and opposite image source at the mirror location with respect to the interface to ensure a vanishing solution at the interface (see [46]). Therefore it yields:

$$\tilde{G}(\boldsymbol{r}, \boldsymbol{r}') = G_0(\boldsymbol{r}, x', y', z') - G_0(\boldsymbol{r}, x', y', -z') \tag{3.6}$$

Convolving the obtained Green's function with the right hand side of Eq. (3.4), one obtains the impulsive pressure field p:

$$p = \int \tilde{G}(\boldsymbol{r}, \boldsymbol{r}')\boldsymbol{R} \cdot \boldsymbol{\nabla}'\delta(x')\delta(y')\delta(z'+h)\mathrm{d}x\mathrm{d}y\mathrm{d}z = \boldsymbol{R} \cdot \boldsymbol{\nabla}'\tilde{G}(\boldsymbol{r}, 0, 0, -h) \ , \tag{3.7}$$

therefore the horizontal pressure field, in which we are interested, corresponds at first order in h:

$$p(\boldsymbol{r}) \;=\; -h\frac{3f_0}{2\pi}\frac{xz}{r^5} + O(h^2)\;. \tag{3.8}$$

The knowledge of p allows one to compute the resulting free surface displacement. In the following, we establish the free surface displacement in response to a given surface pressure field. The velocity potential $\phi(\boldsymbol{r},t)$ is determined by solving the Laplace equation $\Delta\phi = 0$ together with the boundary conditions:

$$\boldsymbol{\nabla}\left[\partial_t^2\phi + g\partial_z\phi - \gamma\partial_z\Delta_{x,y}\phi + \frac{1}{\rho}\partial_t P\right]_{z=0} \;=\; \mathbf{0} \tag{3.9a}$$

$$\partial_z\phi\big|_{z\to-\infty} \;=\; 0\;, \tag{3.9b}$$

where g denotes the acceleration of gravity, γ the surface tension, and $P(\boldsymbol{r},t)$ the imposed pressure field. The general solution reads ([44]):

$$\phi(\boldsymbol{r},t) \;=\; \int \frac{\mathrm{d}^2\boldsymbol{k}}{(2\pi)^2}\, A(\boldsymbol{k},t)\, e^{i(ux+vy)}e^{kz}\;, \tag{3.10}$$

where $\boldsymbol{k} = (u,v)$. Projecting Eq. (3.9a) along the vertical axis $\boldsymbol{e}_z$ and injecting Eq. (3.10) leads to:

$$k\left[\partial_t^2 A + \omega(k)^2 A\right] \;=\; -\frac{1}{\rho}\partial_t\mathcal{F}\left[\partial_z P\big|_{z=0}\right]\;, \tag{3.11}$$

where $\omega^2 = \gamma k^3/\rho + gk$ denotes the dispersion relation for capillary-gravity waves, and where $\mathcal{F}$ denotes the spatial two-dimensional Fourier transform operator. The kinematic boundary condition $\partial_t\zeta = \partial_z\phi|_{z=0}$ can be written in Fourier space as:

$$\partial_t\hat{\zeta} \;=\; kA\;, \tag{3.12}$$

where $\hat{\zeta}(\boldsymbol{k},t) = \mathcal{F}[\zeta]$. Injecting Eq. (3.12) into Eq. (3.11) and integrating over time yields:

$$\partial_t^2\hat{\zeta} + \omega(k)^2\hat{\zeta} \;=\; -\frac{1}{\rho}\mathcal{F}\left[\partial_z P\big|_{z=0}\right]\;. \tag{3.13}$$

Equation (3.13) is key in the sense that it allows us to compute the surface displacement $\zeta(\boldsymbol{x},t) = \mathcal{F}^{-1}[\hat{\zeta}]$ for any given pressure distribution $P(\boldsymbol{r},t)$ and for any given set of initial conditions. The general solution can be written as the sum of the solution to the homogenous equation and a particular solution to the nonhomogeneous equation, namely

$\hat{\zeta}(\boldsymbol{k},t) = \hat{\zeta}_{\rm h}(\boldsymbol{k},t) + \hat{\zeta}_{\rm p}(\boldsymbol{k},t)$ where:

$$\hat{\zeta}_{\rm h}(\boldsymbol{k},t) = \hat{\zeta}(\boldsymbol{k},0)\cos(\omega(k)t) + \partial_t\hat{\zeta}(\boldsymbol{k},0)\frac{\sin(\omega(k)t)}{\omega(k)} \tag{3.14a}$$

$$\hat{\zeta}_{\rm p}(\boldsymbol{k},t) = -\frac{1}{\rho}\int_0^t {\rm d}\tau\,\frac{\sin(\omega(k)(t-\tau))}{\omega(k)}\,\mathcal{F}\left[\partial_z P\big|_{z=0}\right]\,, \tag{3.14b}$$

and where the particular solution was determined from the method of variation of constants, explained in section 1.3.3. The homogeneous solution is precisely the well-known *Cauchy-Poisson* solution [55] also called free-wave solution exposed in section 1.4.2. We here assume that the free surface is initially considered at rest, which is $\hat{\zeta}(\boldsymbol{k},0) = 0$ and $\partial_t\hat{\zeta}(\boldsymbol{k},0) = 0$ such that $\hat{\zeta}(\boldsymbol{k},t) = \hat{\zeta}_{\rm p}(\boldsymbol{k},t)$. The impulsive pressure distribution is of form $P(\boldsymbol{r},t) = p(\boldsymbol{r})\delta(t)$ where $p(\boldsymbol{r})$ is given by Eq. (3.8). Injecting $P(\boldsymbol{r},t)$ into Eq. (3.14b) yields:

$$\hat{\zeta}(\boldsymbol{k},t) = -\frac{1}{\rho}\frac{\sin(\omega(k)t)}{\omega(k)}\,\mathcal{F}\left[\partial_z p\big|_{z=0}\right]\,, \tag{3.15}$$

where at first order in h:

$$\mathcal{F}\left[\partial_z p\big|_{z=0}\right] = -\mathcal{F}\left[\frac{3f_0}{2\pi}\frac{hx}{\left(x^2+y^2+h^2\right)^{5/2}}\right]\,. \tag{3.16}$$

Recalling the results of [46], we here compute the response of the free surface to the impulsive pressure field in infinite depth. Taking the pressure field given by Eq. (3.16) and computing the Fourier transform with polar coordinates (r,θ), we use $\boldsymbol{k}\cdot\boldsymbol{r} = kr\cos(\theta-\phi)$, with θ the polar coordinates in the real space and ϕ the polar coordinates in the Fourier space, one obtains after some calculations:

$$\begin{aligned}
\mathcal{F}\left[\frac{\partial p_{\rm imp}}{\partial z}\big|_{z=0}\right] &= -\frac{3f_0h}{2\pi}\iint {\rm d}x{\rm d}y\;\frac{x}{\left(x^2+y^2+h^2\right)^{5/2}}e^{-i(k_xx+k_yy)} \\
&= -\frac{3f_0h}{2\pi}\iint {\rm d}r{\rm d}\theta\;\frac{r^2\cos(\theta)}{\left(r^2+h^2\right)^{5/2}}e^{-ikr\cos(\theta-\phi)} \\
&= -\frac{3f_0h}{2\pi}\int_0^\infty {\rm d}r\;\frac{r^2}{\left(r^2+h^2\right)^{5/2}}\int_{-\pi}^{\pi}\cos(\theta)e^{-ikr\cos(\theta-\phi)}\,.
\end{aligned} \tag{3.17}$$

After integrating over theta one easily gets:

$$\int_{-\pi}^{\pi}\frac{{\rm d}\theta}{2\pi}\cos(\theta)e^{-ikr\cos(\theta-\phi)} = -i\cos(\phi)J_1(kr)\,. \tag{3.18}$$

Thus

$$\begin{aligned}\mathcal{F}\left[\frac{\partial p_{\text{imp}}}{\partial z}\Big|_{z=0}\right] &= 3if_0h\frac{k_x}{k}\int_0^{+\infty}\mathrm{d}r\,\frac{r^2}{(r^2+h^2)^{\frac{5}{2}}}J_1(kr)\\ &= if_0k_x\exp(-hk)\ .\end{aligned} \tag{3.19}$$

From this distribution, we compute the evolution of the free surface after an oriented impulsion:

$$\zeta_{\text{imp}}(\boldsymbol{x},t) = -i\frac{f_0}{(2\pi)^2\rho}\int_0^{+\infty}\mathrm{d}k_x\mathrm{d}k_yk_x\exp(-hk)\frac{\sin(\omega(k)t)}{\omega(k)}\exp(i(k_xx+k_yy))\ . \tag{3.20}$$

After a polar transformation in Fourier space we obtain an expression for the evolution of the free surface after an impulsive strike:

$$\zeta_{\text{imp}}(\boldsymbol{x},t) = \frac{f_0}{2\pi\rho}\frac{x}{\sqrt{x^2+y^2}}\int_0^{\infty}\mathrm{d}k\,k^2e^{-hk}J_1\left(k\sqrt{x^2+y^2}\right)\frac{\sin(\omega(k)t)}{\omega(k)}\ . \tag{3.21}$$

Eq. (3.21) gives the evolution of the free surface after an impulsion.

3.4.2 Finite depth

The measurements were performed in shallow water due to optical resolution. Therefore, we extend the theory to the case of shallow water. With the same assumptions than in the previous section, we consider an impulsive force field localized at $x = y = 0$ and depth $z = -h$ where $h > 0$ in a shallow water of depth $H > h$. The force field is given by Eqs. (3.2) and (3.3), and the resulting pressure field is found by solving the Poisson equation (see Eq. (3.4)) but with a different set of boundary conditions: $p(z = 0) = 0$, $\partial_z p(z = H) = 0$ and $\boldsymbol{\nabla} p|_{r\to\infty} \to \mathbf{0}$. In the finite depth case, one must first compute the pressure field resulting from an impulsive force in finite depth and the resulting surface response. Let G be the Green's function of the problem given by Eq (3.4) subject to $p(z = 0) = 0$, $\partial_z p(z = -H) = 0$ and $\nabla p \to 0$ as $\sqrt{x^2+y^2} \to \infty$. The function G solves: $\Delta G = \delta(\boldsymbol{x} - \boldsymbol{x}')$, with the same boundary conditions, which leads to: $p = -f_0\partial_x G(\boldsymbol{x}, 0, 0, -h)$. Using the eigen-decomposition of the Laplacian with these boundaries:

$$\Psi_n(k_x,k_y) = \frac{\sqrt{2/H}}{2\pi}e^{i\boldsymbol{k}\cdot\boldsymbol{r}}\sin\left(\Lambda_nz\right)\ , \tag{3.22}$$

where $\Lambda_n = (2n+1)\pi/(2H)$, together with the spectral formula of Green's function (see Appendice A.2.1), one obtains:

$$\begin{aligned}G(\boldsymbol{r},\boldsymbol{r'}) &= \frac{1}{2\pi^2H}\sum_{n=0}^{\infty}\sin\left(\Lambda_nz\right)\sin\left(\Lambda_nz'\right)\iint dk_xdk_y\frac{e^{i\boldsymbol{k}\cdot(\boldsymbol{r}-\boldsymbol{r'})}}{k^2+\Lambda_n^2}\\ &= \frac{1}{\pi H}\sum_{n=0}^{\infty}\sin\left(\Lambda_nz\right)\sin\left(\Lambda_nz'\right)K_0\left(|r-r'|\Lambda_n\right)\ .\end{aligned} \tag{3.23}$$

The horizontal impulsive pressure field thus reads:

$$p_h = -\frac{f_0}{\pi H}\cos(\theta)\sum_{n=0}^{\infty}\Lambda_n \sin\left(\Lambda_n z\right)\sin\left(\Lambda_n h\right) K_1\left(r\Lambda_n\right) \ . \tag{3.24}$$

Then, in order to compute the deformation of the free surface, we need to compute the Fourier transform of $\partial_z p_h(z=0)$. Computing the derivative with respect to z yields:

$$\frac{\mathrm{d}p_h}{\mathrm{d}z}|_{z=0} = -\frac{f_0}{2\pi H}\cos(\theta)\sum_{n=0}^{\infty}\Lambda_n^2 \sin\left(\Lambda_n h\right) K_1\left(r\Lambda_n\right) \ , \tag{3.25}$$

with $r=\sqrt{x^2+y^2}$. We set $\tilde{f}(k_x,k_y)$ the Fourier transform of $\dfrac{\mathrm{d}p_h}{\mathrm{d}z}(z=0)$:

$$\begin{aligned}
\tilde{f}(k_x,k_y) &= \iint \mathrm{d}x\mathrm{d}y\ e^{-i(k_x x+k_y y)}\frac{\mathrm{d}p_h}{\mathrm{d}z}|_{z=0} \\
&= -\frac{f_0}{\pi H}\sum_{n\geq 0}\Lambda_n^2\sin\left(\Lambda_n h\right)\int_0^{+\infty}\mathrm{d}r\ rK_1\left(r\Lambda_n\right)\int_0^{2\pi}\mathrm{d}\theta\cos(\theta)e^{-ikr\cos(\theta-\phi)} \\
&= \frac{2if_0}{H}\sum_{n\geq 0}\Lambda_n^2\sin\left(\Lambda_n h\right)\cos(\phi)\int_0^{+\infty}K_1\left(r\Lambda_n\right)J_1(kr)r\mathrm{d}r \\
&= \frac{2if_0}{H}k_x\sum_{n\geq 0}\sin\left(\Lambda_n h\right)\frac{\Lambda_n}{k^2+\Lambda_n^2} \ .
\end{aligned} \tag{3.26}$$

The sum above can be computed from:

$$\sum_{n=1}^{\infty}\frac{n}{y^2+n^2}\sin(nx) = \frac{\pi}{2}\frac{\sinh(y(\pi-x))}{\sinh(\pi y)} \ . \tag{3.27}$$

Therefore one gets:

$$\tilde{f}(k_x,k_y) = if_0k_x\left(\cosh(kh)-\sinh(kh)\tanh(kH)\right) \ . \tag{3.28}$$

The case of an impulsion in an infinitely deep water is a limiting case of this expression, we easily see that:

$$\lim_{H\to+\infty}\tilde{f}(k_x,k_y) = if_0k_xe^{-kh} \ , \tag{3.29}$$

which is exactly Eq. (3.19). The displacement of the free surface then reads:

$$\zeta_{\mathrm{imp}}^H(\boldsymbol{x},t) = \frac{f_0}{2\pi\rho}\frac{x}{r}\int_0^{\infty}\mathrm{d}k\,k^2\left(\cosh(kh)-\sinh(kh)\tanh(kH)\right)J_1\left(kr\right)\frac{\sin(\omega(k)t)}{\omega(k)} \ . \tag{3.30}$$

with $\omega^2=(k+k^3)\tanh(kH\kappa)$ and κ^{-1} the capillary length. Note that one easily recovers Bühler's result in deep water by letting $H\to+\infty$.

3.5 Experimental results

In this section we present the experimental setup used by our collaborators in Tours to record the surface deformation both at rest when the water strider stand on the water surface and during the dynamic phase of propulsion.

3.5.1 Synthetic Schlieren method

Several profilometry techniques have been developed in the past for the measurement of the local topography of the air-water interface. Our collaborators in Tours, Jerome Casas and Thibaud Steinman have used the synthetic Schlieren method initially developed by Marc Rabaud and Frédéric Moisy [56]. The main feature of this innovative method consists in capturing from above, by means of a high speed video camera, images of a random dot pattern at the bottom of the basin transmitted through the liquid interface. Changes in the liquid-air interface topography result in a modification of the refracted dot pattern images.

If $\zeta(x,\ y)$ is the free surface displacement with respect to its equilibrium position, then $\delta\boldsymbol{d}(x,\ y)$ is the resulting modification of the refracted dot pattern. In this study [56], they demonstrated that the distortion field $\delta\boldsymbol{d}$ is simply proportional to the free surface gradient in the limit of small deformations.

Using Particle Image Velocimetry (PIV) techniques, digital image correlation algorithms are used to determine the apparent displacement field between the refracted image and the reference image obtained when the surface is flat. Eventually, a numerical integration of this displacement field, based on a least-square inversion of the gradient operator, reconstructs the instantaneous surface height.

3.5.2 Static measurement

As given by the vertical force balance of a water strider in a static situation see [49] and [57], the mass of the volume displaced by the insect at the free surface is equal to the mass of the insect. Indeed, given the free surface displacement $\zeta(x,y)$ resulting from an external pressure field $p_{\text{ext}}(x,y)$, and denoting $\hat{\zeta}(k)$ and $\hat{p}(k)$ their respective Fourier transform, the volume of the displaced fluid V_{d} can be directly linked to $\zeta(x,y)$ through:

$$V_{\text{d}} = \iint \mathrm{d}x\mathrm{d}y\ \zeta(x,y) = -\lim_{k\to 0}\hat{\zeta}(k)\ . \tag{3.31}$$

In addition, $\hat{\zeta}(k)$ being proportional to $\hat{p}(k)$ see [44], and given that $\hat{p}(0) = Mg$, one can eventually show that:

$$V_d = \frac{M}{\rho}\ , \tag{3.32}$$

where M is the mass of the insect and ρ denotes the water density. We predict that Archimedes' law is not modified by capillarity see Eq. (3.32). To determine the weight of individuals independently, insects were frozen and weighed just after defrosting with a microbalance. They were placed on absorbing paper during defrosting to remove water in excess. The weight of 70 individuals (from first instars to adults) measured with the microbalance was compared to the one predicted with the Schlieren technique. In the Fig. 3.3 we obtained an excellent agreement for all insects weights and validate the prediction of Eq. (3.32). The Schlieren technique can be considered as an accurate and non-intrusive technique that is appropriate for our task.

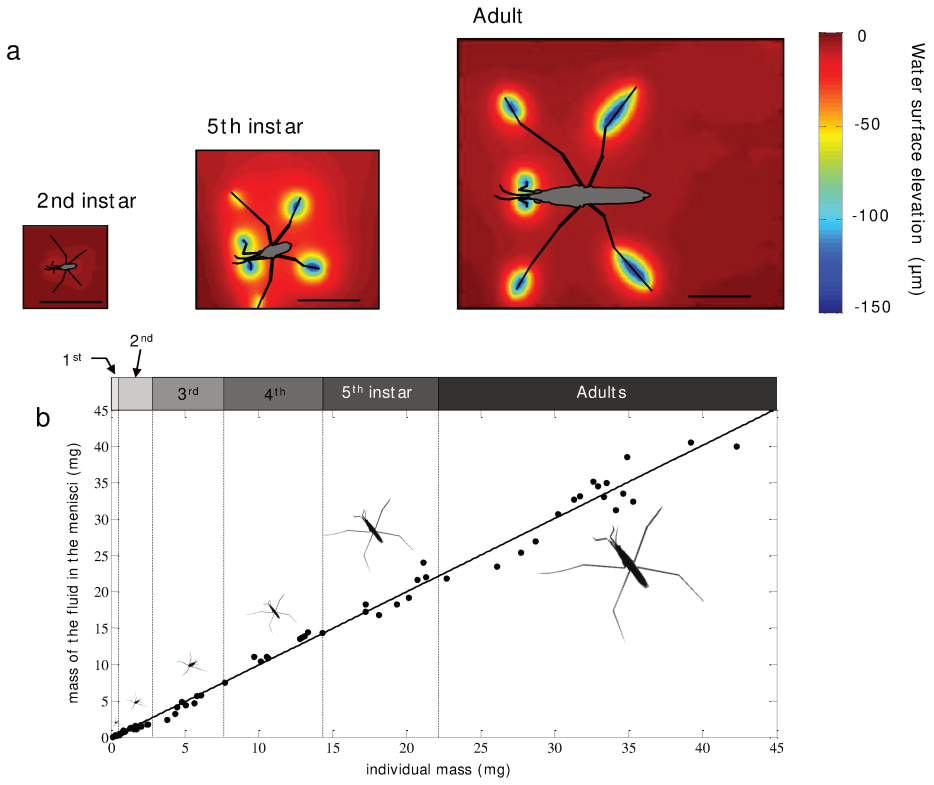

Figure 3.3 a. Static water surface deformation around non-moving *Gerris paludum* of 3 different instars. The color scale corresponds to the water surface elevation. The scale is given by the black line (5mm). b. Mass of displaced fluid as function of insect mass from first instars to adults.

3.5.3 Qualitative comparison, from impulsive to continuous forcing

The experimental observations of the surface displacement to the theoretical predictions developed in the previous section. We fit the theoretical surface of the continuous forcing to the experimental one which outputs the amplitude of the propulsive force f_0 see Eq. (3.3). Figure 3.5 (left column) shows the time resolved surface displacement around a water strider, during the stroke. The central column shows the theoretical prediction of the surface displacement following Bühler's theory for an impulsive forcing. We clearly see a poor qualitative agreement between experiments and the theoretical impulsive wave

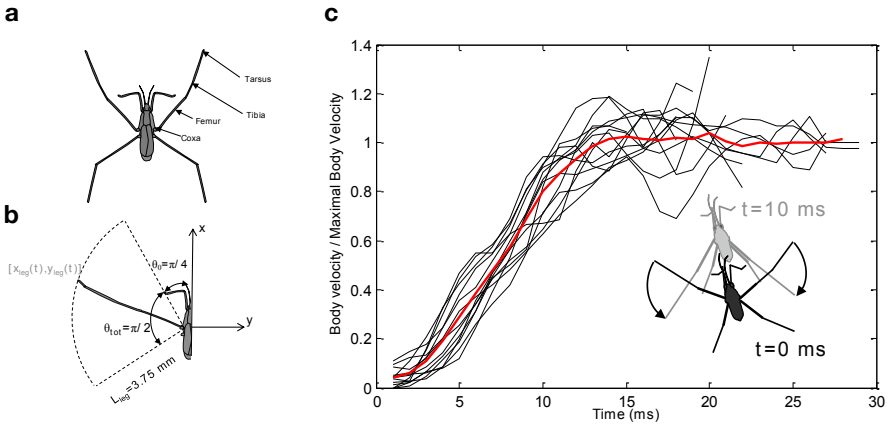

Figure 3.4 Body and leg kinetics during a stroke. a. Definition of the morphology of an insect leg. b. The water strider body is oriented along x axis. At rest, the 3.75 mm long median leg makes a $\pi/4$ angle with the x axis. During the 10 ms stroke, the leg rotates by approximately $\pi/4$ rad. c. Dimensionless velocity of the body for 10 strokes. The small sketch superimposed illustrates the movement of an individual, lasting 10 ms.

pattern. During the propulsion phase, we see a circular elongated wave, this shape results from the circular displacement of the leg during the stroke.

During a leg stroke, the leg is not localised in space as an impulsive forcing, but is following a circular trajectory. In order to account for the temporal extension of the rowing period, and consistent with the linearity of the governing equation, we now superimpose the impulsive solutions along the real leg's trajectory captured by the camera. Denoting $\boldsymbol{x}_{\rm leg}(t) = (x_{\rm leg}(t), y_{\rm leg}(t))$ for $t \in [0, \tau_{\rm imp}]$ the trajectory of a leg during the stroke phase, one obtains:

$$\zeta_{\rm cont}(\boldsymbol{x}, t) = \int_0^t \frac{{\rm d}s}{\tau_{\rm imp}} \Theta(s < \tau_{\rm imp})\, \zeta^H_{\rm imp}(\boldsymbol{x} - \boldsymbol{x}_{\rm leg}(s), t - s) \ , \tag{3.33}$$

where Θ denotes the Heaviside step function, and where $\zeta^H_{\rm imp}$ is given by Eq. (3.30). The time dependent positions of the tip of the left and right legs were obtained by fitting two parametric equations $\boldsymbol{x}_{\rm leg}(t)$=$(x_{\rm leg}(t), y_{\rm leg}(t))$ of the real legs trajectories recorded by camera. The Fig. 3.5 displays the result of the continuous forcing in the right forcing. The typical circular elongated wave produced by the legs is now very well reproduced by the theory with a continuous forcing in shallow water.
As mentioned above, fitting the theoretical surface to the experimental data by minimisation of the mean square difference allows us to obtain the total amplitude of the impulsive forcing f_0 as a fitting parameter. One obtains $f_0 = 1.3 \times 10^{-10}$ kg.m^4.s^{-1}.

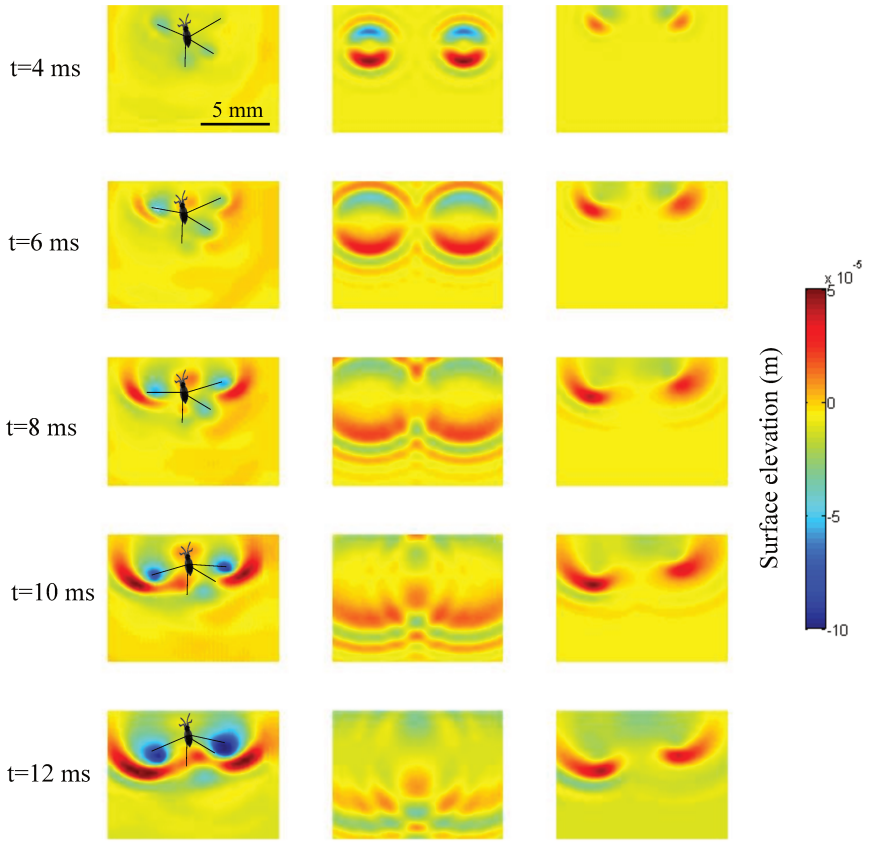

Figure 3.5 Comparison of the experimental surface elevation with theoretical predictions. The 1^{st} column represents the experimental surface elevation generated during the propulsion of a water strider ($m_{\text{gerris}} = 0.348$ mg, $V_{\text{gerris}} = 0.38$ m.s^{-1}). The 2^{nd} column represents the theoretical surface elevation produced by a single impulse in the direction of motion using ζ_{imp} as expressed in equation (3.21). The 3^{rd} column represents the results for a continuous forcing in shallow water along the trajectory of the water strider legs.

3.6 Conclusion

This study is a new step in the quantitative understanding of the water strider's locomotion mechanism. We have presented experiments and theory on the surface displacement generated by the water strider's leg strokes. Using the synthetic Schlieren method, we were able to dynamically measure the topography of the air-water interface during the water strider's leg strokes with unprecedented accuracy. We extended Bühler's study to account for finite depth consistent with the experimental conditions. We showed that accounting for the continuous forcing along the leg's trajectories was essential to reproduce the experimental wave patterns. This suggests that in the real conditions of the Gerris' natural habitat (including infinite depth: $H \gg \lambda$), Bühler's approach is very satisfactory by superimposing the impulsive solution along the leg's trajectories.

Second part

—

Glass transition in confinement

Chapter 4

Glassy polymers

Chapter 4 : Glassy polymers

↑ back to contents

Chapter abstract

In this chapter we recall physical properties of supercooled liquids and glasses. Then we introduce phenomenological laws such as the Adam and Gibbs laws, as well as theories such as the free volume theory [58]. We also propose a cooperative string model [59, 60] that will be used later on to understand the glass transition in confined samples of polymer glasses.

4.1 Introduction

For a long time glassmakers knew that during the cooling down of liquids made of oxydes, viscosity evolved to make a glass. A convention allowing the distinction between a liquid and a glassy amorphous solid was adopted, Tammann called this transition temperature T_g the glass transition temperature and correspond to a liquid with a viscosity of 10^{12} Pa.s^{-1}. It is now well established that around T_g a lot of different condensed phase chemicals such

as glycerol, polymers, oxydes, metals have the same dramatic increase of viscosity but also similar physical modification specific to the glassy state. Although obtaining a glass by cooling down rapidly is fairly simple, it has been so far impossible to fully understand the glass transition from a theoretical point of view. The main reasons are that the properties depends on how the glass was made, and these properties evolve with time. This is called the phenomenon of ageing.

4.2 Observation of the bulk glass transition

The most numerous data concerned enthalpy (via calorimetry) and volume (via dilatometry). Therefore in order to explain the experiments, we need to recall the basics properties of the thermodynamics of liquids.

4.2.1 Thermodynamical aspect of the glass transition

Through basics thermodynamics, we will highlight the relaxational signature of the glass transition temperature. When crossing the domain close to T_g during the cooling down process, we loose the possibility of finding the minimum of free-enthalpy, this is characteristic of the supercool liquid in a metastable state see Fig. 4.1. Therefore the system is macroscopically out of equilibrium but locally atoms or molecules could be in a local minimum of energy. On Fig. 4.2 , we observe that the first derivatives seems to be continuous but the second derivatives tends to have a brutal variation around T_g, the variation on the second order derivatives of the free-enthalpy experimentally defines the glass transition temperature. This observation could suggest that the glass transition is a second order phase transition, however we can check experimentally that it is not the case. For example we have for a second order transition:

$$\left(\frac{\mathrm{d}T}{\mathrm{d}P}\right)_{\text{transition}} = \frac{\Delta\chi}{\Delta\alpha_v} \tag{4.1}$$

where α_v is the coefficient of volume dilatation and χ is the coefficient of compressibility. In fact when we form a glass we usually have $\frac{\mathrm{d}T_g}{\mathrm{d}P} < \frac{\Delta\chi}{\Delta\alpha_v}$. Experimentally we observe that the value of T_g obtained depends linearly on the cooling rate. This obviously highlights the relaxational character of the glass transition.

When a liquid is at high temperature, the system reacts rapidly to the imposed variation of temperature and easily finds a new equilibrium point. If we consider a variation of volume with the temperature, it can be divided in two terms:

$$\frac{\mathrm{d}V}{\mathrm{d}T} = \left(\frac{\delta V}{\delta T}\right)_{\text{vib}} + \left(\frac{\delta V}{\delta T}\right)_{\text{conf}} \tag{4.2}$$

the variation due to the vibrational degree of liberty and the one due to the configurational degree of freedom. In a reasonable range of temperature, the vibrational terms are

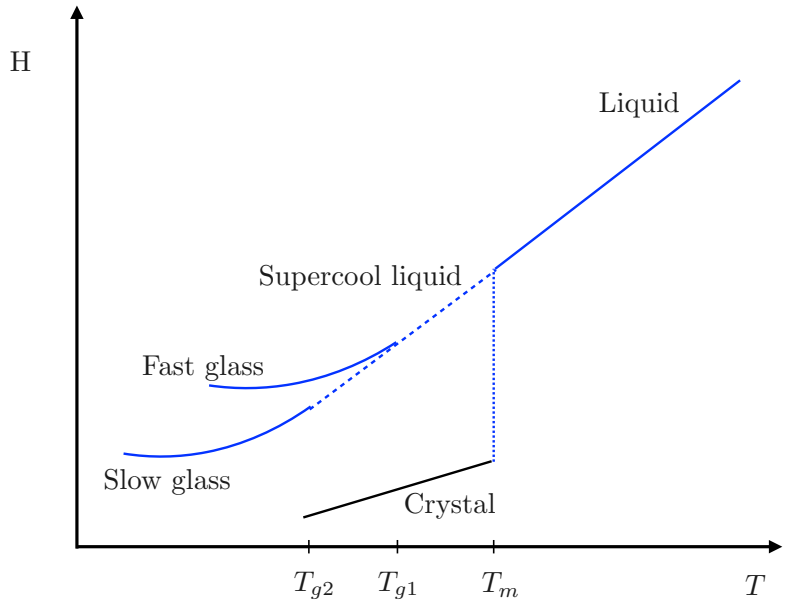

Figure 4.1 Free enthalpy as a function of the temperature, it decreases continuously with the temperature, the slope of the curve is the heat capacity which changes from liquid-like to solid-like values in the transition region. By cooling down the system rapidly, one can avoid the melting transition and reach a glassy regime, the property of the glassy regime depends on the cooling history.

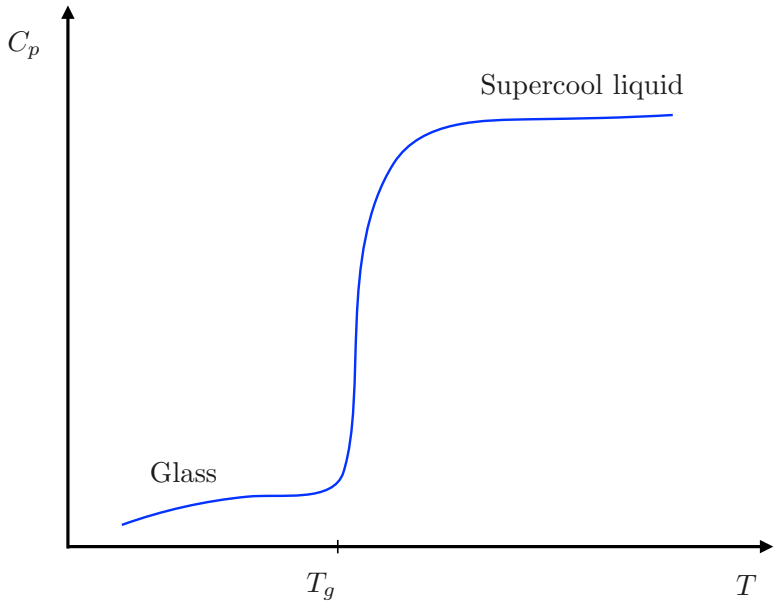

Figure 4.2 Heat capacity as a function of the temperature, heat capacity of glasses arises mostly from vibrational contributions, rotational and translational degrees of freedom have been frozen out.

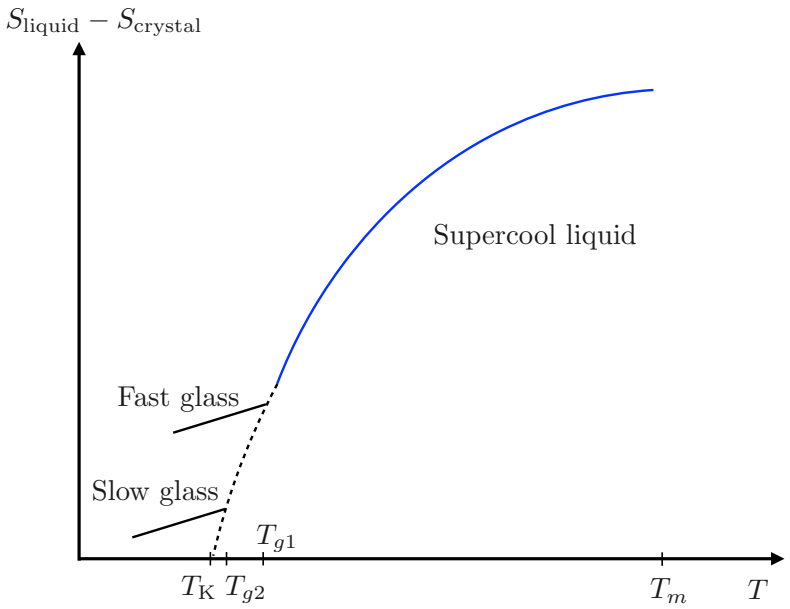

Figure 4.3 Excess of entropy of the supercool liquid as a function of the temperature, above the melting point, there is no excess of entropy. Supercooled liquid have excess of entropy because they have not lost all the entropy of melting given to the liquid on melting. At T_{K}, the supercool liquid has lost all of this excess entropy.

equal for the liquid, the crystal and the glass. Therefore the configurational term is the important value to understand the difference between a liquid and a solid. Indeed when we cool down a liquid its viscosity rises, the configurational changes are more and more difficult. The characteristic time of this re-arranging region increases particularly in the region of T_g. We can use the temperature dependence of the specific heat in order to calculate the entropy in a liquid or a solid phase :

$$S_i(T) = S_i(T_m) - \int_T^{T_m} \frac{C_i}{T} \mathrm{d}T \ . \tag{4.3}$$

Using this relation in both phase i, we can compute the difference of entropy between the two phases. The order of magnitude of S_{glass} is of the order of 5 J.K^{-1}.mol^{-1} for metallic glass to 50 J.K^{-1}.mol^{-1} for organic polymer glass.This value represents the configurational disorder which is only conceptual and has a real sense only if the time of the experiment is similar to the equilibrium time which is quasi infinite for a glass. Although we see on Fig. 4.3 with an extrapolation that Kauzmann define a temperature T_k where the "disorder" tends to 0 see Fig. 4.3. If a liquid could be supercooled below its Kauzmann temperature, therefore the displayed entropy would be lower than that of the crystal phase. This is known as the Kauzmann paradox. Physicists have proposed three possible argument to solve that paradox. First the heat capacity of the supercool liquid near T_{K} could be lower. Or a first order phase transition to another liquid state could occur before T_{K} with a smaller heat capacity for this phase. Or the supercool liquid should crystallize before reaching T_{K}.

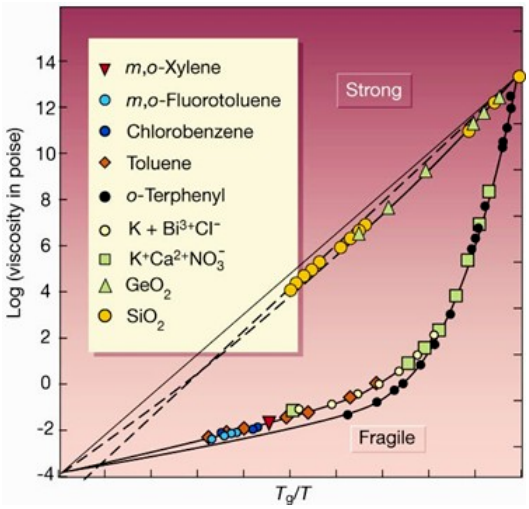

Figure 4.4 Log-viscosity as a function of the inverse of the temperature, Angell plot extracted from [61].

4.2.2 Dynamical aspect of the glass transition.

We want to present here some fundamental observations in glass-forming systems. At sufficiently high temperature, the typical relaxation time of a liquid is of the order of 1 picosecond. This time scale reflects the fact that in a liquid the particles can move easily and their trajectories looks like brownian motion. If we look at the temperature dependence of the relaxation time, we observe that an decrease in the temperature will change τ by order of magnitude. Understanding the microscopic mechanism responsible for this dramatic slowing down of the relaxation time is one of the main challenges. Although this slowing down can be easily explained there is no theory that describes all the glassy dynamics. Now if we plot $\ln(\eta)$ on an Angell plot, it shows that certain liquids follow Arrhenius law such as SiO_2 whereas others show an important deviation from Arrhenius. A popular way to describe the data is called the Vogel-Fulcher-Tammann law.

$$\eta(T) = \eta_0 \exp(\frac{A}{T - T_v}) \ , \tag{4.4}$$

this formula predicts the divergence at a finite temperature of the viscosity, called the Vogel temperature T_v. We present in the following a toy model that recovers this phenomenology based on Adam and Gibbs picture. In order to obtain a good understanding of the relaxation dynamics, it is useful to probe it at a microscopic level. We plot in Fig. 4.5 the time correlation function of a liquid at high temperature (dashed line) and the relaxation dynamics in a supercooled liquid (plain line). At short times we observe a ballistic dynamics, then at some point the particles will collide with their neighbours and therefore the correlation function decays exponentially. In the case of low temperature the pattern of the correlation function is more complex. At short time we still observe this ballistic behaviour then we reach a plateau corresponding to the behaviour found in a crystal, the reason of this reminiscent behaviour is due to a caging effect, in order to

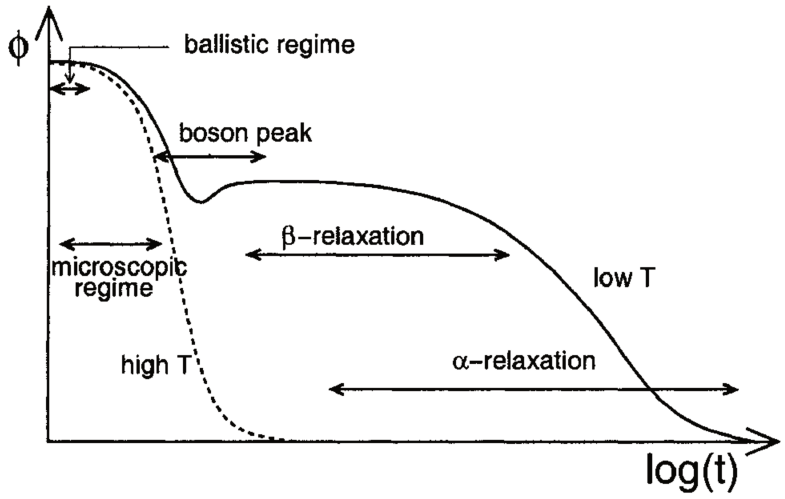

Figure 4.5 Time dependence of a correlation function. In dashed line a liquid, and in plain line a supercool liquid, graph extracted from [58].

make a large displacement in a supercool liquid, the particle has to escape the cage made of its neighbours. And then for longer time, the correlation function start to decay again, the particles have succeed to escape their cage. This final decay is well described by the stretched exponential known as the Kohlraush-Williams-Watts function [58]:

$$\phi(t) = A \exp\left(-\left(\frac{t}{\tau}\right)^{\beta}\right) \quad . \tag{4.5}$$

Historically, the relaxation process corresponding to the leaving of the cage is called the $\alpha-$ process and the plateau is called the $\beta-$process.

4.3 Theories of glass transition

From the observations we can draw the fundamental basis of every theory on glass transition.

- The glass transition is a universal manifestation for all liquids forming glasses.
- Even if there is a modification of thermodynamic quantities, it is not a phase transition but the disappear of configuration modes.
- The variation of the properties around T_g is still dramatic.
- This transition is mainly described by kinetic aspect.

- During the cooling down of a liquid, it doesn't reach a glassy state because some kinetic or topological barrier increases dramatically close to T_g.
- The relevant parameter is the molecular mobility τ_0, corresponding to the time of an elementary unit to move comparably to its size. The relaxation time depends on the temperature with a VFT phenomenology for $T > T_g$ and an Arrhenius phenomenology above T_g but with very high energy barrier.

In the following we are presenting some of the theories proposed to understand the glass transition. Obviously we cannot present all, in the New York Times David Weitz said: *There are more theories of glass transition than there are theorists who propose them.* We mention here the most successful theory known as the mode-coupling theory, however its complexity prevents us to use it to understand the confinement and polymeric effect that we are interested in later.

4.3.1 Theory of Adam and Gibbs

Adam and Gibbs in their seminal article [62], had the physical idea that in a glass-forming liquid, at low temperature, the relaxation process is the result of a sequence of individual events resulting in the re-arrangement of a subregion. This relaxation occurs due to local fluctuation of the enthalpy allowing collective motion. They consider an equilibrium isobar and isotherm of these small subsystems. The transition probability between two configurations is function of the size of the smallest possible region that can host such a rearrangement. In such a region we set z to be the number of structural units inside this region. There are two classes of subsystems n allowing rearrangement and $N - n$ that don't. $Z(z, P, T)$ is the partition function isothermal and isobaric of all the N subsystems and G the free enthalpy corresponding. Z' and G' correspond to the n rearranging subsystems.

$$\frac{n}{N} = \frac{Z'}{Z} = \exp\left(-\frac{G' - G}{k_b T}\right) = \exp\left(-\frac{z\Delta\mu}{k_b T}\right) \ . \tag{4.6}$$

By introducing $\Delta\mu = (G' - G)/z$ the enthalpic barrier per structural unit or particle, and using the fact that the probability that a system of size z makes a rearrangement $W(z, T)$ is proportional to n/N, therefore:

$$W(z, T) = A \exp(-\beta z \Delta\mu) \ . \tag{4.7}$$

From that we obtain the average transition probability per structural unit:

$$\langle W(T) \rangle = \frac{1}{N} \sum_{z=1}^{N} z u(z, T) W(z, T) \ , \tag{4.8}$$

with $u(z, T)$ the number of subsystem of size $z \in [1, N]$. In fact this sum will start at z^* the cooperative onset or the smallest clusters of structural unit able to rearrange.

Assuming that $u(z,t)$ do not depends a lot on z therefore we have:

$$\langle W(T)\rangle = B\exp(-\beta z^*\Delta\mu)\ . \tag{4.9}$$

Thus the relaxation dynamics is dominated by the smallest possible cluster of structural unit rearranging. The cooperative onset z^* determines how many structural units participate in a typical relaxation event. This value corresponds to an entropy $S^* = k_b\ln(2)$ and we have $z^*S_{\text{conf}} = N^*S^*$.

$$\langle W(T)\rangle = B\exp\left(-\frac{N^*\ln(z)\Delta\mu}{TS_{\text{conf}}}\right)\ . \tag{4.10}$$

Invoking ergodicity, we directly obtain the results of Adam and Gibbs:

$$\tau(T) \propto \exp\left(\frac{C}{TS_{\text{conf}}}\right) \tag{4.11}$$

A simple thermodynamic calculus allows us to compute the configurational entropy by integrating the enthalpy:

$$S_{\text{conf}} = N\Delta C_p\ln(T/T_k)\ , \tag{4.12}$$

with ΔC_p the difference of specific heat between the liquid and the glassy state. Eventually one gets:

$$\tau(T) \propto \exp\left(\frac{D}{T\ln(T/T_k)}\right)\ . \tag{4.13}$$

4.3.2 Free volume theory

Cohen and Turnbull [63] had made the hypothesis that the molecular transport is due to the motion of molecules in holes which size should be superior to a critical size. We consider here a material composed of spheres with a hard or a Lennard-Jones potential. If we consider two particles A and B as in Fig. 4.6 we see that the particle A is not able to make a relaxation corresponding to leave its cage, but the particle B has enough place to relax. The free volume theory attemps to relate the diffusivity of the particle to the distribution of free space in the material. The free volume per particle is defined has following:

$$v_f = v - v_0\ , \tag{4.14}$$

with v_0 the excluded volume per particle and v the volume per particle. The aim is to determine the probability distribution of v. By decomposing the system in smaller region

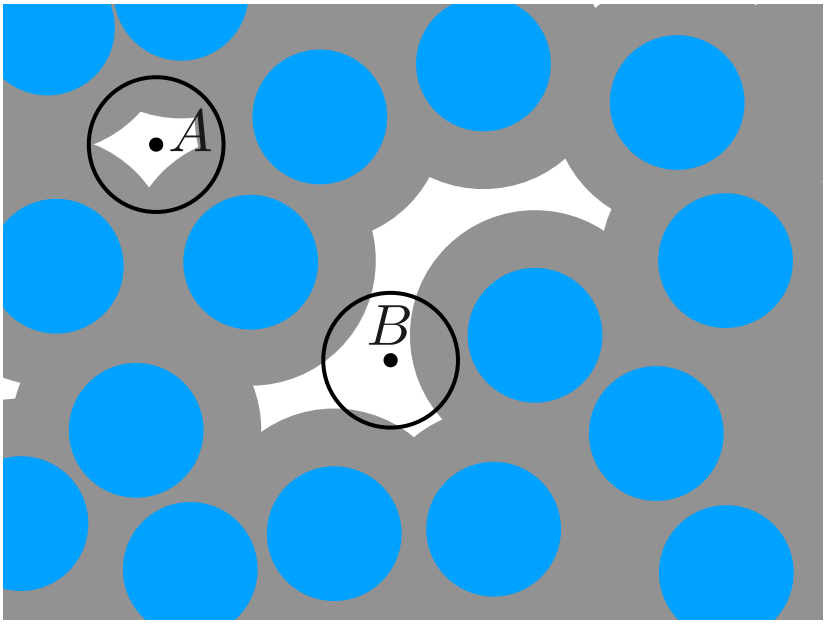

Figure 4.6 In white the accessible volume for the particles A and B. The particule in A is caged by its neighbours and cannot relaxes however the particle B is able to move a relaxation motion.

j, with n_j structural units with an average free volume v_{fj}:

$$C\sum_j n_j v_{fj} = N v_{fm} \ , \tag{4.15}$$

$$\sum_j n_j = N \ , \tag{4.16}$$

where $C \in [0.5, 1]$ is an overlap factor that accounts for free volume that might be shared by adjacent cells in the lattice. The number of configuration rearranging the space reads:

$$\Omega = \frac{N!}{\Pi_j n_j!} \tag{4.17}$$

We seek to maximise for entropic reasons the number Ω of distinguishable ways that free volume v_{fi} per subsystem can be redistributed among n_i subsystems, subject to the previous two constraints. Using Stirling formula one gets:

$$\ln(\Omega) = \frac{1}{2}\ln(2\pi) + \left(N + \frac{1}{2}\right)\ln(N) - \sum_j \frac{1}{2}\ln(2\pi) + \left(n_j + \frac{1}{2}\right)\ln(n_j) \tag{4.18}$$

In order to verify the two constraints we use two Lagrange multipliers λ_1 and λ_2, thus we have to maximise F:

$$F = \ln(\Omega) + \lambda_1\left(N - \sum_j n_j\right) + \lambda_2\left(N v_{fm} - C\sum_j n_j\right) \tag{4.19}$$

therefore we have:

$$\partial_{n_i} F = -\ln(n_i) - \lambda_1 - \lambda_2 C v_{fi} = 0 \ , \tag{4.20}$$

$$\partial_{\lambda_1} F = N - \sum_j n_j = 0 \ , \tag{4.21}$$

$$\partial_{\lambda_2} F = N v_{fm} - C \sum_j n_j v_{fj} = 0 \ . \tag{4.22}$$

Using a continuous description one easily gets the distribution of free volume:

$$p(v) = \frac{C}{v_{fm}} \exp\left(-\frac{Cv}{v_{fm}}\right) \ . \tag{4.23}$$

In condensed matter, a relaxation process needs two conditions:

- enough space next to the test particle
- enough energy for the test particle

within the framework of the free volume theory, in order to have enough space, we should have an entropic coalescence of small free volume up to reach the critical space needed to relax. In this condition we can state that if the free volume available is below a structural unit size v_0, the diffusion constant is $D = 0$, if $v > v_0$ therefore $D \sim D_0$ under the assumption that the diffusivity weakly depends on the free volume available above v_0. Therefore the effective diffusivity reads:

$$D^* = D_0 \exp\left(-\frac{Cv_0}{v_{fm}}\right) \quad , \tag{4.24}$$

where $D_0 = \nu_D \lambda^2$, ν_D is the Debye frequency and λ a molecular distance. The timescale associated to this diffusion constant is simply the mean time for a structural unit to travel a molecular distance λ:

$$\tau = \frac{\lambda^2}{D} = \tau_0 \exp\left(\frac{Cv_0}{v_{fm}}\right) \ . \tag{4.25}$$

The free volume distribution varies with the temperature, and we can link them with the linear expansivity. We assume the existence of free volume only above a certain temperature T_v, therefore we have for $T > T_v$:

$$v_{fm} = v_0(\alpha_l - \alpha_g)(T - T_v) \ . \tag{4.26}$$

From this results the Vogel-Fulcher-Tammann phenomenology:

$$\tau = \tau_0 \exp\left(\frac{\Delta\alpha^{-1}}{T - T_v}\right) \tag{4.27}$$

4.3.3 Cooperative string theory

In a supercooled liquid, due to crowding and caging [64], local rearrangements seem to require the cooperative participation of a growing number of molecules as the temperature T is decreased. This was related through phenomenological arguments to the vanishing of the free volume needed for relaxation, and could lead to the tremendous slowing down of glassy dynamics described by the empirical time-temperature superposition. This relaxation process defines a temperature-dependent length scale $\xi(T)$ for the cooperatively rearranging regions, and thus for glassy dynamics in the bulk. Furthermore, within some degree of poly-dispersity in size, numerical simulations, and experiments, suggested that those regions might take the form of unidimensional chains – the so-called *cooperative strings* [65, 66, 67, 68]. We developed a minimal kinetic model based on those ideas, that is successful in reproducing bulk phenomenology and will be useful to understand confined phenomenology [59]. For the sake of simplicity, we map the real liquid state to a simple hard-sphere liquid and thus fully neglect the enthalpic contributions in the activation barriers for relaxation. Stated differently, we assume that entropic effects are dominant in the critical slowing down of supercooled liquids. This is also what the Gibbs-DiMarzio approach to glass formation in polymers would suggest, with the underlying transition essentially determined by a vanishing of the configurational entropy.

Let us consider a dense assembly of small molecules with size λ_V and average intermolecular distance λ. The volume fraction is thus $\phi \propto (\lambda_V/\lambda)^3$. A test molecule sits in a cage of volume $\sim \lambda^3$, with gates of length $L \sim \lambda - \lambda_V$. We set that a typical non-cooperative liquid-like local relaxation requires $L > L_c = \lambda_c - \lambda_V$, or equivalently λ to be larger than λ_c – the so-called onset of cooperativity, with volume fraction ϕ_c (see Fig. 4.7). Also, when $\lambda \sim \lambda_V$, the gates are completely closed ($L \sim 0$) and the system is at kinetic arrest, with volume fraction ϕ_V. For $\lambda_V < \lambda < \lambda_c$, the relaxation is possible but necessarily collective. It requires a random string-like cooperative motion involving at least $N^* - 1$ neighbours of the test molecule, that provide a total space $(N^* - 1)L \sim L_c - L$ by getting in close contact with each other. The test molecule thus sees a temporary larger gate, of length L_c, and can exit the cage. Therefore, one gets the scaling expression of the minimal number of molecules needed for a local relaxation, *i.e.* the so-called cooperativity (see

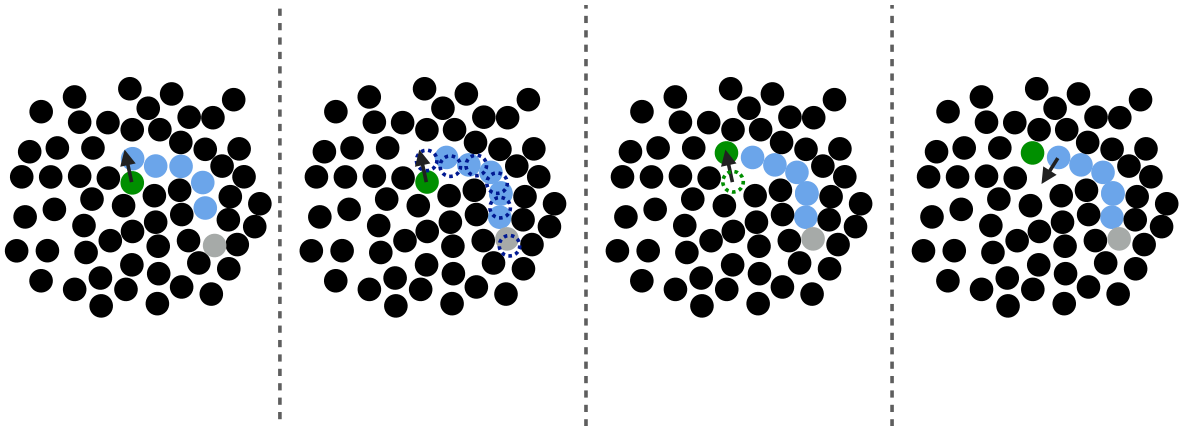

Figure 4.7 Model of cooperative string relaxation, the test particle in green needs cooperative rearrangement from its neighborhood in order to relax.

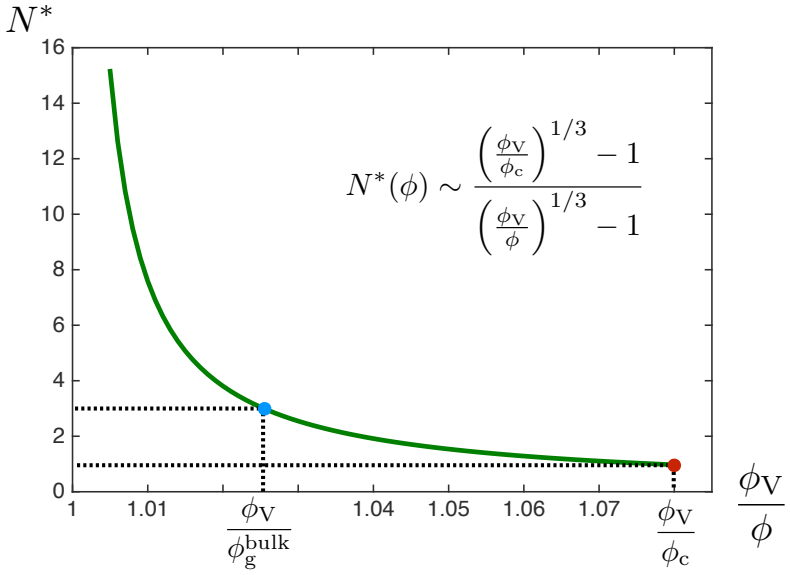

Figure 4.8 Bulk cooperativity as a function of the inverse of the density for the polystyrene.

Fig. 4.8):

$$N^*(\phi) = \frac{\left(\frac{\phi_V}{\phi_c}\right)^{1/3} - 1}{\left(\frac{\phi_V}{\phi}\right)^{1/3} - 1} \ . \tag{4.28}$$

As expected, this expression reaches 1 at the cooperative onset ϕ_c, where solitary rearrangements are allowed, and diverges at the kinetic arrest point ϕ_V. Note that the bulk glass-transition point ϕ_g^{bulk} lies somewhere in between those two extreme values. By introducing the necessity of coherence between molecular motions within a cooperative rearrangement, the probability for the motion of $N-1$ consecutive particles coherently with the motion of the first test particle scale like $\sim \epsilon^{N-1}(1-\epsilon)$, ϵ is an elementary coherence probability and the factor $1-\epsilon$ expresses the incoherence of the $N+1$th particle. Finally we can express the probability of a cooperative relaxation involving N particles:

$$P_N(\phi) = \frac{1}{\tau_c \lambda^3}(1-\epsilon)\epsilon^{N-1}\Theta\left(N - N^*\right) \ , \tag{4.29}$$

where Θ is the Heaviside function. Summing over all possible chains lengths N, we obtain the probability of relaxation:

$$P(\phi) \sim P_c \epsilon^{N^*-1} \tag{4.30}$$

the relaxation is entirely determined by the cooperativity N^* and is exponentially decay-

ing with increasing N^* ($\epsilon << 1$). Introducing an ergodic correspondence between bulk relaxation time τ and the probability of relaxation through $\tau P\lambda^3 \sim 1$

$$\frac{\tau_0}{\tau} = \left(\frac{\tau_0}{\tau_c}\right)^{N^*} , \tag{4.31}$$

where $\tau_c \sim 1$ ps is a typical liquid-like relaxation time at the cooperative onset, and $\tau_0 \sim 10$ fs is a molecular time scale. Our description thus naturally leads to the Adam-Gibbs phenomenology. While the proposed approach does globally use free volume to correlate to dynamics, it does not necessarily mean that local regions with higher free volume are always faster in a real material, despite indications that this might be true. In fact, the effect of coherence of molecular motion is at least as important as the free volume itself. If parts of the sample had a higher density, but also a higher coherence factor τ_0/τ_c, then those parts may relax faster. All of this is not considered in the context of the current mean-field approach, but it does mean that we do not necessarily have to assume a strict correlation between local density and local mobility.

Since, in the temperature range considered, the thermal expansion coefficient $\alpha = -(1/\phi)\mathrm{d}\phi/\mathrm{d}T$ of the supercooled liquid is almost constant, one has:

$$\phi(T) = \phi_V[1 - \alpha(T - T_V)] , \tag{4.32}$$

where $\phi(T_V) = \phi_V$ defines the Vogel temperature T_V. Therefore, our description naturally leads to the Vogel-Fulcher-Tammann time-temperature superposition without incorporation of any enthalpic contribution, through the use of Eqs. (4.28), (4.31) and (4.32):

$$\tau(T) = \tau_0 \exp\left(\frac{A}{T - T_V}\right) , \tag{4.33}$$

where $A = (T_c - T_V)\ln(\tau_c/\tau_0)$, and with $\phi(T_c) = \phi_c$ by definition of the onset temperature T_c. As a first remark, τ_c/τ_0 should be a constant only for hard spheres. For a real liquid, the latter dimensionless relaxation time is rather expected to follow an Arrhenius law $\tau_c/\tau_0 = \exp(T_a/T)$, where $k_B T_a$ is an activation energy barrier proportional to the cohesive interaction strength, and k_B is the Boltzmann constant. In that case, Eq. (4.33) would be replaced by the leading-order expression near the kinetic-arrest point:

$$\tau \simeq B\,\tau_0 \exp\left(\frac{C}{T - T_V}\right) , \tag{4.34}$$

where $C = T_a(T_c - T_V)/T_V$ and $\ln B = -C/T_V$ are two constants. Thus, the Vogel-Fulcher-Tammann form is still recovered asymptotically, which means, in this type of description, that the details of the enthalpic contributions are not essential to capture the critical slowing down in an ideal supercooled liquid. As a second remark, the Vogel-Fulcher-Tammann law is only valid over some temperature range, and in reality we do not expect the relaxation times to actually diverge. This approach should rather be considered as a high-temperature approximation. The low-temperature behavior lies beyond the scope

of the present minimal description, as it might involve the fine details of the real energy landscape. As the bulk relaxation process presented here consists of random cooperative strings involving N^* molecules, one can minimally describe them through ideal random walks. The length scale ξ of the cooperatively rearranging regions is thus of the form $\xi \sim \lambda\sqrt{N^*}$, near the kinetic arrest point. Invoking Eqs. (4.28) and (4.32), one obtains the temperature-dependent expression of the cooperativity:

$$N^*(T) = \frac{T_c - T_V}{T - T_V} \ , \tag{4.35}$$

and thus an asymptotic expression for the associated length scale:

$$\xi(T) = \lambda_V \sqrt{\frac{T_c - T_V}{T - T_V}} \ . \tag{4.36}$$

As a consequence of this description, the cooperative length diverges at the Vogel temperature with a $-1/2$ power law, and is comparable to the molecular diameter at the cooperative onset.

4.4 Glass transition temperature measurement

4.4.1 Calorimetric measures

The most common method to obtain the glass transition temperature of an amorphous polymer is using calorimetric measurement. If we consider a graph of the calorific capacity as a function of the temperature, there are four ways to determine the glass transition temperature. Therefore the glass transition temperature depends on the used convention. T_{g1} corresponds to the beginning of the structural evolution of the system, T_{g2} corresponds to the temperature at which C_p is equal to the average of C_p(liquid) and C_p(glass), T_{g3} corresponds to the point of maximal speed of structural relaxation, and T_{g4} when the system first reach the metastable state. Considering the kinetic aspect of the glass transition, we expect that the glass transition temperature vary with the cooling rate k. The energy barrier $\Delta H_k \sim 430$ kJ.mol^{-1}. The very high energy barrier corresponds to the collective character of the glass transition.

4.4.2 Ellipsometric measures

Ellipsometry is an optical technique of characterization and surface analysis, based on the change of state of polarization of light, by reflection of light on the flat surface of a sample A collimated light beam is polarized linearly through a polarizer. The beam is reflected on the sample, which modifies its state of polarization. It then passes into an analyzer before arriving in a mirror extending the beam in an optical fiber connected to the spectrometer. It is from this principle that the very high sensitivity of the measurement and its wide

range of use result. Thus, an ellipsometer physically measures only two parameters: the state of polarization of the light and the intensity of the reflected radiation. The physical parameters of the analyzed sample come from models of wave-matter interactions. This technique is very accurate for thin polymer films, where glass transition dependence with the film thickness have been reported. The index of refraction can be characterized by ellipsometry. It measures the reflection coefficient and the ratio of phase shift of the parallel and perpendicular components of elliptically polarized light reflected from a surface. Glass transition temperature can be determined from the thickness and index of refraction due to the difference in thermal expansion coefficient.

4.5 Conclusion

In this section we have presented some theories of glass transition and particularly our cooperative string model. This model captures basic features of the glass transition such as the Vogel-Fulcher-Tamman phenomenology and has the advantage of capturing the physics of glass transition shift in confined geometry presented in the next chapter.

Chapter 5

Glass transition in confinement

Chapter 5 : Glass transition in confinement

↑ back to contents

Chapter abstract

Understanding the nature of the glass transition and its physical properties remains a huge challenge in solid state physics. The observed dynamics of a glass forming liquid close to the glass transition temperature follows the Vogel-Fulcher-Tamman phenomenology, the viscosity diverges at a finite temperature[69, 70, 71]. This phenomenology can be explained by the Adam-Gibbs description[62] of cooperative rearrangement in supercool liquids. The length scale of these cooperative regions has raised an important interest[72, 73]. The study of glassy polymer films is probably the most prominent physical measurement of this characteristic length ξ. In polystyrene thin films, it is now well established that the measured glass transition temperature decreases as the film thickness is reduced. Similarly, the same behavior has been observed in nano-sphere[74, 75, 76], nano-pores[73] and other geometries.

In the previous chapter, we developed a bulk toy model for the relaxation of supercooled liquids, here we model the interfacial effects to recover the observed phenomenology of thin films[59] and nano-spheres[60]. We also discuss the influence of various boundaries. Eventually we provide a model of attractive interface and study extensively the case of the supported film.

5.1 Cooperative strings model

5.1.1 Effects of confinement

Experiments have shown that at a free interface we observe an higher surface mobility[77, 78, 79, 80, 81]. The effect of the free interface is introduced in our model by truncating the cooperative strings at the boundary, leading to a smaller average local cooperativity $N_s^*(\mathbf{r}, T)$, where $\mathbf{r}$ is the position of the test particle (see Fig.5.1). When the distance of the

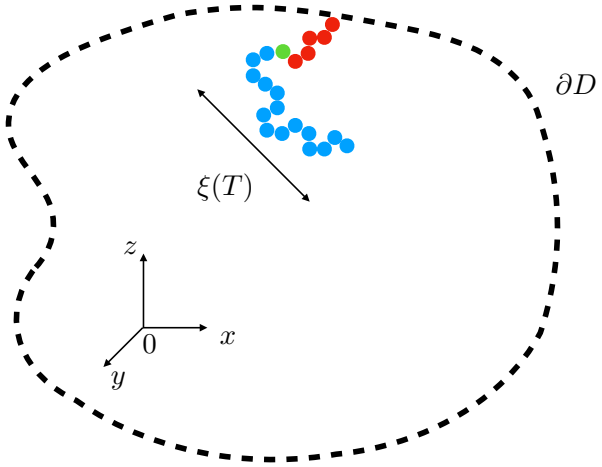

Figure 5.1 Two string like cooperative strings inside a glassy material of volume V. The material belongs to the domain D and is delimited by its boundary ∂D. The relaxation of the test particle in green close to the interface can occur trough either a bulk cooperative string of size ξ in blue or a truncated strings by a shorter path touching the free interface in red.

test particle is large in comparison to $\xi(T)$, the free interface is not reached with smaller paths than N^*, therefore $N_s^* \sim N^*$. By contrast, when the distance to the interface goes to 0, the cooperativity goes to 0 as well due to the absence of caging at the free boundary. Therefore the local cooperativity in presence of a free interface reads:

$$N_s^*(\mathbf{r}, T) = \langle \min(N^*, l) \rangle = N^*(T) f(\mathbf{r}, T) \ , \tag{5.1}$$

with l the path length of the first passage to the interface, the probability distribution of l depends on the boundary shape. The relaxation time in presence of a free interface is obtained by replacing N^* by $N_s^*(\mathbf{r}, T)$[59] and one gets the local relaxation time:

$$\frac{\tau_s(\mathbf{r}, T)}{\tau_0} \sim \left(\frac{\tau}{\tau_0}\right)^{f(\mathbf{r},T)} , \tag{5.2}$$

the function f measures how the free interface enhanced the glassy dynamics inside the material. Using experimental criteria on the relaxation time ($\tau_g \sim 100$ s) and on "averaging" the local relaxation time (for example in a thin polymer film, we consider that the glass transition occurs when half of the volume is liquid) we can relate T_g to the studied object's scale.

5.1.2 Diffusion modeling

From experimental[67] and numerical[65, 66, 82] insights, a cooperative region is modeled here by brownian motion, thus its path statistics verifiy the diffusion equation. This approximation is especially good near the kinetic arrest point. The cooperative process described in the previous chapter 4.3.3 involves random strings of particles .The advantage of working near the kinetic-arrest point is to get a Brownian description, and thus tractable analytical results using first-passage probability densities. First-passage densities are determined using the path density $P(\mathbf{r_1}, l|\mathbf{r})$ of dimensionless length l inside the domain D delimited by the free interface ∂D. This dpath density solves the following diffusion equation:

$$\partial_l P = \frac{1}{2}\Delta P , \tag{5.3}$$

$$P(\mathbf{r_1}, 0|\mathbf{r}) = \delta(\mathbf{r} - \mathbf{r_1}) , \tag{5.4}$$

$$P(\mathbf{r_1}, l|\mathbf{r}) = 0 , \ \forall \mathbf{r_1} \in \partial D . \tag{5.5}$$

For the classical diffusion equation, by deriving the Fokker-Planck equation, one can show that the diffusion coefficient is $\frac{a^2}{2\tau}$ with τ the elementary time step and a the elementary spatial step. The analogous length in our model is the trajectory length L of a cooperative string. The elementary step for this length is a which is the elementary spatial step. Therefore the diffusion coefficient of our equation is $\frac{a}{2}$. In our model the elementary spatial step is $a = \lambda_v$ defined in 4.3.3 as the inter-particular distance at the kinetic arrest point. Our diffusion equation then reads:

$$\partial_L P = \frac{\lambda_v}{2}\tilde{\Delta} P , \tag{5.6}$$

with $\tilde{\Delta}$ the laplacian with respect to the spatial coordinates. Therefore, using the dimensionless variables $l = L/\lambda_v$, $z = Z/\lambda_v$, one gets the dimensionless diffusion equation defined in Eq. 5.3. In the rest of the thesis all the lengths, constants or variables will be dimensionless unless otherwise stated.

The previous equation is a diffusion equation in a bounded euclidean domain with Dirichlet boundary condition. [1] The spectrum of the Laplace operator is known to be discrete. Among the important properties on this spectrum we have[83, 84, 85]:

- The eigenvalue λ_n are positive and increasing with $n \in \mathbb{N}_+^*$.
- The corresponding eigenfunctions $u_n(\mathbf{r})$ form a complete basis on $L_2(D)$
- The completeness of the eigenfunctions can be expressed as:

$$\sum_{n=1}^{\infty} u_n(\mathbf{r}) u_n^*(\mathbf{r}') = \delta(\mathbf{r} - \mathbf{r}') \ . \tag{5.7}$$

- The eigenfunction are normalized with the L_2 norm :

$$\int_D \mathrm{d}\mathbf{r} |u_n(\mathbf{r})|^2 = 1 \ . \tag{5.8}$$

- Therefore the heat kernel of Eqs[5.3-5.5] reads:

$$G(\mathbf{r}, \mathbf{r}', l) = \sum_{n=1}^{\infty} u_n(\mathbf{r}) u_n^*(\mathbf{r}') e^{-\lambda_n l} \ . \tag{5.9}$$

Therefore with the initial condition, one can get for any bounded domains D, the density of path:

$$P(\mathbf{r_1}, l|\mathbf{r}) = \sum_{n=1}^{\infty} u_n(\mathbf{r}) u_n^*(\mathbf{r_1}) e^{-\lambda_n l} \ . \tag{5.10}$$

From the path density, one can get the survival probability of a path of length l inside the domain D (i.e. a path of length l that hasn't touch yet the absorbing boundary) and eventually the first passage distribution $g(\mathbf{r}, l)$. The survival probability inside the domain D reads:

$$S_{\mathbf{r}}(l) = \sum_{n=1}^{\infty} u_n(\mathbf{r}) \int_D \mathrm{d}\mathbf{r_1} u_n^*(\mathbf{r_1}) e^{-\lambda_n l} \ . \tag{5.11}$$

using the mean value theorem one easily gets that:

$$S_{\mathbf{r}}(l) = V \sum_{n=1}^{\infty} a_n u_n(\mathbf{r}) e^{-\lambda_n l} \ . \tag{5.12}$$

with $\int_D \mathrm{d}\mathbf{r_1} u_n^*(\mathbf{r_1}) = V a_n$, where $V = \mathrm{Vol}(D)$ (dimensionless volume) and $|a_n| \leq 1$. By taking the opposite of the derivatives of the survival probability, one gets the first passage

[1] To take into account a supported interface that is not a free volume reservoir, we should introduce a reflecting boundary condition known as a Neumann boundary condition ($\partial_n P(\mathbf{r_1}, l|\mathbf{r}) = 0 \ , \ \forall \mathbf{r_1} \in \partial D$, where ∂_n is the normal derivatives pointed outwards the domain). This won't modify the discussion.

distribution:

$$g(\mathbf{r}, l) = V \sum_{n=1}^{\infty} \lambda_n a_n u_n(\mathbf{r}) e^{-\lambda_n l}. \tag{5.13}$$

The local cooperativity in presence of a free interface is computed using the first passage distribution $langle \min(N^*(T), l)\rangle$, it reads:

$$N_s^*(\mathbf{r}, T) = N^*(T) V \sum_{n=1}^{\infty} \frac{1}{\lambda_n} a_n u_n(\mathbf{r})(1 - e^{-\lambda_n N^*}). \tag{5.14}$$

5.2 Exact results for simple domains

We now list the examples of simple domains, in which symmetries allows for variable separation and thus explicit representations of eigenfunctions.

5.2.1 Free standing film

A free standing film is a volume delimited by two free interface in $z = 0$ and $z = h$, the natural variable separation yields:

$$u_n(z) = \sqrt{\frac{2}{h}} \sin(\omega_n z) \ , \tag{5.15}$$

and,

$$\lambda_n = \frac{\omega_n^2}{2} = \frac{\pi^2 n^2}{2h^2} \ \forall n \geq 1 \ . \tag{5.16}$$

The local cooperativity reads:

$$N_s^*(z, T) = \frac{8N^*}{h} \sum_{n>0, n \text{ odd}}^{\infty} \frac{\sin(\omega_n z)}{\omega_n^3} \left(1 - e^{-\frac{\omega_n^2}{2} N^*}\right) \tag{5.17}$$

5.2.2 Supported film

A supported film is delimited by a reflecting interface in $z = 0$ and a free interface (absorbing boundary) in $z = h$, the decomposition of the laplacian leads to:

$$u_n(z) = \sqrt{\frac{2}{h}} \sin(\omega_n z) \ , \tag{5.18}$$

and,

$$\lambda_n = \frac{\omega_n^2}{2} = \frac{\pi^2 (2n+1)^2}{8h^2} \ \forall n \geq 0 \ . \tag{5.19}$$

The local cooperativity reads:

$$N_s^*(z,T) = \frac{4N^*}{h}\sum_{n=1}^{\infty}\frac{\sin(\omega_n z)}{\omega_n^3}\left(1-e^{-\frac{\omega_n^2}{2}N^*}\right) \tag{5.20}$$

We see that the cooperativity is equal to the cooperativity of a free standing film of thickness $2h$. This illustrates the property of reflection of the brownian motion and is in agreement with the experimental observations. Therefore, the mobile layer will have the same size, and the glass transition as a function of the thickness is obtained using the transformation $h \to 2h$.

5.2.3 Cylinder

We consider a cylinder of radius R with absorbing condition at its boundary $P(r=R)=0$. The decomposition of the laplacian leads to:

$$u_n(r) = \frac{\sqrt{2}}{RJ_1(\omega_n R)}J_0\left(\omega_n r\right) \ , \tag{5.21}$$

with ω_n solving:

$$J_0(\omega_n R) = 0 \ , \tag{5.22}$$

and,

$$\lambda_n = \frac{\omega_n^2}{2} \quad . \tag{5.23}$$

Thus the cooperativity reads:

$$N_s^*(r,T) = \frac{4N^*}{R}\sum_{n=1}^{\infty}\frac{J_0\left(\omega_n r\right)}{\omega_n^3 J_1(\omega_n R)}\left(1-e^{-\frac{\omega_n^2}{2}N^*}\right) \ . \tag{5.24}$$

5.2.4 Sphere

We consider a sphere of radius R with absorbing boundary condition. The Eigenfunction of the Laplacian reads:

$$u_n(r) = \sqrt{\frac{2}{R}}\frac{\sin\left(\omega_n r\right)}{r} \ , \tag{5.25}$$

with,

$$\lambda_n = \frac{\omega_n^2}{2} = \frac{\pi^2 n^2}{2R^2} \ \forall n \geq 1 \ . \tag{5.26}$$

Thus the cooperativity reads:

$$N_s^*(r,T) = \frac{4N^*}{r}\sum_{n=1}^{\infty}(-1)^{n-1}\frac{\sin(\omega_n r)}{\omega_n^3}\left(1-\exp\left(-\frac{\omega_n^2}{2}N^*\right)\right) \ . \tag{5.27}$$

5.3 Theoretical results

5.3.1 Reduction of the glass transition temperature

We can now determine the effective glass transition temperature as a function of the size of the glassy material. We use the following experimental criterium: half of the volume of the glassy sample must relax to a liquid-like state [86, 87] . Using this criterium together with Eq. (5.2) that links implicitly the system size to the effective glass transition temperature, we obtain the expected result. First it has been compared to thin film experiments [59], the theory was compared to dilatometric measurements on polystyrene supported thin film, the results of the theory is plotted in the Fig. 5.2, this graph is extracted from the following article [59]. The theory as two adjustable parameters, the critical interparticular distance $\lambda_v \sim 3.7$ nm which is comparable to the persistent length of the polystyrene, and the Vogel temperature $T_v \sim 322$ K which is close to the reported value 327 K. On the

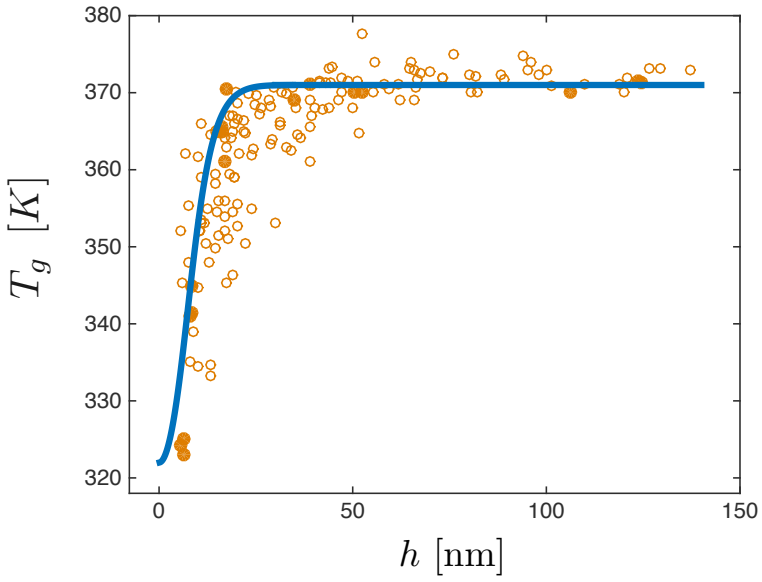

Figure 5.2 Glass transition temperature as a function of the supported film thickness for polystyrene, comparison with dilatometric experimental data for the filled symbol [88], the theory in blue line and open symbol represents other literature data [89]. The fixed parameters are the bulk glass transition temperature $T_g^{\text{bulk}} = 371$ K and the onset temperature $T_c = 463$ K, and the fitting parameters are $\lambda_v = 3.7$ nm and $T_v = 322$ K

Fig 5.2 we observe a very good agreement of the theory with the filled data point, which are considered well controlled because of the annealing condition and atmosphere [88]. The same work can be done on nano-sphere Fig 5.3, using the theoretical results for the sphere and the experimental criterium saying that at the glass transition temperature half of the volume has a liquid-like behavior. It is clear that the experimental scatter is not satisfying to conclude on our model here. However, we know that the preparation of polystyrene nano-spheres is not as well controlled as thin polymer films, for instance the presence

of surfactant which are often used in preparation technique can affect significantly the free interface properties. We now compare on the Fig. 5.4, the theoretical results of the

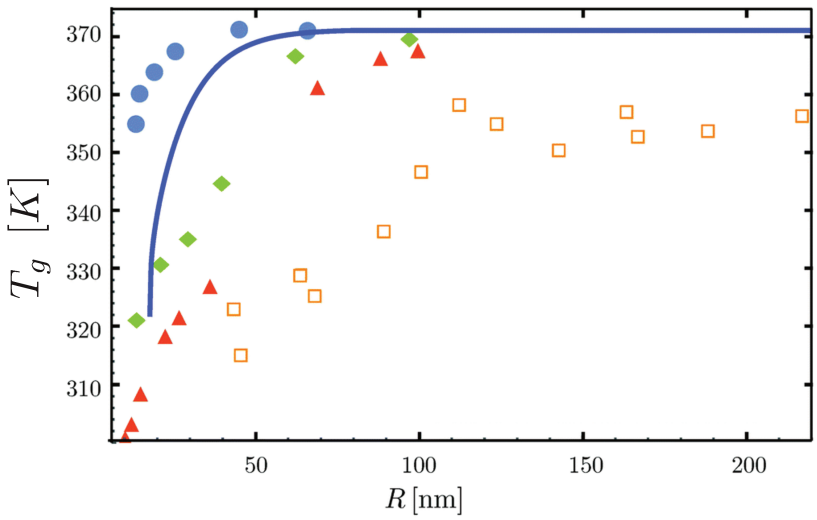

Figure 5.3 Glass transition temperature as a function of the sphere radius, in blue line the theoretical results for polystyrene using the same fitting parameter as for the supported film. The blue dots are data from this reference [75] , the green square from [74] for an anionic surfactant , the red triangle from [74] for surfactant free nanoparticles and the empty orange square from [76] .

reduction of glass transition temperature results for the studied geometries for polystyrene. The greater the exposition of the sample to the free surface, the greater the effect on the glass transition. It is clear that the nano-sphere will experience a greater effect than a supported film.

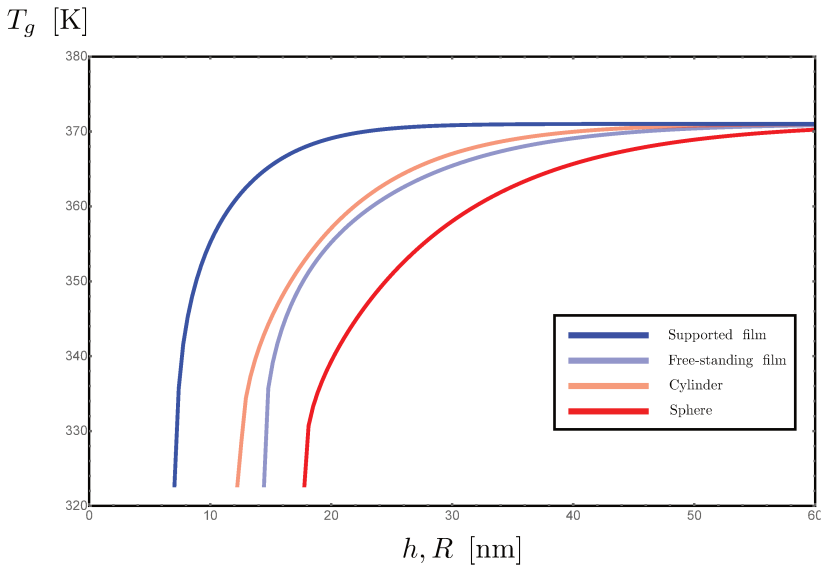

Figure 5.4 Glass transition temperature as a function of the film thickness or the sphere or cylinder radius in presence of a purely free interface.

5.3.2 Mobile layer at the free surface

From our model we can also predict the size of the mobile layer (i.e. the size of the sample that relaxes liquid-like). Therefore for finite size system we always predict a minimal

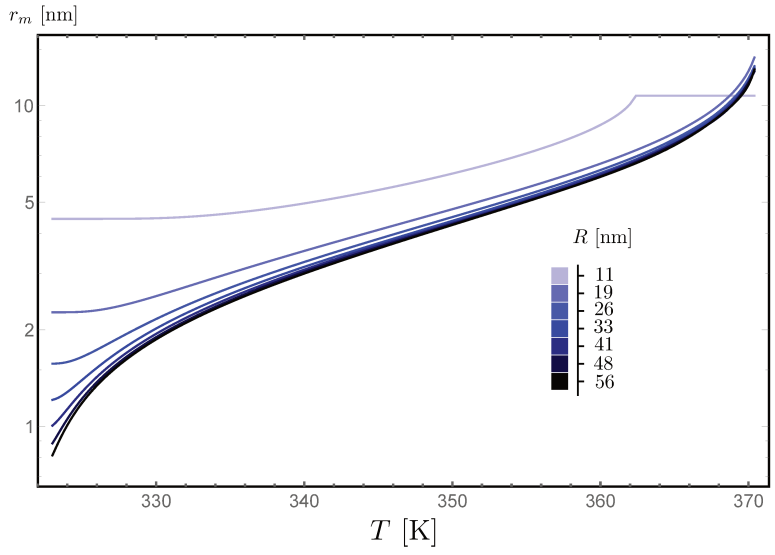

Figure 5.5 Mobile layer thickness as a function of the temperature for several cylinder radius.

size for the sample below which there are no possibility to reach a glassy state. For the sphere one can show that it corresponds to a radius of 10 nm which corresponds to the cooperative length at the bulk glass transition temperature.

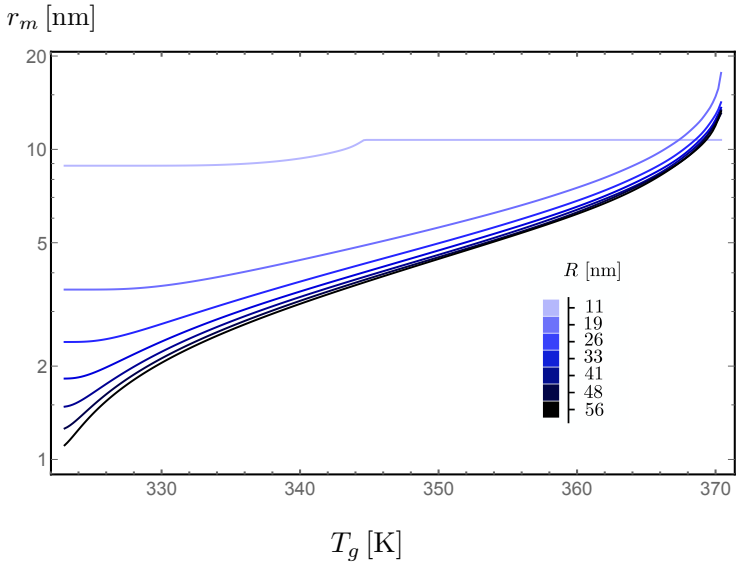

Figure 5.6 Mobile layer thickness as a function of the temperature for several sphere radius.

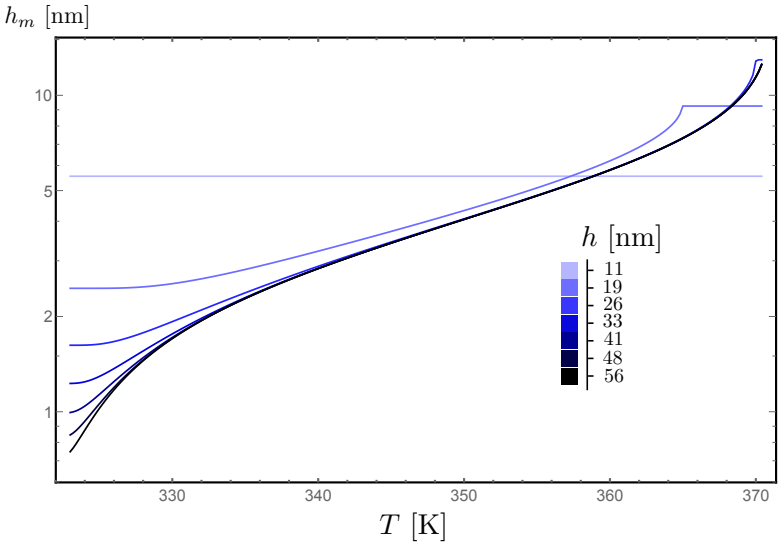

Figure 5.7 Mobile layer thickness as a function of the temperature for several film thickness.

5.4 Attractive boundary

In the previous section we have studied the effect of a free interface on cooperativeness and thus on the decrease of the glass transition temperature. However, it has been experimentally observed that certain substrates interacting with the polymers can on the contrary increase the glass transition temperature. In this section, we propose a model that could explain the rising effect of some interfaces on the glass transition temperature

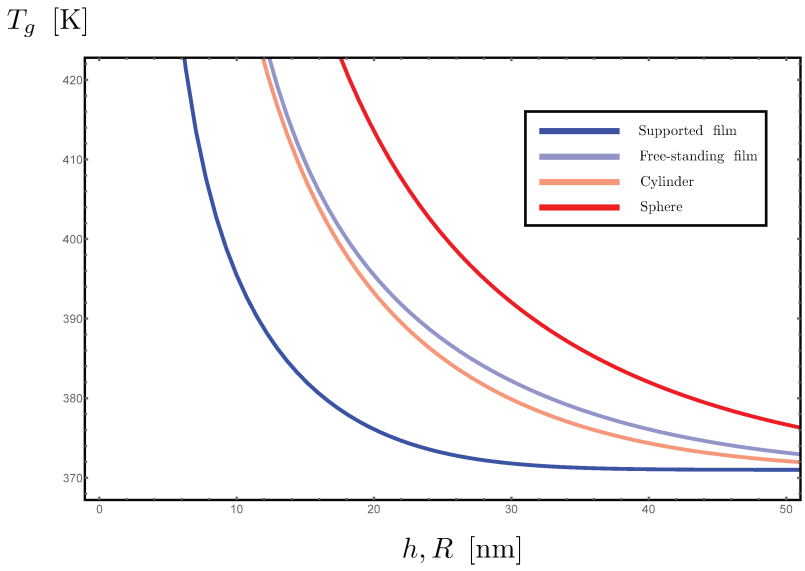

Figure 5.8 Glass transition temperature as a function of the film thickness or the sphere or cylinder radius in presence of a purely attractive interface.

and this for several possible geometries.

5.4.1 Purely attractive boundary

If one considers an attractive interface, we assume that a walk that reaches this interface with a number of steps below N^*, will not relax. Therefore if we consider a test particle, this particle can relax either bulk-like with a probability $1-p = S$ (S the survival probability) or if it touches the interface, we have to make another try, with known probability of success $p(1-p)$; succeeding to relax bulk-like at the nth trial therefore is associated with a probability $p^{n-1}(1-p)$. The effective cooperativity thus reads:

$$N^*_{\text{eff}} = \sum_{n=0}^{\infty} p^n(1-p)\left(n\langle l\rangle + N^*\right) \tag{5.28}$$

$$= N^* + \frac{1-S}{S}\langle l\rangle \ , \tag{5.29}$$

with $\langle l\rangle$ the average length of the first passage to the interface. At the glass transtion temperature we have:

$$N^*_{\text{eff}}(T_g) = N^*(T_g^{\text{bulk}}) \tag{5.30}$$

The survival probability and average first passage length have been computed for four geometries in the previous section. In Fig. 5.8 we plot our results for four geometries.

5.4.2 Partially attractive boundary

In this section we study a supported film, with an attractive boundary at the bottom and a free surface at the top. Both of the effect of this boundary can be modified through partially reflective condition at the interface, the effect of the interface will get stronger as κ_i increases (when $\kappa_i = 0$, the walks are always reflected, whereas $\kappa_i \to \infty$).

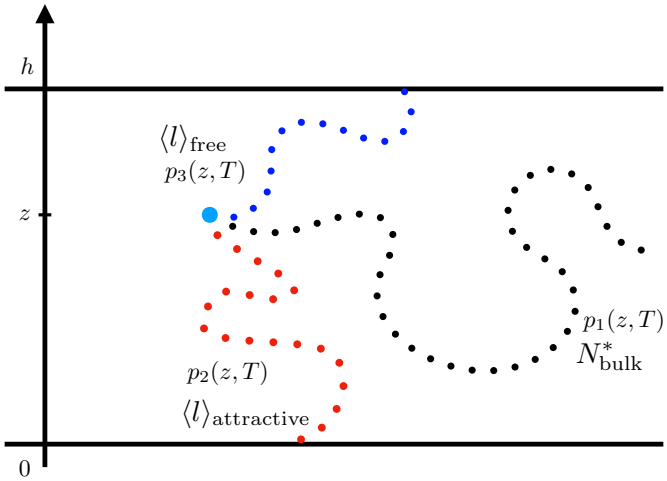

Figure 5.9 A walk of length l starting in z as a probability $p_1(z,l)$ to stay in the film, a probability $p_2(z,l)$ to reach the attractive interface, and a probability $p_3(z,l)$ to reach the free interface. Therefore at a given temperature the average length for a walk inside the film is $N^*(T)$, for a walk touching the free interface $\langle l \rangle_{free}$ and $\langle l \rangle_a$ for a walk touching the attractive interface.

The effective cooperativity in presence of these two interfaces at position z inside the film is therefore:

$$N^*_{\text{eff}}(T,\kappa_1,\kappa_2,h,z) = \sum_{n=0}^{\infty} p_2^n \left(p_3\left(n\langle l\rangle_{\text{a}} + \langle l\rangle_{\text{free}}\right) + p_1\left(n\langle l\rangle_{\text{a}} + N^*\right)\right) \tag{5.31}$$

$$= \frac{1}{1-p_2}\left[p_1 N^* + p_2\langle l\rangle_{\text{a}} + p_3\langle l\rangle_{\text{free}}\right] \tag{5.32}$$

In order to compute all these statistics, we need the probability density of a walk of length l, starting in z and ending in z' without being absorbed by any interface. This density verifies the diffusion equation with the following boundary conditions as depicted

in Fig. 5.10:

$$\partial_l P = \frac{1}{2}\Delta P \ , \tag{5.33}$$

$$\partial_z P(z,z',l)|_{z=h} = -\kappa_2 P(h,z',l) \ , \tag{5.34}$$

$$\partial_z P(z,z',l)|_{z=0} = \kappa_1 P(0,z',l) \ , \tag{5.35}$$

$$P(z,z',0) = \delta(z-z') \ . \tag{5.36}$$

Therefore the eigenfunction reads:

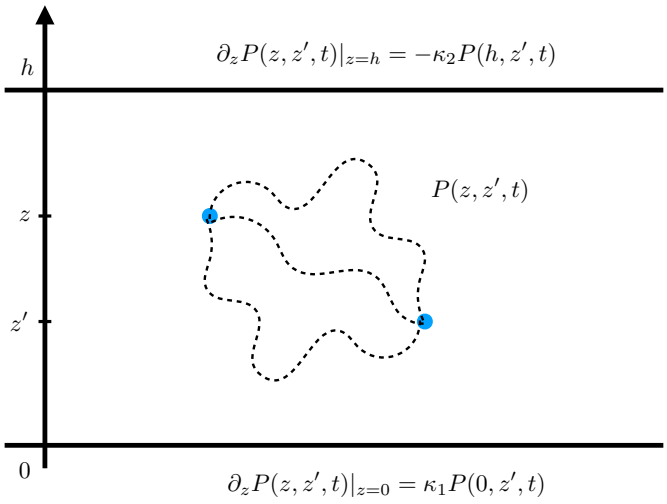

Figure 5.10 At the interfaces, we can tune the effect of the free interface or the attractive interface by modyfing κ_i, when $\kappa_i = 0$, the walks are always reflected, whereas $\kappa_i \to \infty$ all the walks are truncated at the interface. This boundary condition are known in heat transfer as radiative boundary conditions [90].

$$\phi_n(z) = a_n \left(\cos\left(\beta_n \frac{z}{h}\right) + \frac{\kappa_1}{\beta_n} \sin\left(\beta_n \frac{z}{h}\right) \right) \ , \tag{5.37}$$

a_n is determined by the normalisation of the eigenfunction, it yields:

$$a_n = \left[\left(\beta_n^2 + h^2\kappa_1^2\right) \left(1 + \frac{\kappa_2 h}{\beta_n^2 + h^2\kappa_2^2}\right) + h\kappa_1 \right]^{-1/2} \tag{5.38}$$

this eigenfunction is associated with the eigenvalue β_n that verifies:

$$\tan(\beta_n) = \frac{\beta_n + h(\kappa_1 + \kappa_2)}{\beta_n^2 - \kappa_1\kappa_2 h^2} \ . \tag{5.39}$$

Enventually one gets the density $P(z, z', l)$:

$$P(z, z', l) = \frac{2}{h} \sum_{n=0}^{\infty} \phi_n(z)\phi_n(z') e^{-\frac{\beta_n^2}{2h^2} l} \ , \tag{5.40}$$

from which we can compute p_1 , p_2 , p_3 and $\langle l \rangle_a$, $\langle l \rangle_{\text{free}}$. First we compute p_1 which is simply the survival probability at a given temperature inside the film:

$$p_1(z, T) = \int_0^h \mathrm{d}z' \ P\left(z, z', N^*(T)\right) \ . \tag{5.41}$$

We compute the probability of being absorbed at the bottom boundary $p_2(z, T)$, this probability is simply the flux of walks at this boundary $p_2(z, T) = \frac{1}{2}\partial_z P(z, z', N^*(T))|_{z'=0}$, therefore this probability reads:

$$p_2(z, T) = \frac{\kappa_1}{h} \sum_{n=0}^{\infty} \phi_n(z)\phi_n(0) e^{-\frac{\beta_n^2}{2h^2} N^*(T)} \ , \tag{5.42}$$

the length distribution of the first passage is simply $p_2(z, T)$, therefore the average length of the truncated walks smaller than the bulk walk reads (the average length varies with z the position in the film where we look at this average length):

$$\langle l \rangle_a = \frac{\kappa_1 N^*}{h} \sum_{n=0}^{\infty} \phi_n(z)\phi_n(0) \left(2h^2 - e^{-\frac{\beta_n^2}{2h^2} N^*(T)}\right) \left(\frac{4h^4}{\beta_n^4} + \frac{2h^2 N^*(T)}{\beta_n^2}\right) \tag{5.43}$$

With the flux of walks at the upper interface we get:

$$p_2(z, T) = \frac{\kappa_2}{h} \sum_{n=0}^{\infty} \phi_n(z)\phi_n(h) e^{-\frac{\beta_n^2}{2h^2} N^*(T)} \ , \tag{5.44}$$

and

$$\langle l \rangle_{\text{free}} = \frac{\kappa_2 N^*}{h} \sum_{n=0}^{\infty} \phi_n(z)\phi_n(h) \left(2h^2 - e^{-\frac{\beta_n^2}{2h^2} N^*(T)}\right) \left(\frac{4h^4}{\beta_n^4} + \frac{2h^2 N^*(T)}{\beta_n^2}\right) \ . \tag{5.45}$$

We now have an analytical expression of the effective cooperativity Eq. (5.32) using Eq. (5.45) and Eq. (5.44). This local cooperativity depends on the property of each interface. The eigenvalue that verifies Eq. (5.39) are computed using a third order Newton method [90, 91]. We also predict with this model the mobile layer as a function of the temperature for different film thickness and interfaces. We observe that the presence of attractive boundaries creates jumps in the graphs of the mobile layer as a function of the temperature.

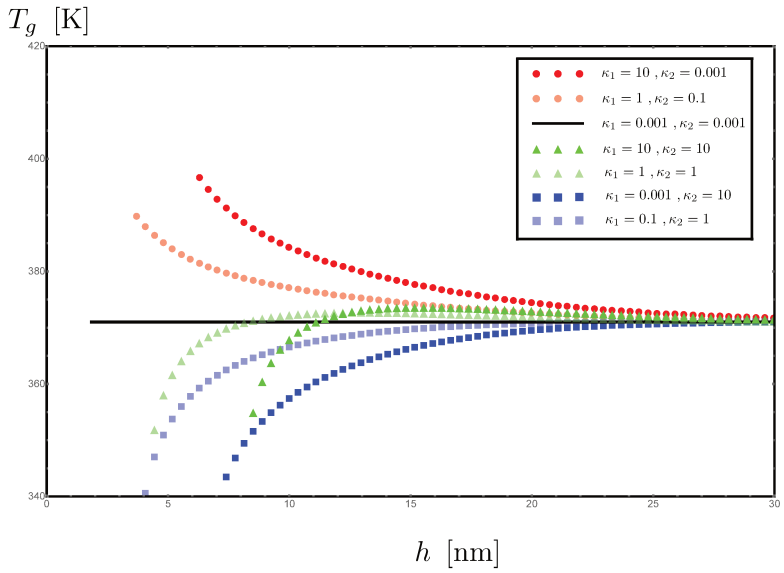

Figure 5.11 Glass transition temperature for a supported thin film as a function of the film thickness. By modifying κ_i we predict several behavior, the κ_i are dimensionless and there values are chosen to exhibit different behavior. In red dot the attractive interface is stronger than the free interface, in green triangle both interfaces have the same strength and in blue square the free interface has a stronger effect. We observe increases of the glass transition temperature for strongly attractive interface and reduction of T_g for strongly free surface as expected. We also observe an intermediate curve with an increase of the glass transition temperature then a decrease when we reduce the size of the film, it corresponds to equivalent strength of both interfaces.

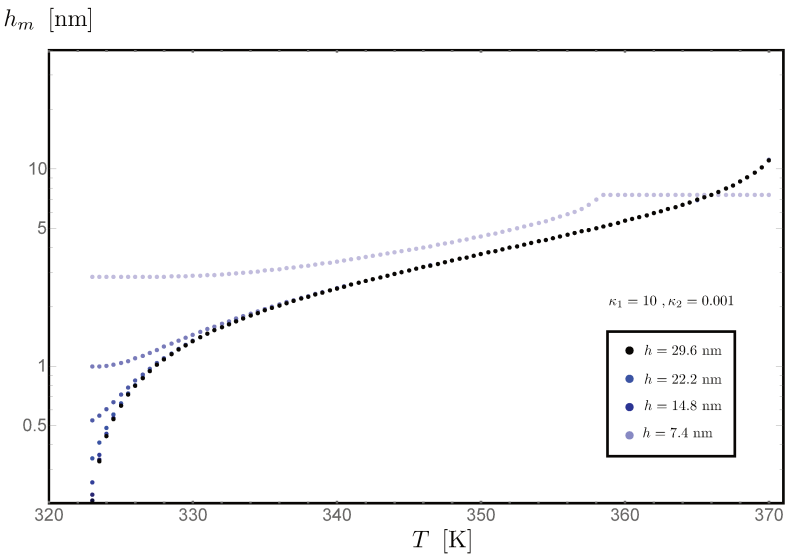

Figure 5.12 Mobile layer as a function of the temperature for several film thickness, the supported film as a free surface at the top and an inert substrate at the bottom.

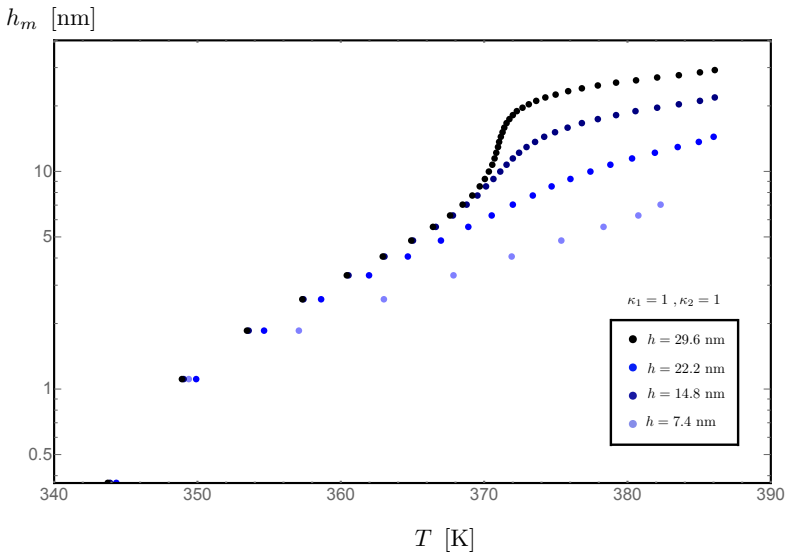

Figure 5.13 Mobile layer as a function of the temperature for several film thickness, the supported film as a free surface at the top and an attractive substrate at the bottom.

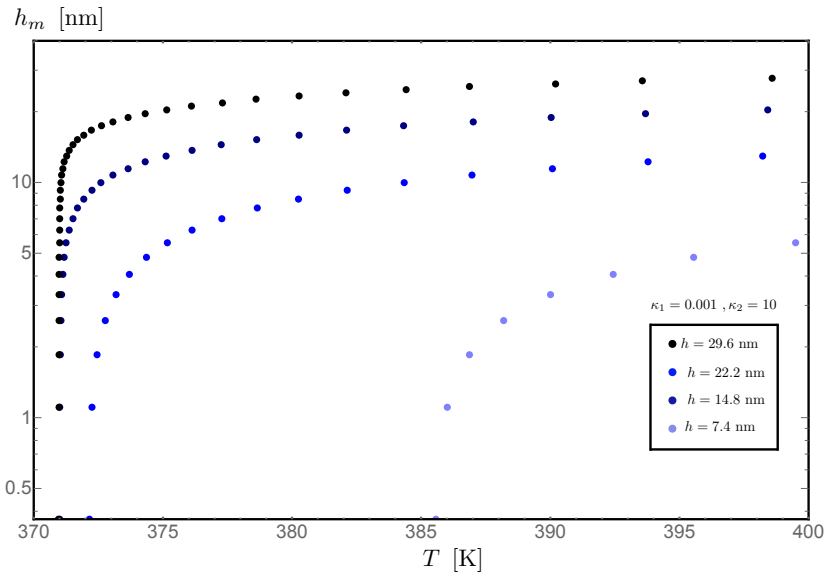

Figure 5.14 Mobile layer as a function of the temperature for several film thickness, the supported film as an inert substrate at the top and an attractive substrate at the bottom.

5.5 Conclusion

In this chapter we have investigated the effect of confinement for both free interfaces and attractive interfaces, the geometry has no big influence, it is rather the ratio of volume to free surface that drives the enhanced dynamic. We have modelled the enhanced

dynamic due to the presence of a free surface by truncating the cooperative strings and also modelled a slower dynamic due to attractive interfaces by a process of additive cooperative strings in order to find a relaxation path and predict non monotonic decrease or increase of the glass transition temperature tuning the free interface and the attractive interface in terme of reflectivity for the cooperative strings.

Chapter 6

Polymeric effect on the glass transition

Chapter 6 : Polymeric effect on the glass transition

↑ back to contents

Chapter abstract

The motivation of this chapter is the anomalous glass transition temperature in thin polymer films of polystyrene at high molecular weight and theoretical approaches to explain this phenomenology[92, 93, 94]. We provide statistics of particular paths inside the polymer configuration in confinement. These paths are called bridge, loop or link (see Fig.6.1). We compute the length probability density of these structures in the gaussian chain model framework. The molecular weight dependency of these statistics is closely studied.

6.1 Introduction

Synthesized by chemical –polystyrene– or biological –DNA– means, polymers are ubiquitous and, in science, at the frontier of physics, chemistry, biology and mathematics. A

polymer is the repetition of a monomer unit. Sir Edwards[95] pointed out the analogy between the path of a quantum particle and the configuration of a polymer chain. This description has been successful and prolific from a microscopic (chain configuration, reptation time) to macroscopic scale (stress relaxation of a complex fluid). Usually, theoretical problems in polymer physics have been considered via the analysis of the chain configuration statistics[96, 97]. Polymer chains are successfully described by random walks or

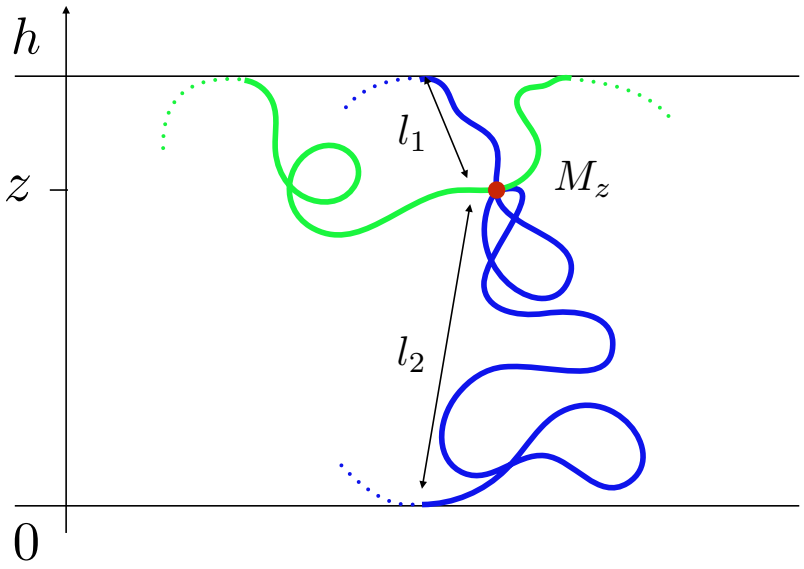

Figure 6.1 The monomer at the position M_z in red belongs to a polymer chain. We are interested in the probability of the monomer to be part a bridge in blue or a loop in green and the dependence of the probability density with the length of the bridge or the loop. A link is a bridge or a loop indifferently.

brownian motion in the gaussian chain model[98]. Within this framework our aim is to compute the length probability density of bridge, loop and link inside a film of thickness h and for a polymer of molecular weight L (Fig.6.1). This work is motivated by previous studies on the delayed glass transition temperature in thin polymer films and its dependency on molecular weight[99, 94, 93]. In previous works, the length probability distribution of link has been established for infinite molecular weight[92, 94]. In our study we distinguish loops and bridges. We give in the following the exact dependency between the length density of bridge, loop, and link and the molecular weight. We believe that these results might be important towards the understanding of phenomena in confined polymer physics such as the glass transition temperature dependency on molecular weight in a confined geometry[99].

6.2 Glass transition temperature in polymer thin film

Anomalous behavior of the glass transition temperature T_g is observed in thin polymer films. For a free standing film, a significant drop in the glass transition occurs around a

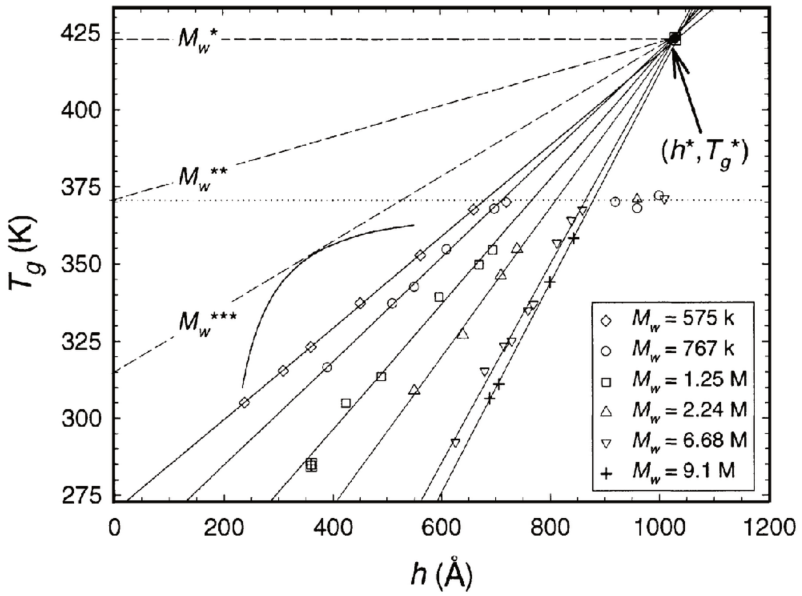

Figure 6.2 Plot of the glass transition temperature as a function of the film thickness and for high molecular weight from[99]. All the curve seems to intersect in a unique point (h^*, T^*).

thickness of 40 nm.[100] These observations suggest that the free surface region enhances glassy dynamics[77]. This hypothesis has been widely studied from a theoretical point of view.[101, 102, 103, 104, 105, 106, 94, 86, 107, 87, 108, 109, 59] An other set of experiments, with free standing polystyrene films, shows that below $M_w \sim 378\times10^3$, T_g does not exhibit dependency on M_w, but that above this limit it shows a strong dependency on the T_g curves with molecular weight M_w. At high M_w, when the thickness is below a certain value $h_0(M_w)$, T_g increases linearly with h:

$$T_g = T_g^{\text{bulk}} - f\,(M_w)\,(h_0 - h)\ , \tag{6.1}$$

both f and h_0 increase with M_w, and for $h \geq h_0$, $T_g = T_g^{\text{bulk}}$.[92, 99] The behavior of the glass transition temperature at low molecular weight has been successfully explained by the cooperative string model in confinement in the previous chapter.[59, 60] However there is a dramatic change in behavior from low to high molecular weight. Indeed, at low molecular weight, the T_g reduction curve is smooth whereas at high molecular weight the transition point is sharp. Therefore it suggests that two modes of melting are competing.[92] We have to highlight that the glass transition temperature depends on the molecular weight only for free standing films. This observation suggests that bridges–which only exist in free standing films–might play a particular role.

6.2.1 Kink diffusion model

A general model of diffusion from one end to the other along a bridge or a loop have been proposed by Lipson and Milner[93]. The local diffusivity varies along each monomer with a value τ_i for the relaxation time with a certain distribution $p(\tau_i)$. They showed that the

distribution of the total relaxation time reads (see [93]):

$$P(\tau) = \int \mathrm{d}\tau_1 ... \mathrm{d}\tau_l p(\tau_1) ... p(\tau_l) \delta(l \sum_{i=1}^{l} \tau_i - \tau) \tag{6.2}$$

If we call $\tau_g \sim 100$ s the experimental time at which we consider to be at the glass transition temperature. The probability that a loop or a bridge of length l is fast (i.e. its typical relaxation time is smaller than τ_g) is therefore:

$$F(l) = \int_0^{\tau_g} \mathrm{d}\tau P(\tau) \tag{6.3}$$

The distribution of local relaxation time drives all these quantities, but for local relaxation time with finite first and second moment, one can show that at large l, the probability of being on a fast loop is approximated by the Heaviside function:

$$F(l) \sim \Theta(l_g(T) - l) \tag{6.4}$$

If we assume that the local relaxation time follows the Vogel-Fulcher-Tamman phenomenology [69, 70, 71], the characteristic fast loop length reads:

$$l_g(T) = \sqrt{\frac{\tau_g}{\tau_0}} \exp\left(-\frac{A}{2(T - T_\mathrm{v})}\right) \tag{6.5}$$

with τ_0 a typical molecular time scale, T_v the Vogel temperature, $A = (T_\mathrm{c} - T_\mathrm{v}) \ln(\tau_\mathrm{c}/\tau_0)$. τ_c being a liquid-like relaxation time and T_c the temperature at the cooperative onset[59].

6.2.2 Sliding motion

De Gennes proposed a simpler kink diffusion model[92], where the relaxation time τ is essentially the average time required for a kink to go through the polymer chain via the bridges or loops that connect the free interfaces. During this motion, the kink goes through l monomers. And this requires successive free volumes $(\omega_i)_l$ that are identically distributed with a gaussian distribution:

$$p(\omega) = \sqrt{\frac{\pi}{2\omega_0^2}} e^{-\frac{\omega^2}{2\omega_0^2}} \tag{6.6}$$

The width ω_0 is small ($\omega_0/a^3 = \eta << 1$) in comparison with the monomer size. The relaxation time of this sequential motion reads:

$$\tau = \tau_0 \langle \exp\left(\frac{1}{v(T)} \sum_i \omega_i\right) \rangle \tag{6.7}$$

with tau_0 a molecular timescale, after integration one gets:

$$\tau = \tau_0 \exp\left(\frac{l\eta^2}{2\epsilon(T)^2}\right) \tag{6.8}$$

with $\epsilon(T) = \alpha(T - T_v)$. l is the size of the trajectory involved in the relaxation process. In this model, bridges and loops are contributing equally to the relaxation process. In De Gennes article, it is assumed that $l \sim h^2$ which is true in very confined regime, and therefore one can recover the linear dependence between the glass transition temperature and the size of the polymer film using Eq.6.8. However there is no more molecular weight dependency on this scaling. The aim of our work is precisely to provide the density of l and its exact dependency on the molecular weight.

6.3 Bridge and loops statistics

6.3.1 Gaussian chain

A polymer chain is the repetition of a sequence of monomers, therefore the positions of the monomers can be computed with a random walk on a lattice. The molecular weight is given by the number of monomers N_w inside a polymer chain, the distance between the vertex of the lattice a is the size of a monomer. Therefore, the length of the polymer chain is $L = N_w a$ (in the continuous description used in the following, the length are dimensionless, therefore L and the number of monomers are the same quantity). We know that at large N_w, the polymer chain conformation will be described by a gaussian distribution[97]. At large N_w, or high molecular weight, one can switch to a continuous description using Brownian motion. In the continuous limit we assume that $a \to 0$ and $N_w \to \infty$ with $L = N_w a$ finite [58]. In that limit, the length probability distributions of bridges, loops or links are successfully described by the paths of the brownian motion.

End-to-end distance

We define the end-to-end distance of an ideal polymer chain by:

$$\boldsymbol{R} = \sum_{i=1}^{N_w} \boldsymbol{a}_i \tag{6.9}$$

since the trajectory corresponds to a random walk $\langle \boldsymbol{a}_i \rangle = \boldsymbol{0}$ and $\langle \boldsymbol{R} \rangle = \boldsymbol{0}$ the mean value of the end-to-end distance is zero. However the mean square value reads:

$$\langle \boldsymbol{R}^2 \rangle = \sum_{i,j=1}^{N_w} \langle \boldsymbol{a}_i \boldsymbol{a}_j \rangle = N_w a^2 \ , \tag{6.10}$$

therefore the size of the polymer coil is $R_0 = a\sqrt{N_w}$. The probability $P(\boldsymbol{R})$ that a chain starts in 0 and ends in $\boldsymbol{R}$ is given by:

$$P(\boldsymbol{R}) = \frac{A_{Nw}(\boldsymbol{R})}{(2d)_w^N} \ , \tag{6.11}$$

where $A_{Nw}(\boldsymbol{R})$ corresponds to the number of paths starting in 0 and ending in $\boldsymbol{R}$, and $(2d)_w^N$ the total number of paths in dimension d. Since $\boldsymbol{R}$ is the sum of a large number of independent random variables, one can use the central limit theorem, and we find a gaussian probability for the end-to-end distribution:

$$P(\boldsymbol{R}) = (\frac{3}{2\pi N_w a^2})^{3/2} \exp\left(-\frac{3\boldsymbol{R}^2}{2Na^2}\right) \quad . \tag{6.12}$$

This is a well known property of random walks. In fact a chain is not gaussian because we should take into account short range interactions between segments which are close to each other in the coil, this is called the excluded volume effect. One can model the polymer by a path on a lattice with the condition that a path cannot go twice on a same node of the lattice. This kind of random walks are called self avoiding random walks.

6.3.2 Definition

A bridge is a segment of a polymer that connects the two free interfaces of a thin film, a loop connects the same interface of a thin film and a link is indifferently a bridge or a loop (see Fig.6.1). Our aim is to provide at a certain position z inside the film, the length probability density of bridge, loop and link.
At a distance z from the lower interface, we pick a monomer M_z that belongs to a polymer chain, therefore from that point M_z, one can observe two branches of the polymer chain, these two branches are described by two brownian motions. This polymer chain has a finite length L, thus the monomer is at a distance P from one end of the polymer chain and $L - P$ from the other. With P distributed uniformly $P \sim \mathcal{U}([0, L])$. Therefore the length l_1 of the first branch has to be smaller than $L - P$ and the length l_2 has to be smaller than P (see Fig.6.3). We set $\mathcal{L}_b(z, l)$ to be the length probability density of bridge at a distance z from the lower interface.

$$\mathcal{L}_b(z, l) = \int_0^L \frac{\mathrm{d}P}{L} \mathcal{L}_{b,l}(P, z, l) \ , \tag{6.13}$$

with $\mathcal{L}_b(P, z, l)$ the probability density of bridge of length l at a distance z from the interface and P the position of the monomer fixed inside the polymer chain. The density for a bridge starting at the interface i_1 and ending at the interface i_2 reads:

$$\mathcal{L}_b(P, z, l) = \int_0^P \mathrm{d}l_1 \int_0^{L-P} \mathrm{d}l_2 \delta(l_1 + l_2 - l) f_{i_1}(z, l_1) f_{i_2}(z, l_2) \ , \tag{6.14}$$

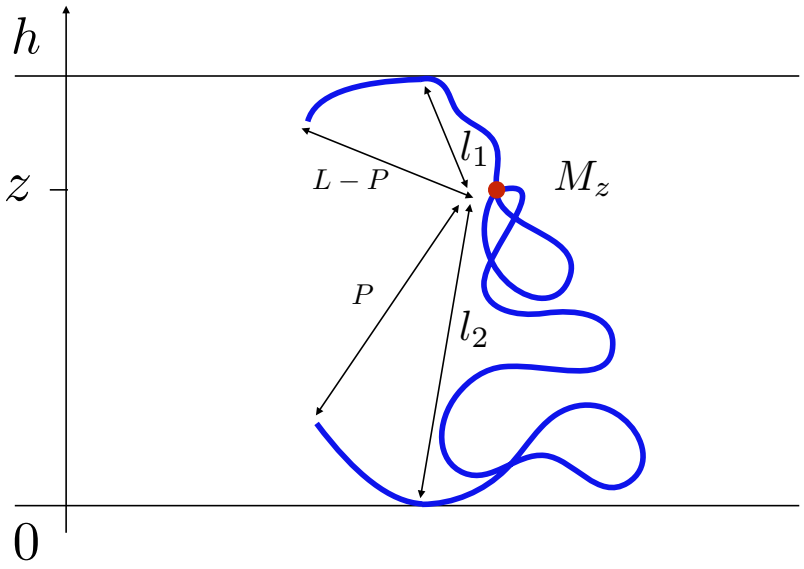

Figure 6.3 The position P of the monomer M_z follows a uniform distribution. The length of the first branch $l_1 < L - P$ and the length of the other one $l_2 < P$.

with f_{i_1} the probability density of first passage at the interface i_1 after a trajectory of length l, starting at a distance z from the lower interface. After integration, one gets:

$$\mathcal{L}_b(P, z, l) = \int_{\max(0,l-P)}^{\min(l,L-P)} \mathrm{d}l_2 f_{i_1}(z, l_2) f_{i_2}(z, l - l_2) \ . \tag{6.15}$$

The length probability density of loop or link are set to be respectively $\mathcal{L}_l(P, z, l)$ and $\mathcal{L}_{b\&l}(P, z, l)$. The link probability density depends on the first passage density in $z = 0$ or $z = l$ indifferently, noted $f(z, l)$.

6.3.3 First passage densities

The density of trajectories of length l, starting in z and reaching an interface at $z = 0$, or at $z = h$ or at $z = 0$ or $z = h$ indifferently, for the first time are called first passage densities[110, 111, 112]. These random processes are well known and have been studied extensively[112]. The first passage densities are computed directly from the density of paths of length l going from z to z_1 without touching the interfaces. This density is noted $P_c(z_1, l|z, 0)$ and verifies the diffusion equation with absorbing boundary conditions in $z = 0$ and $z = h$:

$$\partial_t P_c = D\Delta P_c \ , \tag{6.16}$$

$$P_c(z = 0) = 0 \ , \tag{6.17}$$

$$P_c(z = h) = 0 \ . \tag{6.18}$$

The diffusion coefficient depends on the dimension of the space, therefore without loss of generality we set $D = \frac{1}{2d}$, with d the dimension of the space (here $d = 3$). The solution of this partial differential equation is:

$$P_c\left(z_1, l|z, 0\right) = \frac{2}{h}\sum_{n=1}^{+\infty} \sin\left(\lambda_n z\right) \sin\left(\lambda_n z_1\right) \exp\left(-D\lambda_n^2 l\right) \ , \tag{6.19}$$

with $\lambda_n = \frac{\pi n}{h}$. The density of paths of length l reaching the interface $z = 0$ for the first time, is the density of paths of length l reaching the interface $z = 0$ in the small volume $\mathrm{d}\tau$ just below the interface, therefore if $\mathrm{d}\tau \to 0$:

$$f_0(z, l) = D\left(P_c\left(0, l|z, 0\right) - P_c\left(0 + \mathrm{d}\tau, l|z, 0\right)\right) \frac{1}{\mathrm{d}\tau} \ , \tag{6.20}$$

$$f_0(z, l) = \frac{1}{6} \frac{\mathrm{d}P_c\left(u, l|z, 0\right)}{\mathrm{d}u}|_{u=0} \ , \tag{6.21}$$

eventually one gets:

$$f_0(z, l) = \frac{1}{3h}\sum_{n=1}^{+\infty} \lambda_n \sin\left(\lambda_n z\right) \exp\left(-\frac{\lambda_n^2}{6} l\right) \ , \tag{6.22}$$

similarly the first passage density in $z = h$ reads:

$$f_h(z, l) = \frac{1}{3h}\sum_{n=1}^{+\infty} (-1)^n \lambda_n \sin\left(\lambda_n z\right) \exp\left(-\frac{\lambda_n^2}{6} l\right) \ . \tag{6.23}$$

The first passage density to $z = 0$ or $z = h$, also called the first exit time from the interval $[0, h]$, $f(z, l)$ is linked to the survival probability $S(z, l)$. Indeed the probability that a path of length l has already reached either $z = 0$ or $z = h$ is given by $1 - S(z, l)$ and consequently its density reads:

$$f(z, l) = -\frac{\mathrm{d}S}{\mathrm{d}l}(z, l) \ . \tag{6.24}$$

The survival probability is the integral of the density $P_c(z_1, l|z, 0)$ over all the ending points z_1 inside the film:

$$S(z, l) = \int_0^h \mathrm{d}z_1 P_c(z_1, l|z, 0) \ , \tag{6.25}$$

after integration one gets the survival probability in a film of thickness h:

$$S(z, l) = \frac{4}{h}\sum_{n>0, n \text{ odd}} \frac{\sin\left(\lambda_n z\right)}{\lambda_n} \exp\left(-\frac{\lambda_n^2}{6} l\right) \ . \tag{6.26}$$

The first exit time density from the film of thickness h is therefore:

$$f(z,l) = \frac{2}{3h} \sum_{n>0, n \text{ odd}} \lambda_n \sin(\lambda_n z) \exp\left(-\frac{\lambda_n^2}{6} l\right) . \tag{6.27}$$

Note that $f(z,l) = f_0(z,l) + f_h(z,l)$.

6.3.4 Bridge, loop and link distribution

Using the Eqs.[6.15,6.22,6.23], it is straightforward to get the probability density of bridge, loop or link as a function of the length of the path l and the position inside the film z.

Loop

Consider a loop that connects the same interface in $z = 0$, therefore the density reads:

$$\mathcal{L}_l(z,l) = \frac{1}{9h^2} \frac{l(L-l)}{L} \sum_{n=1}^{+\infty} \lambda_n^2 \sin^2(\lambda_n z) \exp\left(-\frac{\lambda_n^2}{6} l\right) \tag{6.28}$$

$$+ \frac{2}{9h^2} \frac{(L-l)}{L} \sum_{n>m} \frac{\lambda_n \lambda_m}{a_{n,m}} \sin(\lambda_n z) \sin(\lambda_m z) \left(1 - \exp(-a_{n,m} l)\right) , \tag{6.29}$$

with $a_{n,m} = \frac{\lambda_n^2 - \lambda_m^2}{6}$. The loop density that connects the interface in $z = h$ is obtained doing the transformation $z \to h - z$.

Bridge

A bridge is a path that connects the two opposite interfaces. The Eq.6.13 is multiplied by 2, since the path can indifferently go from $z = 0$ to $z = h$ or $z = h$ to $z = 0$ and consequently the density reads:

$$\mathcal{L}_b(z,l) = \frac{2}{9h^2} \frac{l(L-l)}{L} \sum_{n=1}^{+\infty} (-1)^n \lambda_n^2 \sin^2(\lambda_n z) \exp\left(-\frac{\lambda_n^2}{6} l\right) \tag{6.30}$$

$$+ \frac{4}{9h^2} \frac{(L-l)}{L} \sum_{n>m} (-1)^n \frac{\lambda_n \lambda_m}{a_{n,m}} \sin(\lambda_n z) \sin(\lambda_m z) \left(1 - \exp(-a_{n,m} l)\right) . \tag{6.31}$$

Link

Eventually consider a link, which is indifferently a bridge or a loop, its length probability density reads:

$$\mathcal{L}_{b\&l}(z,l) = \frac{4}{9h^2}\frac{l(L-l)}{L}\sum_{n>0,n\text{odd}} \lambda_n^2 \sin^2(\lambda_n z)\exp\left(-\frac{\lambda_n^2}{6}l\right) \tag{6.32}$$

$$+\frac{8}{9h^2}\frac{(L-l)}{L}\sum_{n>m,\text{odd}} \frac{\lambda_n\lambda_m}{a_{n,m}}\sin(\lambda_n z)\sin(\lambda_m z)\left(1-\exp\left(-a_{n,m}l\right)\right) \ . \tag{6.33}$$

In this section we have given the length probability density for a monomer to belong to a link (or loop, or bridge), with the exact dependency on the molecular weight and on the position of the monomer z inside the film. These densities can be used to compute all kind of statistics involving link, bridge or loop paths.

6.4 Discussion

6.4.1 Links density inside the film

By integrating the densities over the film thickness and over its length one can compute the total density of bridges, loops or links inside the polymer film. The density of links of length l inside a film of thickness h reads:

$$\Phi_{b\&l}(l) = \int_0^h \frac{\mathrm{d}z}{h}\mathcal{L}_{b\&l}(z,l) \ , \tag{6.34}$$

after integration one gets:

$$\Phi_{b\&l}(l) = \frac{4}{d^2h^2}\frac{l(L-l)}{L}\sum_{n>0,n\text{ odd}}\frac{\lambda_n^2}{2}\exp\left(-\frac{\lambda_n^2}{2d}l\right) \ . \tag{6.35}$$

Therefore the percentage of links inside a film reads:

$$\phi_{b\&l}(h,L) = \int_0^L \mathrm{d}l\Phi_{b\&l}(l) \ , \tag{6.36}$$

and the average length of a link is:

$$\langle l\rangle_{b\&l}(h,L) = \int_0^L \mathrm{d}l\frac{l\Phi_{b\&l}(l)}{\phi_{b\&l}(h,L)} \tag{6.37}$$

Similarly one can get these quantities for bridge and loop. We can notice that a self similar variable appears: $\tilde{L} = \frac{\pi^2 L}{2dh^2}$. Using this variable and setting $u = \frac{l}{L}$, the density

reads (with d=3):

$$\Phi_{b\&l}(l)\mathrm{d}l = \frac{8}{\pi^2}\tilde{L}^2 \sum_{n>0,n\mathrm{odd}} n^2 e^{-n^2\tilde{L}u} u(1-u)\mathrm{d}u \tag{6.38}$$

After integration the density of link reads in term of the self similar variable:

$$\phi_{b\&l}(\tilde{L}) = 1 - \frac{\pi^2}{6\tilde{L}} + \frac{8}{\pi^2}\sum_{n>0,n\mathrm{odd}} \frac{e^{-\tilde{L}n^2}}{n^2}\left(1+\frac{2}{\tilde{L}n^2}\right) , \tag{6.39}$$

for the bridges it reads:

$$\phi_b(\tilde{L}) = \frac{1}{3} - \frac{7\pi^2}{90\tilde{L}} + \frac{4}{\pi^2}\sum_{n>0}(-1)^{n+1}\frac{e^{-\tilde{L}n^2}}{n^2}\left(1+\frac{2}{\tilde{L}n^2}\right) , \tag{6.40}$$

and to obtain the loop density, we have to multiply by 2 the Eq.6.29, to take into account also the loops of the other interface:

$$\phi_l(\tilde{L}) = \frac{2}{3} - \frac{4\pi^2}{45\tilde{L}} + \frac{4}{\pi^2}\sum_{n>0}\frac{e^{-\tilde{L}n^2}}{n^2}\left(1+\frac{2}{\tilde{L}n^2}\right) . \tag{6.41}$$

One can easily check that $\phi_{b\&l}(\tilde{L}) = \phi_b(\tilde{L}) + \phi_l(\tilde{L})$. We observe that in a very confined regime ($\tilde{L} \to +\infty$), there is a partition of the paths between bridge and loop. 1/3 of bridges and 2/3 of loops, all the monomers belong to links with probability 1 in this regime.

6.4.2 Links average length

The link length is normalized by L the molecular weight. After integration the link average length reads:

$$\langle\frac{l}{L}\rangle_{b\&l} = \frac{1}{\phi_{b\&l}(\tilde{L})}\left(\frac{\pi^2}{6\tilde{L}} - \frac{\pi^4}{20\tilde{L}^2} + \frac{8}{\pi^2}\sum_{n>0,n\ \mathrm{odd}} b_n\right) , \tag{6.42}$$

with $b_n = \frac{e^{-\tilde{L}n^2}}{n^2}\left(1+\frac{4}{\tilde{L}n^2}+\frac{6}{\tilde{L}^2n^4}\right)$. Similarly one can gets the bridge average length:

$$\langle\frac{l}{L}\rangle_b = \frac{1}{\phi_b(\tilde{L})}\left(\frac{7\pi^2}{90\tilde{L}} - \frac{31\pi^4}{1260\tilde{L}^2} + \frac{4}{\pi^2}\sum_{n>0}(-1)^{n+1}b_n\right) , \tag{6.43}$$

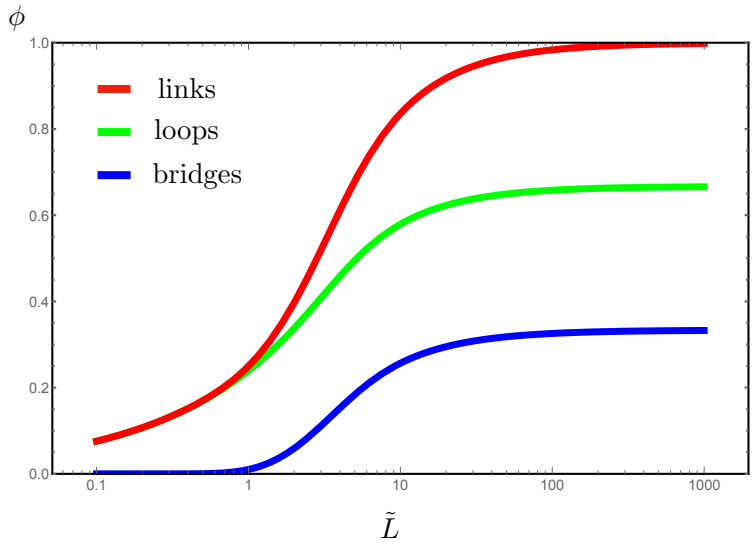

Figure 6.4 The density of bridges (blue), loops (green) or links (red) as a function of the auto-similar variable $\tilde{L}$. We observe that at high molecular weight and/or small film (i.e. $\tilde{L} \to \infty$) all the monomers are part of links, with a partition 1/3 in the bridge and 2/3 in the loops. We also notice that the proportion of loops inside a film decreases much slowly in a large film (or at small molecular weight) than the proportion of bridge, indeed in a large film, bridge are very unlikely, however close to the interface even in a large film there will be numerous loops.

and the loop average length:

$$\langle \frac{l}{L} \rangle_l = \frac{1}{\phi_l(\tilde{L})} \left(\frac{4\pi^2}{45\tilde{L}} - \frac{8\pi^4}{315\tilde{L}^2} + \frac{4}{\pi^2} \sum_{n>0} b_n \right) \quad . \tag{6.44}$$

The typical length of a link, a bridge or a loop in confinement is $\langle l \rangle \propto h^2$. It is independent of the molecular weight. The effects of molecular weight are less and less important as the system is confined ($h \to 0$ and/or $L \to \infty$). In confinement it is striking that the average bridge length is almost twice as big than the average loop length (see Fig.6.7).

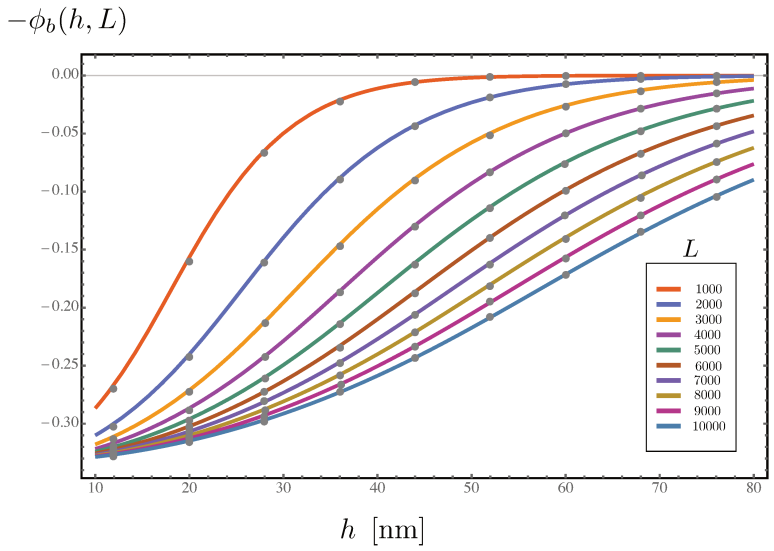

Figure 6.5 The opposite of the density of monomers belonging to a bridge for several molecular weight, the spectrum of molecular weight plotted here corresponds to the spectrum of the experiments in thin polymer films of polystyrene[99] (the molecular weight L is given in number of monomers). The grey dots are the numerical results of a random walk simulation of the same problem. We observe a very good correspondance between the numerical simulations with a discrete random walk on lattice and the analytical formula with Brownian motion, even with a small number of steps the approximation of the random walk by the continuous process is accurate.

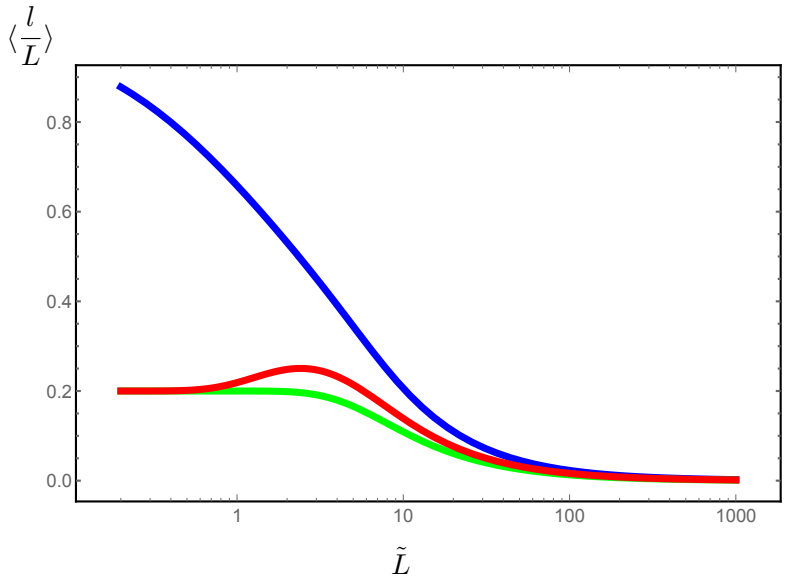

Figure 6.6 In this figure we plot the average length of bridge (blue), loop (green) or link (red) divided by the molecular weight L as a function of the auto-similar variable $\tilde{L}$. In large film or at small molecular weight, the average size of a loop tends to a plateau, indeed even if the film is large in the vicinity of the interface we will observe loops and their typical size will be 20 percent of the molecular weight. However the size of the bridge will tend to L while the film size is smaller than the molecular weight, indeed in a large film, the only possible bridges are stretched polymer chains from one interface to the other. Eventually in the confined regime ($L \to \infty$) all these lengths scale like h^2.

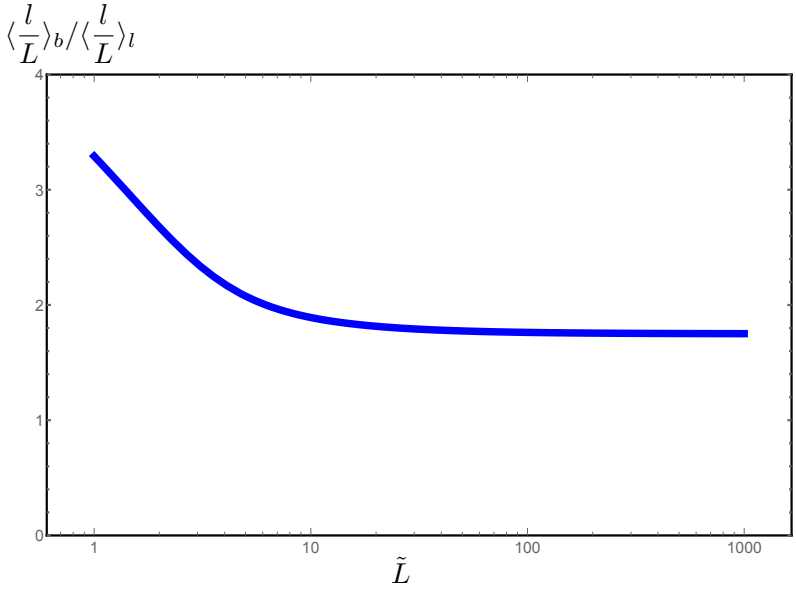

Figure 6.7 The bridge average length divided by the loop average length as a function of the auto-similar variable $\tilde{L}$. In confinement ($\tilde{L} \to \infty$) this ratio tends to exactly 7/4.

6.4.3 Conclusion

In this chapter we have computed the length probability density of bridge, loop and link inside free standing films and their exact dependency on the molecular weight. We have also discussed their proportion and average length inside the film, especially in the confined regime. The auto-similar nature of these statistics, the fact that the proportion of link and the link average length are independent of the molecular weight in very confined regime are in disagreement with the glass transition temperature observation. As h decreases, the observed glass transition temperature for different molecular weight tends to be more and more outspread [99]. This suggest that even if the relaxation process could occur via the bridge or loop, a physical ingredient must be strongly dependent on the molecular weight even in confinement, and this cannot be the bridge or loop statistics.

Conclusion

Conclusion

In this thesis we explored various aspects of interfaces and thin film physics.

In chapter 1, we begin by summarizing elementary properties of waves in deep water. We derive and discuss the fundamental properties of the dispersion relation of waves in water and by studying the dynamical equations of motion we are able to arrive at the integral expression of the surface displacement resulting from a boat moving at constant speed. This is more famously known as the Havelock equation. We further investigate an elementary solution to the point impulse Cauchy-Poisson problem and use it to derive the wake pattern following the historical work of Kelvin. The novel result in this chapter corresponds to our generalization of the Havelock formula for the wave resistance to any kind of motion or trajectory at the surface. The usual proof in literature is restrictive in that it assumes a steady state straight motion. We then use this generalisation of the Havelock formula to analytically compute the free deceleration of a particle at the surface of a fluid due to radiation. This provides theoretical validation to an experiment conducted by Marie Le Merrer [10].

In chapter 2, we begin with a theoretical investigation of the effects of a moving pressure disturbance above a thin elastic sheet which has been placed on top of a narrow viscous film. From the elastohydrodynamic lubrication model, we compute the wake and the associated wave resistance experienced by the operator. A central dimensionless parameter for this study appears to be the elastic Bond number. We then perform an asymptotic analysis of the low and high speed regimes and find a scaling for the maximum of the wave resistance, a reference point that could be important for designing nano-rheological setups. We conclude this chapter by demonstrating that the energy transfer to the fluid by deforming the interface is fully dissipated by viscous damping.

Chapter 3 presents an important novel study aimed at achieving a quantitative understanding of a water strider insect's locomotive mechanism. We begin by presenting a series of experimental and theoretical results on the surface displacement generated by the water strider's leg strokes. Using the synthetic Schlieren method, we are able to dynamically measure the topography of the air-water interface during a water strider's leg strokes with unprecedented accuracy. We extend Bühler's study to account for the finite depth of water, consistent with most experimental setups. We further demonstrate that accounting for the continuous forcing along the strider's leg trajectories is essential to reproduce the experimental wave patterns. This suggests that in the real conditions of the Gerris' natural habitat (including infinite depth: $H \gg \lambda$), Bühler's approach produces satisfactory results by superimposing the impulsive solution along the entire trajectories.

In Chapter 4 we shift our focus slightly and begin by reviewing some traditional

theories of glass transition including the cooperative string model first proposed by [59]. This model is our preferred one for further investigation because it captures the basic features of glass transition such as the Vogel-Fulcher-Tamman phenomenology and has the advantage of being able to theoretical model the physics of the glass transition shift in confined geometry. This is studied further in the following chapters.

We continue our investigations into the cooperative string model for glass transition by studying the effect of confinement for both free and attractive interfaces. Our studies reveal that the enhanced dynamics are primarily driven by the ratio of volume to free surface, rather than the geometry, as might be naively expected. We model this enhanced dynamic as due to the presence of a free surface by truncating the cooperative strings. This is followed by modelling a slower dynamic due to attractive interfaces by a process of additive cooperative strings. The aim of this study is to find a relaxation path and predict non monotonic decreases or increases of the glass transition temperature tuning both the free and the attractive interfaces in terms of reflectivity for the cooperative strings.

The final chapter of this thesis is devoted to computing the length probability density of bridges, loops and links inside free standing films and their exact dependency on the molecular weight of constituent particles. We discuss their proportion and average length inside the film, particularly in the confined regime. We demonstrate that these statistics are self-similar and that in the very confined regime, both the proportion of links and the average link length are independent from the molecular weight of the constituents. This is in disagreement with the glass transition temperature observation. As h decreases, the observed glass transition temperature for different molecular weights tends to be more outspread [99]. This suggests that even if the relaxation process could occur via bridges or loops, a physical component must be strongly dependent on the molecular weight even in confinement, and this cannot be the bridge or loop statistics.

Appendices

Appendix A

Mathematical tools

A.1 Principle of stationary phase

The method was shown by Kelvin in 1887 when he first explained the ship wave pattern. This method depends on the approximation if integrals of type:

$$I \;=\; \int_0^{+\infty} \mathrm{d}x \; f(x) e^{ig(x)} \; . \tag{A.1}$$

It is assumed that the circular function goes trough a large number of period within the interval of integration, whilst $f(x)$ changes much slowly comparatively to the phase argument. Under these assumptions, we understand that most part of the integral will be cancelled du to the phase oscillation except for the value inside the range of integration where the phase is stationary:

$$g'(\sigma) \;=\; 0 \; . \tag{A.2}$$

We assume here that we have only one stationary point, but the method is easily generalizable to multiple stationary points. One can approximate the integral using the Taylor expansion of $g(x) = g(\sigma) + g''(\sigma)\frac{x^2}{2}$ around this stationary point:

$$I \;\sim\; f(\sigma) \int_0^{+\infty} \mathrm{d}x \; e^{i\frac{1}{2}g''(\sigma)x^2} \; , \tag{A.3}$$

hence it becomes after integration:

$$I \;\sim\; \frac{\sqrt{\pi} f(\sigma)}{\sqrt{2|g''(\sigma)|}} e^{i(g(\sigma)+\mathrm{sign}(g''(\sigma)))} \; . \tag{A.4}$$

A.2 Green function

We consider a system inside a domaine D, $\boldsymbol{r}$ represents a point inside this domain. We suppose that the field $u(\boldsymbol{r})$ verifies:

$$\mathcal{L}u(r) = \rho(r) \tag{A.5}$$

with $\mathcal{L}$ a spatial linear operator. This equation can be solve for given boundary conditions (i.e. $u(\boldsymbol{r})$ fixed for $\boldsymbol{r} \in \partial D$). We can decomposed the function in an infinite number of source point:

$$\rho(\boldsymbol{r}) = \int_D \mathrm{d}\boldsymbol{r}' \rho(\boldsymbol{r}')\delta(\boldsymbol{r} - \boldsymbol{r} - r') \ . \tag{A.6}$$

Each elementary source produce an elementary field called the Green function of the operator $\mathcal{L}$, the Green function verifies:

$$\mathcal{L}G(\boldsymbol{r}, \boldsymbol{r}') = \delta(\boldsymbol{r} - \boldsymbol{r}') \ , \tag{A.7}$$

with the same boundary conditions on the Green function. Finding the Green function of the problem, the solution of Eq. (A.5) reads:

$$u(\boldsymbol{r}) = \int_D \mathrm{d}\boldsymbol{r}' G(\boldsymbol{r}, \boldsymbol{r}')\rho(\boldsymbol{r}') \ . \tag{A.8}$$

A.2.1 Spectral formula

If we now suppose that the operator $\mathcal{L}$ dispose of a complete basis of orthonormal eigenfunctions ϕ_n verifying the same boundary conditions. If we set λ_n has the eigenvalue associated to ϕ_n, therefore:

$$\mathcal{L}\phi_n = \lambda_n \phi_n \ . \tag{A.9}$$

The completeness of the eigenfunction basis imply that:

$$\sum_n \phi_n(\boldsymbol{r})\phi_n^*(\boldsymbol{r}') = \delta(\boldsymbol{r} - \boldsymbol{r}') \ . \tag{A.10}$$

One can verify that the inverse of the operator $\mathcal{L}$ has the same eigenfunctions associated with the eigenvalues λ_n^{-1}. If we invert Eq. (A.7) and insert Eq. (A.10) then we obtain the spectral representation of the Green function:

$$G(\boldsymbol{r}, \boldsymbol{r}') = \sum_n \frac{u_n(\boldsymbol{r})u_n(\boldsymbol{r}')}{\lambda_n} \tag{A.11}$$

Note that if we have a continuous spectrum of eigenvalues, the sum is replace by an integral.

A.2.2 Method of images

In electrostatics, it is common to encounter a situation where a plane infinite, taken for example in $x = 0$, is the wall of a conductor maintained at a zero potential. The conductor fills the half-space $x < 0$, the other half-space $x > 0$ being empty. If we want to calculate the electrostatic potential created by an external load distribution to the conductor, the most appropriate Green function is defined by:

$$-\Delta G(\mathbf{r};\mathbf{r}') = \delta(\mathbf{r}-\mathbf{r}') \ , \tag{A.12}$$

in the half-space defined by $x > 0$, with homogeneous Dirichlet boundary conditions, $G(\mathbf{r};\mathbf{r}') = 0$, on the conductive wall at $x = 0$ on the one hand, and infinitely in the empty half-space on the other hand. One can determine $G(\mathbf{r};\mathbf{r}')$ by using the spectral formula used previously. It is easy to compute the basis of eigenfunction associated to the Laplacian with the homogeneous Dirichlet boundary condition in $x = 0$:

$$\phi_{k_x,k_y,k_z}(\mathbf{r}) = \frac{2}{\sqrt{(2\pi)^3}} e^{i(k_y y + k_z z)} \sin(k_x x) \tag{A.13}$$

with $k_x > 0$ form an orthonormal basis in the half-space $x > 0$ canceling at $x = 0$. These functions check the relationship of completeness:

$$\int_0^\infty \mathrm{d}k_x \int_{-\infty}^\infty \mathrm{d}k_y \int_{-\infty}^\infty \mathrm{d}k_z \phi_{k_x,k_y,k_z}(\mathbf{r}) \phi^*_{k_x,k_y,k_z}(\mathbf{r}') = \delta(\mathbf{r}-\mathbf{r}') \tag{A.14}$$

By introducing the eigenfunctions into the spectral formula Eq. (A.11), we find:

$$G(\mathbf{r};\mathbf{r}') = \int_0^\infty \mathrm{d}k_x \int_{-\infty}^\infty \mathrm{d}k_y \int_{-\infty}^\infty \mathrm{d}k_z \frac{\phi_{k_x,k_y,k_z}(\mathbf{r}) \phi^*_{k_x,k_y,k_z}(\mathbf{r}')}{\mathbf{k}^2}. \tag{A.15}$$

After integration one finds:

$$G(\mathbf{r};\mathbf{r}') = G_0(\mathbf{r}-\mathbf{r}') - G_0(\mathbf{r}-\mathbf{r}'_{\mathrm{im}}) \ , \tag{A.16}$$

with $\mathbf{r}'_{\mathrm{im}} = (-x', y', z')$ and G_0 the Green function of the Laplacian without boundary. In 3D it reads:

$$G_0(\mathbf{r}-\mathbf{r}') = \frac{1}{4\pi|\mathbf{r}-\mathbf{r}'|}. \tag{A.17}$$

Appendix B

Soft levelling

PHYSICAL REVIEW FLUIDS **2**, 094001 (2017)

Elastocapillary levelling of thin viscous films on soft substrates

Marco Rivetti,[1] Vincent Bertin,[2] Thomas Salez,[2,3] Chung-Yuen Hui,[4] Christine Linne,[1] Maxence Arutkin,[2] Haibin Wu,[4] Elie Raphaël,[2] and Oliver Bäumchen[1,*]

[1]*Max Planck Institute for Dynamics and Self-Organization (MPIDS), Am Faßberg 17, 37077 Göttingen, Germany*

[2]*Laboratoire de Physico-Chimie Théorique, UMR CNRS 7083 Gulliver, ESPCI Paris, PSL Research University, 10 rue Vauquelin, 75005 Paris, France*

[3]*Global Station for Soft Matter, Global Institution for Collaborative Research and Education, Hokkaido University, Sapporo, Hokkaido 060-0808, Japan*

[4]*Department of Mechanical & Aerospace Engineering, Cornell University, Ithaca, New York 14853, USA*

(Received 31 March 2017; published 1 September 2017)

A thin liquid film with nonzero curvature at its free surface spontaneously flows to reach a flat configuration, a process driven by Laplace pressure gradients and resisted by the liquid's viscosity. Inspired by recent progresses on the dynamics of liquid droplets on soft substrates, we here study the relaxation of a viscous film supported by an elastic foundation. Experiments involve thin polymer films on elastomeric substrates, where the dynamics of the liquid-air interface is monitored using atomic force microscopy. A theoretical model that describes the coupled evolution of the solid-liquid and the liquid-air interfaces is also provided. In this soft-levelling configuration, Laplace pressure gradients not only drive the flow, but they also induce elastic deformations on the substrate that affect the flow and the shape of the liquid-air interface itself. This process represents an original example of elastocapillarity that is not mediated by the presence of a contact line. We discuss the impact of the elastic contribution on the levelling dynamics and show the departure from the classical self-similarities and power laws observed for capillary levelling on rigid substrates.

DOI: 10.1103/PhysRevFluids.2.094001

I. INTRODUCTION

Interactions of solids and fluids are often pictured by the flapping of a flag in the wind, the oscillating motion of an open hosepipe, or that of a fish fin in water, a set of examples in which the inertia of the fluid plays an essential role. In contrast, at small scales, and more generally for low-Reynolds-number (Re) flows, fluid-solid interactions involve viscous forces rather than inertia. Of particular interest are the configurations where a liquid flows along a soft wall, i.e., an elastic layer that can deform under the action of pressure and viscous stresses. For instance, when a solid object moves in a viscous liquid close to an elastic wall, the intrinsic symmetry of the Stokes equations that govern low-Re flows breaks down. This gives rise to a qualitatively different—elastohydrodynamical—behavior of the system in which the moving object may experience lift or oscillating motion [1–3], and a swimmer can produce a net thrust even by applying a time-reversible stroke [4], in apparent violation of the so-called scallop theorem [5]. This coupling of viscous dynamics and elastic deformations is particularly significant in lubrication problems, such as the aging of mammalian joints and their soft cartilaginous layers [6], or roll-coating processes involving rubber-covered rolls [7], among others.

When adding a liquid-vapor interface, capillary forces may come into play, thus allowing for elastocapillary interactions. The latter have attracted a lot of interest in the past decade [8–10]. In order to enhance the effect of capillary forces, the elastic object has to be either slender or soft. The

*oliver.baeumchen@ds.mpg.de

first case, in which the elastic structure is mainly bent by surface tension, has been explored to explain and predict features like deformation and folding of plates, wrapping of plates (capillary origami) or fibers around droplets, and liquid imbibition between fibers [11–18]. The second case involves rather thick substrates, where capillary forces are opposed by bulk elasticity. A common example is that of a small droplet sitting on a soft solid. Lester [19] has been the first to recognize that the three-phase contact line can deform the substrate by creating a ridge. Despite the apparent simplicity of this configuration, the substrate deformation close to the contact line represents a challenging problem because of the violation of the classical Young's construction for the contact angle, the singularity of the displacement field at the contact line, and the difficulty to predict the exact shape of the capillary ridge. In the last few years, several theoretical and experimental works have contributed to a better fundamental understanding of this static problem [20–25], recently extended by the dynamical case of droplets moving along a soft substrate [26–28].

Besides, another class of problems—the capillary levelling of thin liquid films on rigid substrates, or in freestanding configurations—has been studied in the last few years using thin polymer films featuring different initial profiles, such as steps, trenches, and holes [29–34]. From the experimental point of view, this has been proven to be a reliable system due to systematic reproducibility of the results and the possibility to extract rheological properties of the liquid [35,36]. A theoretical framework, based on Stokes flow and the lubrication approximation, results in the so-called thin-film equation [37], which describes the temporal evolution of the thickness profile. From this model, characteristic self-similarities of the levelling profiles, as well as numerical [38] and analytical [39,40] solutions have been derived, which were found in excellent agreement with the experimental results. Furthermore, coarse-grained molecular dynamics models allowed us to extend the framework of capillary levelling by offering local dynamical insights and probing viscoelasticity [41].

In this article, by combining the two classes of problems above—elastocapillarity and capillary levelling—we design a dynamical elastocapillary situation free of any three-phase contact line. Specifically, we consider a setting in which a thin layer of viscous liquid with a nonflat thickness profile is supported onto a soft foundation. The liquid-air interface has a spatially varying curvature that leads to gradients in Laplace pressure, which drive flow coupled to substrate deformation. The resulting elastocapillary levelling might have practical implications in biological settings and nanotechnology.

II. EXPERIMENTAL SETUP

First, polydimethylsiloxane (PDMS, Sylgard 184, Dow Corning) is mixed with its curing agent in ratios varying from 10:1 to 40:1. In order to decrease its viscosity, liquid PDMS is diluted in toluene (Sigma-Aldrich, Chromasolv, purity $>99.9\%$) to obtain a 1:1 solution in weight. The solution is then poured on a 15×15 mm Si wafer (Si-Mat, Germany) and spin-coated for 45 s at 12.000 RPM. The sample is then immediately transferred to an oven and kept at $75\,^{\circ}$C for 2 h. The resulting elastic layer has a thickness $s_0 = 1.5 \pm 0.2\ \mu$m, as obtained from atomic force microscopy (AFM, Multimode, Bruker) data. The Young's modulus of PDMS strongly depends on the ratio of base to cross linker, with typical values of $E = 1.7 \pm 0.2$ MPa for 10:1 ratio, $E = 600 \pm 100$ kPa for 20:1, and $E = 50 \pm 20$ kPa for 40:1 [42,43].

In order to prepare polystyrene (PS) films exhibiting nonconstant curvatures, we employ a technique similar to that described in [29]. Solutions of 34 kg/mol PS (PSS, Germany, polydispersity <1.05) in toluene with typical concentrations varying between 2% and 6% are made. A solution is then spin-cast on a freshly cleaved mica sheet (Ted Pella, USA) for about 10 s, with typical spinning velocities on the order of a few thousands RPM. After the rapid evaporation of the solvent during the spin-coating process, a thin (glassy) film of PS is obtained, with a typical thickness of 200–400 nm.

To create the geometry required for the levelling experiment, a first PS film is floated onto a bath of ultrapure (MilliQ) water. Due to the relatively low molecular weight of the PS employed here, the glassy film spontaneously ruptures into several pieces. A second (uniform) PS film on

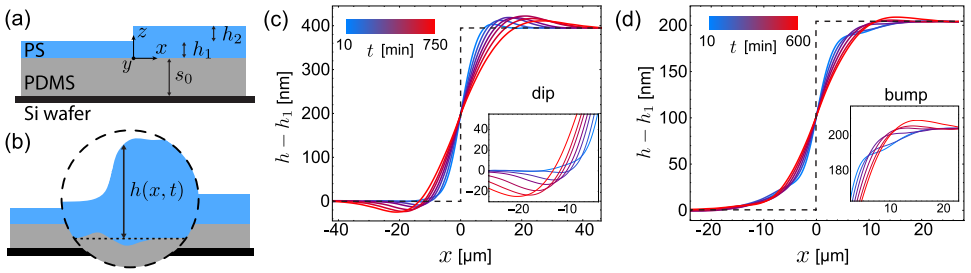

FIG. 1. (a) Schematics of the initial geometry: a stepped liquid polystyrene (PS) film is supported by an elastic layer of polydimethylsiloxane (PDMS). (b) Schematics of the levelling dynamics: the liquid height h depends on the horizontal position x and the time t. The elastic layer deforms due to the interaction with the liquid. (c) Experimental profiles of the liquid-air interface during levelling at $T_a = 140\,^\circ$C on 10:1 PDMS. The initial step has $h_1 = h_2 = 395$ nm. The inset shows a closeup of the dip region. (d) Experimental profiles during levelling at $T_a = 140\,^\circ$C on the softer 40:1 PDMS. The initial step has $h_1 = h_2 = 200$ nm. The inset shows a magnification of the bump region. Dashed lines in (c) and (d) indicate the initial condition.

mica is approached to the surface of water, put into contact with the floating PS pieces and rapidly released as soon as the mica touches the water. That way a collection of PS pieces is transferred onto the second PS film, forming a discontinuous double layer that is then floated again onto a clean water surface. At this stage, a sample with the elastic layer of PDMS is put into the water and gently approached to the floating PS from underneath. As soon as contact between the PS film and the PDMS substrate is established, the sample is slowly released from the bath. Finally, the initial configuration depicted in Fig. 1(a) is obtained. For a direct comparison with capillary levelling on rigid substrates, we also prepared stepped PS films of the same molecular weight on freshly cleaned Si wafers (Si-Mat, Germany) using the same transfer procedure.

Using an optical microscope we identify spots where isolated pieces of PS on the uniform PS layer display a clean and straight interfacial front. A vertical cross section of these spots corresponds to a stepped PS-air interface, which is invariant in the y dimension [see Fig. 1(a) for a sketch of this geometry]. Using AFM, the 3D shape of the interface is scanned and a 2D profile is obtained by averaging along y. From this profile the initial height of the step h_2 is measured. The sample is then annealed at an elevated temperature $T_a = 120$–$160\,^\circ$C (above the glass-transition temperature of PS) using a high-precision heating stage (Linkam, UK). During this annealing period the liquid PS flows. Note that on the experimental time scales and for the typical flow velocities studied here the PS is well described by a Newtonian viscous fluid [29,31–34] (viscoelastic and non-Newtonian effects are absent since the Weissenberg number $\mathrm{Wi} \ll 1$ and the Deborah number $\mathrm{De} \ll 1$). After a given annealing time t, the sample is removed from the heating stage and quenched at room temperature (below the glass-transition temperature of PS). The three-dimensional (3D) PS-air interface in the zone of interest is scanned with the AFM and a 2D profile is again obtained by averaging along y. This procedure is repeated several times in order to monitor the temporal evolution of the height $h(x,t)$ of the PS-air interface [defined with respect to the undeformed elastic-liquid interface; see Fig. 1(b)]. At the end of each experiment, the thickness h_1 of the uniform PS layer is measured by AFM.

III. EXPERIMENTAL RESULTS AND DISCUSSION

A. Profile evolution

The temporal evolutions of two typical profiles are reported in Figs. 1(c) and 1(d), corresponding to films that are supported by elastic foundations made of 10:1 PDMS and 40:1 PDMS, respectively. As expected, the levelling process manifests itself in a broadening of the initial step over time.

In all profiles, three main regions can be identified (from left to right): a region with positive curvature (negative Laplace pressure in the liquid), an almost linear region around $x = 0$ (zero Laplace pressure), and a region of negative curvature (positive Laplace pressure in the liquid). These regions are surrounded by two unperturbed flat interfaces exhibiting $h = h_1$ and $h = h_1 + h_2$. In analogy with earlier works on rigid substrates [31], we refer to the positive-curvature region of the profile as the *dip*, and the negative-curvature region as the *bump*. Close-up views of those are given in the insets of Figs. 1(c) and 1(d).

The decrease of the slope of the linear region is a direct consequence of levelling. A less intuitive evolution is observed in the bump and dip regions. For instance, in the first profile of Fig. 1(c), recorded after 10 min of annealing, a bump has already emerged while a signature of a dip cannot be identified yet. As the interface evolves in time, a dip appears and both the bump and the dip grow substantially. At a later stage of the evolution, the height of the bump and the depth of the dip eventually saturate. This vertical evolution of the bump and the dip is at variance with what has been observed in the rigid-substrate case [29,31], where the values of the maximum and the minimum are purely dictated by h_1 and h_2 and stay fixed during the experimentally accessible evolution. That specific signature of the soft foundation is even amplified for PS levelling on the softer (40:1 PDMS) foundation; see Fig. 1(d). The evolution of the bump and dip results from the interaction between the liquid and the soft foundation. Indeed, the curvature gradients of the liquid-air interface give rise to Laplace pressure gradients that drive the flow. The pressure and flow fields both induce elastic deformations in the substrate. Intuitively, the negative Laplace pressure below the dip results in a traction that pulls upwards on the PDMS substrate, while the positive Laplace pressure below the bump induces a displacement in the opposite direction. In addition, a no-slip condition at the solid-liquid interface coupled to the flow induces an horizontal displacement field in the PDMS substrate. These displacements of the foundation act back on the liquid-air interface by volume conservation. According to this picture, the displacement of the solid-liquid interface is expected to tend to zero over time, since the curvature gradients of the liquid-air interface and the associated flow decrease.

B. Temporal evolution of the profile width

The capillary levelling on a rigid substrate possesses an exact self-similar behavior in the variable $x/t^{1/4}$, leading to a perfect collapse of the rescaled height profiles of a given evolution [31]. In contrast, for a soft foundation, no collapse of the profiles is observed (not shown) when the horizontal axis x is divided by $t^{1/4}$.

To determine whether another self-similarity exists or not, we first quantify the horizontal evolution of the profile by introducing a definition of its width [see Fig. 2(a), inset]: $w(t) = x(h = h_1 + 0.6\,h_2) - x(h = h_1 + 0.4\,h_2)$. With this definition, only the linear region of the profile matters and the peculiar shapes of the dip and bump do not affect the value of w. The temporal evolution of w was measured in several experiments, featuring different values of h_1, h_2 as well as three stiffnesses of the soft foundation. First, the absolute value of w at a given time is larger for thicker liquid films, as expected since more liquid can flow. Second, the data plotted in Fig. 2(a) clearly show that in all these experiments the width increases as $w \sim t^{1/6}$. Equivalently, dividing the horizontal axis x by $t^{1/6}$ leads to a collapse of all the linear regions of the profiles, as shown in Figs. 2(b) and 2(c). However, while allowing for the appreciation of the vertical evolution of the bump and dip, the noncollapse of the full profiles indicates the absence of true self-similarity in the problem. Nevertheless, we retain that for practical purposes associated with elastocapillary levelling, the $w \sim t^{1/6}$ scaling encompasses most of the evolution in terms of flowing material.

C. Role of viscosity

The impact of the soft foundation on the levelling dynamics depends on two essential aspects: the stiffness of the foundation and how strongly the liquid acts on it. The first aspect is constant, and

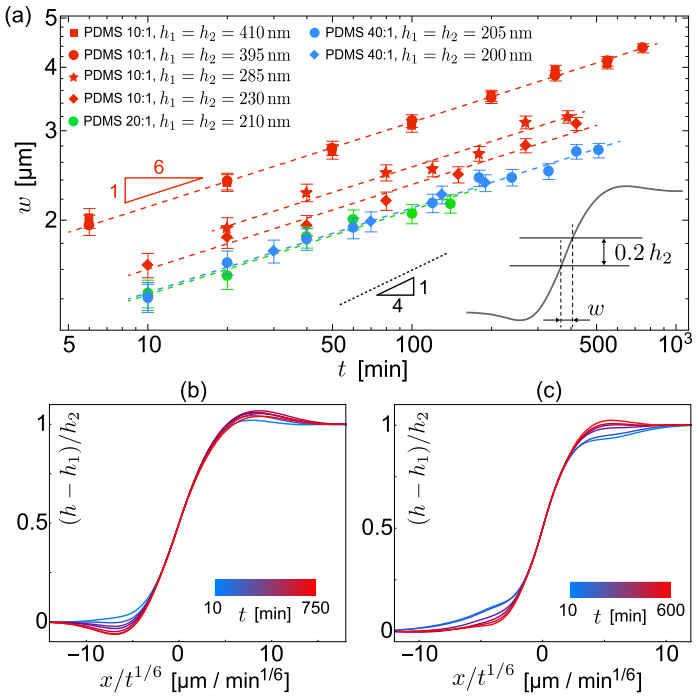

FIG. 2. (a) Experimental evolution of the profile width w (proportional to the lateral extent of the linear region as displayed in the inset) as a function of time t, in log-log scale, for samples involving different liquid-film thicknesses and substrate elasticities. All datasets seem to exhibit a $t^{1/6}$ power law. The slope corresponding to a $t^{1/4}$ evolution (rigid-substrate case) is displayed for comparison. (b) Experimental levelling profiles on 10:1 PDMS from Fig. 1(c) with the horizontal axis rescaled by $t^{-1/6}$. (c) Same rescaling applied for the levelling profiles on 40:1 PDMS shown in Fig. 1(d).

controlled by both the Young's modulus E and the thickness s_0 of the (incompressible) PDMS layer, the former being fixed by the base-to-cross-linker ratio. The second aspect is ultimately controlled by the Laplace pressure, which is directly related to the curvature of the liquid-air interface. Even for a single experiment, the amplitude of the curvature field associated with the profile evolves along time, from large values at early times, to small ones at long times when the profile becomes almost flat. Thus, we expect the relative impact of the soft foundation to change over time.

This time dependence can be explored by adjusting the PS viscosity. Indeed, the latter strongly decreases for increasing annealing temperature, while the other quantities remain mostly unaffected by this change. Hence, the levelling dynamics can be slowed down by performing experiments at lower annealing temperature, in order to investigate the dynamics close to the initial condition, and accelerated at higher annealing temperature in order to access the late-stage dynamics. Here, we report on experiments at 120 °C (high viscosity) and 160 °C (low viscosity) and compare the results to our previous experiments at 140 °C.

Following lubrication theory [37], the typical time scale of a levelling experiment is directly fixed by the capillary velocity γ/η, where γ denotes the PS-air surface tension and η the PS viscosity, as well as the thickness $h_0 = h_1 + h_2/2$ of the PS film. In Fig. 3, the experimental profile width is plotted as a function of $\gamma h_0{}^3 t/\eta$ [31], for experiments involving different liquid film thicknesses, substrate elasticities, and annealing temperatures. Samples with PS stepped films on bare (rigid) Si wafers were used to measure the capillary velocity γ/η at different annealing temperatures [36]. In these calibration measurements, the profile width follows a $t^{1/4}$ power law, as expected [31]. In

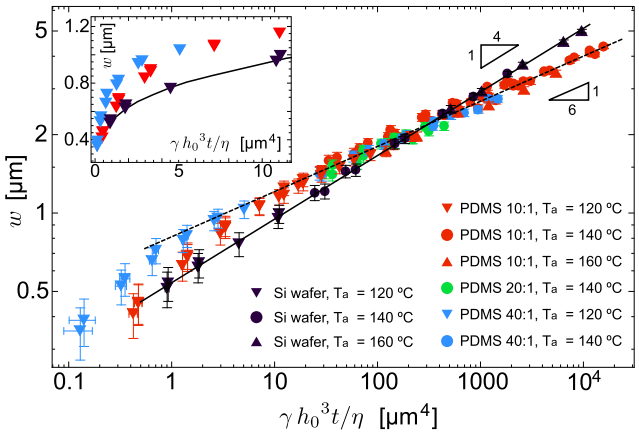

FIG. 3. Experimental profile width w [see Fig. 2(a), inset] as a function of $\gamma h_0{}^3 t/\eta$ (see definitions in text), in log-log scale, for all the different samples and temperatures. Experiments for 10:1 (red), 20:1 (green), and 40:1 (blue) PDMS substrates, as well as annealing temperatures $T_a = 120\,^\circ$C (down triangle), $140\,^\circ$C (circle), $160\,^\circ$C (up triangle) are displayed. Most of the data collapses on a single curve of slope 1/6 (dashed line). The data for capillary levelling on rigid substrates (black symbols) are shown for comparison and collapse on a single curve of slope 1/4 (solid line). The inset displays a closeup of the early-time regime in linear representation.

contrast, for the experiments on elastic foundations, two different regimes might be distinguished: for $\gamma h_0{}^3 t/\eta$ larger than $\sim 5\ \mu$m^4, the width follows a $t^{1/6}$ power law and all datasets collapse onto a single master curve over three to four orders of magnitude on the horizontal scale; for values of $\gamma h_0{}^3 t/\eta$ smaller than $\sim 5\ \mu$m^4, the evolution depends on the elastic modulus and it appears that the softer the foundation the faster the evolution (see inset of Fig. 3).

D. Vertical evolution of the dip and bump

Guided by the previous discussion, we now divide the horizontal axis x of all the height profiles in different experiments by the quantity $(\gamma h_0{}^3 t/\eta)^{1/6}$. As shown in Fig. 4, this rescaling leads to a collapse in the linear region of the profiles, while the dip and the bump regions display significant deviations from a universal collapse.

In order to characterize these deviations, we introduce the Maxwell-like viscoelastic time η/E and define the dimensionless time $\tau = Et/\eta$. This dimensionless parameter quantifies the role of the deformable substrate: experiments on softer foundations (lower E) or evolving slower (larger η) correspond to smaller values of τ, and are therefore expected to show more pronounced elastic behaviors. As seen in Fig. 4, we find a systematic trend when plotting the experimental levelling profiles using the parameter τ. Profiles with large τ (dark green and black) display clear bumps and dips, comparable in their vertical extents to the corresponding features observed on rigid substrates (not shown). In contrast, profiles with small τ (yellow and bright green) feature large deviations with respect to this limit.

The previous observation can be quantified by tracking the temporal evolution of the height of the liquid-air interface $h_d(t) = h(x_d, t)$ at the dip position x_d, which we define as the (time-independent) position at which the global minimum is located at the latest time of the levelling dynamics (see arrow in Fig. 4). The inset of Fig. 4 displays the normalized difference between h_d and the corresponding value for a rigid substrate $h_{d,rig}$, plotted as a function of τ. We find that the parameter τ allows for a reasonable rescaling of the data. As anticipated, the difference between levelling on rigid and soft substrates decreases monotonically as a function of this dimensionless time. For small τ, the

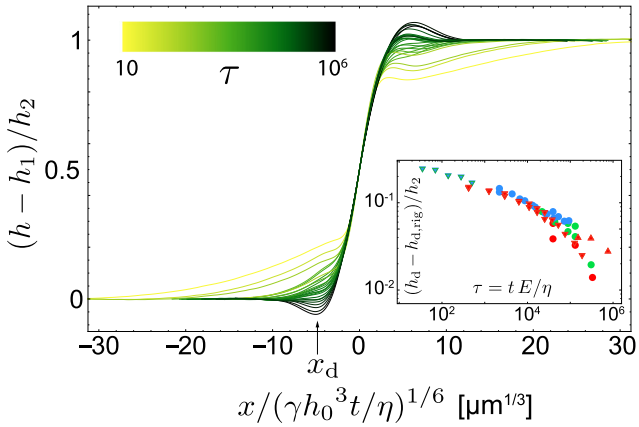

FIG. 4. Rescaled experimental profiles for all data displayed in Fig. 3, color coded according to the dimensionless time $\tau = tE/\eta$. Inset: Evolution with τ of the normalized distance between the height h_d of the liquid-air interface at the dip position x_d and the corresponding value $h_{d,rig}$ for the rigid case. Note that in all the experiments $h_1 = h_2$. Symbols are chosen to be consistent with Fig. 3.

difference can be larger than 20% of the liquid film thickness, while for large τ it drops to less than 1%, which corresponds to the vertical resolution of the AFM.

IV. THEORETICAL MODELLING

A. Model and solutions

We consider an incompressible elastic slab atop which a viscous liquid film with an initial stepped liquid-air interface profile is placed. The following hypotheses are retained: (i) the height h_2 of the step is small as compared to the thickness $h_0 = h_1 + h_2/2$ of the (flat) equilibrium liquid profile; (ii) the slopes at the liquid-air interface are small, such that the curvature of the interface can be approximated by $\partial_x^2 h$; (iii) the lubrication approximation applies in the liquid, i.e., typical vertical length scales are much smaller than horizontal ones; (iv) the components of the displacement field in the elastic material are small compared to the thickness of the elastic layer (linear elastic behavior); (v) the elastic layer is incompressible (valid assumption for PDMS). Note that the hypotheses (i)–(iii) have been successfully applied in previous work on the levelling dynamics of a stepped perturbation of a liquid film placed on a rigid substrate [39].

Below, we summarize the model, the complete details of which are provided in the Supplemental Material [44]. The main difference with previous work [39] is the coupling of fluid flow and pressure to elastic deformations of the substrate. The Laplace pressure is transmitted by the fluid and gives rise to a vertical displacement $\delta(x,t)$ of the solid-liquid interface, and thus a horizontal displacement $u_s(x,t)$ of the latter by incompressibility. Consequently, the no-slip condition at the solid-liquid interface implies that a fluid element in contact with the elastic surface will have a nonzero horizontal velocity $\partial_t u_s$. In addition, we assume no shear at the liquid-air interface. After linearization, the modified thin-film equation reads

$$\frac{\partial \Delta}{\partial t} + \frac{\partial}{\partial x}\left[-\frac{h_0^3}{3\eta}\frac{\partial p}{\partial x} + h_0 \frac{\partial u_s}{\partial t}\right] = 0, \tag{1}$$

where $\Delta(x,t) = h(x,t) - \delta(x,t) - h_0$ is the excess thickness of the liquid layer with respect to the equilibrium value h_0. The excess pressure $p(x,t)$ in the film, with respect to the atmospheric value,

is given by the (small-slope) Laplace pressure:

$$p \simeq -\gamma \frac{\partial^2(\Delta+\delta)}{\partial x^2}. \tag{2}$$

Furthermore, the surface elastic displacements are related to the pressure field through

$$\delta = -\frac{1}{\sqrt{2\pi}\,\mu}\int_{-\infty}^{\infty} k(x-x')p(x',t)\,dx', \tag{3}$$

$$u_s = -\frac{1}{\sqrt{2\pi}\,\mu}\int_{-\infty}^{\infty} k_s(x-x')p(x',t)\,dx', \tag{4}$$

where $\mu = E/3$ is the shear modulus of the incompressible substrate, and where $k(x)$ and $k_s(x)$ are the Green's functions (see Supplemental Material [44]) for the vertical and horizontal surface displacements, i.e., the fundamental responses due to a linelike pressure source of magnitude $-\sqrt{2\pi}\mu$ acting on the surface of the infinitely long elastic layer.

Equations (1)–(4) can be solved analytically using Fourier transforms (see Supplemental Material [44]), and we obtain

$$\tilde{\Delta}(\lambda,t) = -\frac{h_2}{2i\lambda}\sqrt{\frac{2}{\pi}}\exp\left[-\left(\frac{\gamma\lambda^4 h_0^3}{3\eta}\right)\frac{t}{1+(\gamma\lambda^2/\mu)(\tilde{k}+i\lambda h_0\tilde{k}_s)}\right], \tag{5}$$

$$\tilde{\delta} = \frac{-\tilde{k}}{\mu}\frac{\gamma\lambda^2\tilde{\Delta}}{[1+(\gamma\lambda^2/\mu)\tilde{k}]}, \tag{6}$$

where $\tilde{}$ denotes the Fourier transform of a function and λ is the conjugated Fourier variable, i.e., $\tilde{f}(\lambda) = \frac{1}{\sqrt{2\pi}}\int_{-\infty}^{\infty} f(x)e^{i\lambda x}\,dx$. The vertical displacement $h(x,t) - h_0$ of the liquid-air interface with respect to its final state is then determined by summing the inverse Fourier transforms of Eqs. (5) and (6).

Figure 5(a) displays the theoretical profiles of both the liquid-air interface $z = h(x,t)$ and the solid-liquid interface $z = \delta(x,t)$, for a stepped liquid film with thicknesses $h_1 = h_2 = 2h_0/3 =$ 120 nm, supported by a substrate of stiffness $\mu = 25$ kPa and thickness $s_0 = 2$ μm. The viscosity $\eta = 2.5 \times 10^6$ Pa s is adapted to the PS viscosity at the annealing temperature $T_a = 120\,^\circ$C in the experiment. The PS-air surface tension is fixed to $\gamma = 30$ mN/m [45]. We find that the profiles predicted by this model reproduce some of the key features observed in our experiments. In particular, the evolutions of the bump and dip regions in the theoretical profiles (see Fig. 5 inset) qualitatively capture the characteristic behaviors recorded in the experiment [see Fig. 1(c) inset].

An advantage of this theoretical approach is the possibility to extract information about the deformation of the solid-liquid interface. As shown in Fig. 5, the substrate deforms mainly in the bump and dip regions, as a result of their large curvatures. The maximal vertical displacement of the solid-liquid interface in this example is ~25 nm, and it reduces over time, due to the levelling of the profile and the associated lower curvatures.

B. Evolution of the profile width

The temporal evolution of the width w [see Fig. 2(a), inset] of the profiles was extracted from our theoretical model for a series of different parameters. Figure 6 shows the theoretical width w as a function of the quantity $\gamma h_0{}^3 t/\eta$ for all cases studied. With this rescaling, it is evident that the width of the theoretical profile depends strongly on elasticity at early times, while all datasets collapse onto a single curve at long times. Moreover, this master curve exhibits a slope of 1/4, and thus inherits a characteristic signature of capillary levelling on a rigid substrate. The early-time data show that the width is larger than on a rigid substrate, but with a slower evolution and thus a lower effective exponent. These observations are in qualitative agreement with our experimental data. However,

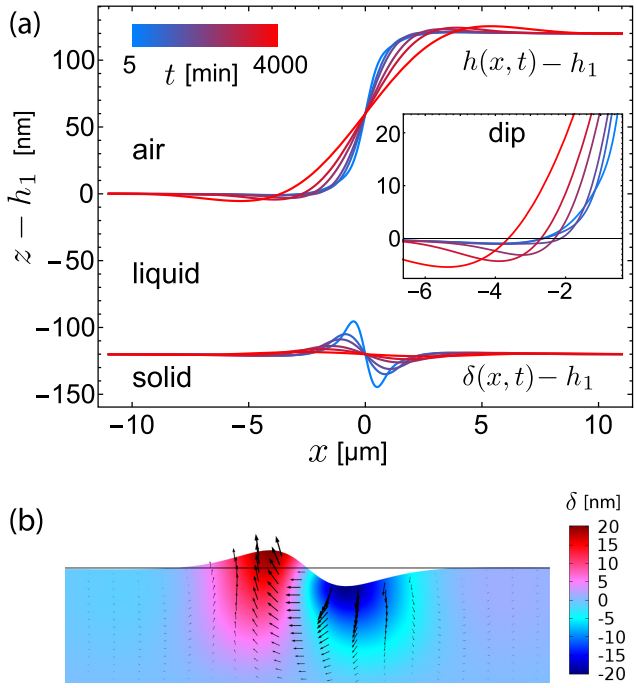

FIG. 5. (a) Theoretical profiles for the liquid-air interface $z = h(x,t)$ and the solid-liquid interface $z = \delta(x,t)$, both shifted vertically by $-h_1$. Here, we employ $s_0 = 2$ μm, $h_1 = h_2 = 2h_0/3 = 120$ nm, $\mu = 25$ kPa, $\gamma = 30$ mN/m, $\eta = 2.5 \times 10^6$ Pa s. The inset displays a close-up of the dip region. (b) Finite-element simulation (COMSOL) of the solid's total displacement (black arrows) and its vertical component δ (color code). The result has been obtained by imposing the Laplace pressure field corresponding to the first profile in (a) to a slab of elastic material exhibiting comparable geometrical and mechanical properties as in (a). The maximal displacement of 22 nm is in good agreement with the theoretical prediction shown in (a).

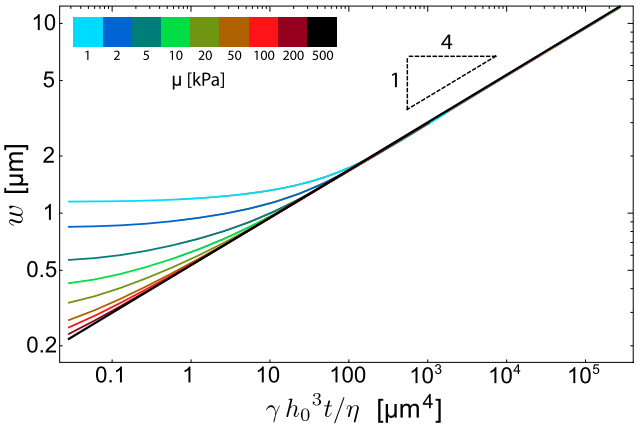

FIG. 6. Temporal evolution of the profile width [see definition in Fig. 2(a), inset], in log-log scale, as predicted by the theoretical model, for different shear moduli, viscosities, and liquid-film thicknesses. The 1/4 power law corresponding to a rigid substrate is indicated.

interestingly, we do not recover in the experiments the predicted transition to a long-term rigidlike $1/4$ exponent, but instead keep a $1/6$ exponent (see Fig. 3).

It thus appears that we do not achieve a full quantitative agreement between the theoretical and experimental profiles. The initially sharp stepped profile could possibly introduce an important limitation on the validity of the lubrication hypothesis. Indeed, while this is not a problem for the rigid case since the initial condition is rapidly forgotten [40], it is not *a priori* clear if and how elasticity affects this statement. We thus checked (see Supplemental Material [44]) that replacing the lubrication approximation by the full Stokes equations for the liquid part does not change notably the theoretical results. We also checked that the linearization of the thin-film equation is not the origin of the aforementioned discrepancy: in a test experiment with $h_2 \ll h_1$ on a soft substrate we observed the same characteristic features—and especially the $1/6$ temporal exponent absent of the theoretical solutions—as the ones reported for the $h_1 \approx h_2$ geometry (see Supplemental Material [44]). Besides, we note that while the vertical deformations of the elastic material (see Fig. 5) are small compared to the thickness s_0 of the elastic layer in the experimentally accessible temporal range, the assumption of small deformations could be violated at earlier times without affecting the long-term behavior at stake.

Finally, we propose a simplified argument to qualitatively explain the smaller transient exponent in Fig. 6. We assume that the vertical displacement $\delta(x,t)$ of the solid-liquid interface mostly translates the liquid above, such that the liquid-air interface displaces vertically by the same amount, following

$$h(x,t) = h_{\mathrm{r}}(x,t) + \delta(x,t), \tag{7}$$

where h_{r} is the profile of the liquid-air interface that would be observed on a rigid substrate. Note that this simplified mechanism does not violate conservation of volume in the liquid layer. By deriving the previous equation with respect to x, and evaluating it at the center of the profile ($x = 0$), we obtain an expression for the central slope of the interface:

$$\partial_x h(0,t) = \partial_x h_{\mathrm{r}}(0,t) + \partial_x \delta(0,t). \tag{8}$$

Due to the positive (negative) displacement of the solid-liquid interface in the region $x < 0$ ($x > 0$), $\partial_x \delta(0,t)$ is always negative, as seen in Fig. 5. Therefore, we expect a reduced slope of the liquid-air interface in the linear region, which is in agreement with the increased width observed on soft substrates. Moreover, taking the second derivative of Eq. (7) with respect to x leads to

$$\partial_x^2 h(x,t) = \partial_x^2 h_{\mathrm{r}}(x,t) + \partial_x^2 \delta(x,t). \tag{9}$$

In the dip region, $h_{\mathrm{r}}(x,t)$ is convex in space (positive second derivative with respect to x), while $\delta(x,t)$ is assumed to be concave in space (negative second derivative with respect to x) up to some distance from the center (see Fig. 5). Therefore, the resulting curvature is expected to be reduced. A similar argument leads to the same conclusion in the bump region. This effect corresponds to a reduction of the Laplace pressure and, hence, of the driving force for the levelling process: the evolution is slower which translates into a smaller effective exponent.

C. Finite-element simulations

To check the validity of the predicted shape of the solid-liquid interface, we performed finite-element simulations using COMSOL Multiphysics. Starting from an experimental profile of the liquid-air interface at a given time t, the curvature and the resulting pressure field $p(x,t)$ were extracted. This pressure field was used as a top boundary condition for the stress in a 2D slab of an incompressible elastic material exhibiting a comparable thickness and stiffness as in the corresponding experiment. The slab size in the x direction was chosen to be 20 μm, which is large enough compared to the typical horizontal extent of the elastic deformation [see Fig. 5(a)]. The bottom boundary of the slab was fixed (zero displacement), while the left and right boundaries were let free (zero stress). The deformation field predicted by these finite-element simulations is shown in Fig. 5(b) and found to be in quantitative agreement with our theoretical prediction.

V. CONCLUSION

We report on the elastocapillary levelling of a thin viscous film flowing above a soft foundation. The experiments involve different liquid film thicknesses, viscosities, and substrate elasticities. We observe that the levelling dynamics on a soft substrate is qualitatively and quantitatively different with respect to that on a rigid substrate. At the earliest times, the lateral evolution of the profiles is faster on soft substrates than on rigid ones, as a possible result of the "instantaneous" substrate deformation caused by the capillary pressure in the liquid. Immediately after, this trend reverses: the lateral evolution of the profiles on soft substrates becomes slower than on rigid ones, which might be related to a reduction of the capillary driving force associated with the elastic deformation. Interestingly, we find that the width of the liquid-air interface follows a $t^{1/6}$ power law over several orders of magnitude on the relevant scale, in sharp contrast with the classical $t^{1/4}$ law observed on rigid substrates.

To the best of our knowledge, this system is a unique example of dynamical elastocapillarity that is not mediated by the presence of a contact line, but only by the Laplace pressure inside the liquid. Notwithstanding, this process is not trivial, since the coupled evolutions of both the liquid-air and solid-liquid interfaces lead to an intricate dynamics. Our theoretical approach, based on linear elasticity and lubrication approximation, is able to reproduce some observations, such as the typical shapes of the height profiles and the dynamics at short times.

While some characteristic experimental features are captured by the model, a full quantitative agreement is still lacking to date. Given the careful validation of all the basic assumptions underlying our theoretical approach (i.e., lubrication approximation, linearization of the thin-film equation, and linear elasticity), we hypothesize that additional effects are present in the materials or experiments. For instance, it remains unclear whether the physicochemical and rheological properties at the surface of PDMS films, which were prepared using conventional recipes, are correctly described by bulk-measured quantities [9]. We believe that further investigations of the elastocapillary levelling on soft foundations, using different elastic materials and preparation schemes, could significantly advance the understanding of such effects and dynamic elastocapillarity in general.

Finally, we would like to stress that the signatures of elasticity in the elastocapillary levelling dynamics are prominent even on substrates that are not very soft (bulk Young's moduli of the PDMS in the ∼MPa range) and for small Laplace pressures. In light of applications such as traction-force microscopy, where localized displacements of a soft surface are translated into the corresponding forces acting on the material, the elastocapillary levelling on soft substrates might be an ideal model system to quantitatively study surface deformations in soft materials with precisely controlled pressure fields.

ACKNOWLEDGMENTS

The authors acknowledge S. Herminghaus, J. Snoeijer, A. Pandey, H. Stone, M. Brinkmann, C. Mailliet, P. Damman, K. Dalnoki-Veress, A. Jagota, and J. McGraw for interesting discussions. The German Research Foundation (DFG) is acknowledged for financial support under Grant No. BA 3406/2. V.B. acknowledges financial support from École Normale Supérieure. T.S. acknowledges financial support from the Global Station for Soft Matter, a project of Global Institution for Collaborative Research and Education at Hokkaido University. C.-Y.H. (elasticity modelling) acknowledges financial support from the U.S. Department of Energy, Office of Basic Energy Sciences, Division of Materials Sciences and Engineering under Award No. DE-FG02-07ER46463, and from the Michelin-ESPCI Paris Chair. O.B. acknowledges financial support from the Joliot ESPCI Paris Chair and the Total-ESPCI Paris Chair.

[1] J. M. Skotheim and L. Mahadevan, Soft Lubrication, Phys. Rev. Lett. **92**, 245509 (2004).

[2] T. Salez and L. Mahadevan, Elastohydrodynamics of a sliding, spinning and sedimenting cylinder near a soft wall, J. Fluid Mech. **779**, 181 (2015).

[3] B. Saintyves, T. Jules, T. Salez, and L. Mahadevan, Self-sustained lift and low friction via soft lubrication, Proc. Natl. Acad. Sci. USA **113**, 5847 (2016).
[4] R. Trouilloud, T. S. Yu, A. E. Hosoi, and E. Lauga, Soft Swimming: Exploiting Deformable Interfaces for Low Reynolds Number Locomotion, Phys. Rev. Lett. **101**, 048102 (2008).
[5] E. M. Purcell, Life at low reynolds number, Am. J. Phys **45**, 3 (1977).
[6] C. W. McCutchen, Lubrication of and by articular cartilage, in *Cartilage: Biomedical Aspects*, Vol. 3 (Academic Press, New York, 1983), pp. 87–107.
[7] D. J. Coyle, Forward roll coating with deformable rolls: a simple one-dimensional elastohydrodynamic model, Chem. Eng. Sci. **43**, 2673 (1988).
[8] B Roman and J Bico, Elasto-capillarity: deforming an elastic structure with a liquid droplet, J. Phys.: Condens. Matter **22** 493101 (2010).
[9] B. Andreotti, O. Bäumchen, F. Boulogne, K. E. Daniels, E. R. Dufresne, H. Perrin, T. Salez, J. H. Snoeijer, and R. W. Style, Solid capillarity: when and how does surface tension deform soft solids? Soft Matter **12**, 2993 (2016).
[10] R. W. Style, A. Jagota, C.-Y. Hui, and E. R. Dufresne, Elastocapillarity: Surface tension and the mechanics of soft solids, Annu. Rev. Condens. Matter Phys. **8**, 99 (2016).
[11] C. Py, P. Reverdy, L. Doppler, J. Bico, B. Roman, and C. N. Baroud, Capillary Origami: Spontaneous Wrapping of a Droplet with an Elastic Sheet, Phys. Rev. Lett. **98**, 156103 (2007).
[12] A. Antkowiak, B. Audoly, C. Josserand, S. Neukirch, and M. Rivetti, Instant fabrication and selection of folded structures using drop impact, Proc. Natl. Acad. Sci. USA **108**, 10400 (2011).
[13] C. Duprat, S. Protiere, A. Y. Beebe, and H. A. Stone, Wetting of flexible fibre arrays, Nature (London) **482**, 510 (2012).
[14] N. Nadermann, C.-Y. Hui, and A. Jagota, Solid surface tension measured by a liquid drop under a solid film, Proc. Natl. Acad. Sci. USA **110**, 10541 (2013).
[15] R. D. Schulman and K. Dalnoki-Veress, Liquid Droplets on a Highly Deformable Membrane, Phys. Rev. Lett. **115**, 206101 (2015).
[16] J. D. Paulsen, V. Demery, C. D. Santangleo, T. P. Russell, B. Davidovitch, and N. Menon, Optimal wrapping of liquid droplets with ultrathin sheets, Nat. Mater. **14**, 1206 (2015).
[17] H. Elettro, S. Neukirch, F. Vollrath, and A. Antkowiak, In-drop capillary spooling of spider capture thread inspires hybrid fibers with mixed solid-liquid mechanical properties, Proc. Natl. Acad. Sci. USA **113**, 6143 (2016).
[18] R. D. Schulman, A. Porat, K. Charlesworth, A. Fortais, T. Salez, E. Raphaël, and K. Dalnoki-Veress, Elastocapillary bending of microfibers around liquid droplets, Soft Matter **13**, 720 (2017).
[19] G. R. Lester, Contact angles of liquids at deformable solid surfaces, J. Colloid Sci. **16**, 315 (1961).
[20] R. Pericet-Cámara, A. Best, H.-J. Butt, and E. Bonaccurso, Effect of capillary pressure and surface tension on the deformation of elastic surfaces by sessile liquid microdrops: An experimental investigation, Langmuir **24**, 10565 (2008).
[21] E. R. Jerison, Y. Xu, L. A. Wilen, and E. R. Dufresne, Deformation of an Elastic Substrate by a Three-Phase Contact Line, Phys. Rev. Lett. **106**, 186103 (2011).
[22] A. Marchand, S. Das, J. H. Snoeijer, and B. Andreotti, Contact Angles on a Soft Solid: from Young's Law to Neumann's Law, Phys. Rev. Lett. **109**, 236101 (2012).
[23] L. Limat, Straight contact lines on a soft, incompressible solid, Eur. Phys. J. E **35**, 1 (2012).
[24] R. W. Style, R. Boltyanskiy, Y. Che, J. S. Wettlaufer, L. A. Wilen, and E. R. Dufresne, Universal Deformation of Soft Substrates Near a Contact Line and the Direct Measurement of Solid Surface Stresses, Phys. Rev. Lett. **110**, 066103 (2013).
[25] L. A. Lubbers, J. H. Weijs, L. Botto, S. Das, B. Andreotti, and J. H. Snoeijer, Drops on soft solids: free energy and double transition of contact angles, J. Fluid Mech. **747**, R1 (2014).
[26] R. W. Style, Y. Che, S. J. Park, B. M. Weon, J. H. Je, C. Hyland, G. K. German, M. P. Power, L. A. Wilen, J. S. Wettlaufer, and E. R. Dufresne, Patterning droplets with durotaxis, Proc. Natl. Acad. Sci. USA **110**, 12541 (2013).
[27] S. Karpitschka, S. Das, M. van Gorcum, H. Perrin, B. Andreotti, and J. H. Snoeijer, Droplets move over viscoelastic substrates by surfing a ridge, Nat. Commun. **6** 7891 (2015).

[28] S. Karpitschka, A. Pandey, L. A. Lubbers, J. H. Weijs, L. Botto, S. Das, B. Andreotti, and J. H. Snoeijer, Liquid drops attract or repel by the inverted cheerios effect, Proc. Natl. Acad. Sci. USA **113**, 7403 (2016).
[29] J. D. McGraw, N. M. Jago, and K. Dalnoki-Veress, Capillary levelling as a probe of thin film polymer rheology, Soft Matter **7**, 7832 (2011).
[30] J. Teisseire, A. Revaux, M. Foresti, and E. Barthel, Confinement and flow dynamics in thin polymer films for nanoimprint lithography, Appl. Phys. Lett. **98**, 013106 (2011).
[31] J. D. McGraw, T. Salez, O. Bäumchen, E. Raphaël, and K. Dalnoki-Veress, Self-Similarity and Energy Dissipation in Stepped Polymer Films, Phys. Rev. Lett. **109**, 128303 (2012).
[32] O. Bäumchen, M. Benzaquen, T. Salez, J. D. McGraw, M. Backholm, P. Fowler, E. Raphaël, and K. Dalnoki-Veress, Relaxation and intermediate asymptotics of a rectangular trench in a viscous film, Phys. Rev. E **88**, 035001 (2013).
[33] M. Backholm, M. Benzaquen, T. Salez, E. Raphaël, and K. Dalnoki-Veress, Capillary levelling of a cylindrical hole in a viscous film, Soft Matter **10**, 2550 (2014).
[34] M. Ilton, M. M. P. Couchman, C. Gerbelot, M. Benzaquen, P. D. Fowler, H. A. Stone, E. Raphaël, K. Dalnoki-Veress, and T. Salez, Capillary Levelling of Freestanding Liquid Nanofilms, Phys. Rev. Lett. **117**, 167801 (2016).
[35] E. Rognin, S. Landis, and L. Davoust, Viscosity measurements of thin polymer films from reflow of spatially modulated nanoimprinted patterns, Phys. Rev. E **84**, 041805 (2011).
[36] J. D. McGraw, T. Salez, O. Bäumchen, E. Raphaël, and K. Dalnoki-Veress, Capillary leveling of stepped films with inhomogeneous molecular mobility, Soft Matter **9**, 8297 (2013).
[37] A. Oron, S. H. Davis, and S. G. Bankoff, Long-scale evolution of thin liquid films, Rev. Mod. Phys. **69**, 931 (1997).
[38] T. Salez, J. D. McGraw, S. L. Cormier, O. Bäumchen, K. Dalnoki-Veress, and E. Raphaël, Numerical solutions of thin-film equations for polymer flows, Eur. Phys. J. E **35**, 114 (2012).
[39] T. Salez, J. D. McGraw, O. Bäumchen, K. Dalnoki-Veress, and E. Raphaël, Capillary-driven flow induced by a stepped perturbation atop a viscous film, Phys. Fluids **24**, 102111 (2012).
[40] M. Benzaquen, T. Salez, and E. Raphaël, Intermediate asymptotics of the capillary-driven thin film equation, Eur. Phys. J. E **36**, 82 (2013).
[41] I. Tanis, H. Meyer, T. Salez, E. Raphaël, A. C. Maggs, and J. Baschnagel, Molecular dynamics simulation of the capillary leveling of viscoelastic polymer films, J. Chem. Phys. **146**, 203327 (2017).
[42] X. Q. Brown, K. Ookawa, and J. Y. Wong, Evaluation of polydimethylsiloxane scaffolds with physiologically-relevant elastic moduli: interplay of substrate mechanics and surface chemistry effects on vascular smooth muscle cell response, Biomaterials **26**, 3123 (2005).
[43] A. Hemmerle, M. Schröter, and L. Goehring, A cohesive granular material with tunable elasticity, Sci. Rep. **6**, 35650 (2016).
[44] See Supplemental Material at http://link.aps.org/supplemental/10.1103/PhysRevFluids.2.094001 for further details on the theoretical model, a comparison between lubrication and full-Stokes models for the liquid part, and an additional experiment with a small step atop a thick liquid base film (the ensemble being placed on the soft foundation).
[45] J. Brandrup, E. H. Immergut, E. A Grulke, A. Abe, and D. R. Bloch, *Polymer Handbook* (Wiley, New York, 1989), Vol. 7.

Appendix C

Fractional brownian motion

This worked has been done in collaboration with Kay J. Wiese.

C.1 Introduction

The fractional brownian motion generalises standard brownian motion, it is a gaussian stationary process. This process, unlike standard brownian motion, is non-Markovian, self-similar with respect to a parameter $H \in [0, 1]$, the value $H = 1/2$ corresponds to the Markovian case of the standard brownian motion. In this study, we will compute the first passage time of a drifted fractional brownian motion. In order to compute its first passage time, we will use perturbation theory for the fractional brownian motion[113, 114]. But first, let us motivate the reason for investigating the properties of this process. The log-Brownian model for the movement of share price is widely used in mathematical finance but empirically this model is incorrect in many ways. Various alternative have been proposed to capture differences, for example the Lévy flight to capture price jumps or the fractional Brownian motion which displays time dependence between returns. The presence of autocorrelation and memory in financial stock returns has been a long discussed subject, at least as soon as 1963 (10 years before the Black & Scholes formula) by Mandelbrot [115], wherein the property of long memory of volatility is observed: large changes tend to be followed by large changes, of either sign, and small changes tend to be followed by small changes. While returns r_t themselves tend to be uncorrelated, squared returns r_t^2 show a positive and slowly decaying autocorrelation function: $\mathrm{corr}(r_t^2, r_{t+\tau}^2) > 0$ for τ ranging from a few minutes to a several weeks [116]. This is a well known fact both in academic research as well as on trading floors, that lead to the adoption of auto-regressive models for predicting volatility, and the manifestation of this phenomenon is often priced in the market, e.g. in the volatility futures products. The Fractional Brownian Motion (fBM) was introduced in 1968 by Mandelbrot and van Ness [117], as a generalization of the classical Brownian Motion, whereby the increments of the process can be serially correlated. What initially motivated the creation of such a process was the property of stationarity and self affinity of increments of a random function, as described by Man-

delbrot [115], as well as self-similarity. In such a process, which is also almost surely continuous and non differentiable [117, 115], the arrival of information has a lasting effect on the series, the process is non Markovian, and the whole trajectory impacts the forecast of the evolution. We place ourselves in a continuous market [118], where the evolution of a stock is simulated by a process of a similar form to the classical Geometric Brownian Motion. Let's suppose furthermore that rates, dividends and funding spreads are set to zero. In such a market, the stock can be described by the following SDE:

$$\mathrm{d}S_t = \mu S_t \mathrm{d}t + \sigma S_t \diamondsuit \mathrm{d}B_t^H \tag{C.1}$$

corresponding to a solution of the form:

$$S_t = S_0 e^{\mu t - \frac{1}{2}\sigma^2 t^{2H} + \sigma B_t^H} \tag{C.2}$$

where μ is the historical equity premium associated to the stock, σ is the constant volatility of the asset returns, B_t^H is a fBM with a Hurst coefficient of H. The fBM not being a semi-martingale [119] (except for $H = 0.5$), Ito calculus cannot be used, this SDE requires a choice for the stochastic integration calculus, which are historically either Wick-based integration (denoted here by $\diamondsuit$), or Stratonovitch (path-wise) integration described in details in [120], which have very different properties. Furthermore, Wick's approach can only be used in the persistant case ($H > 0.5$), whereas for anti-persistant cases, the S-transform method [121], can be used as an extension. The usage of such a model has long been criticized in financial mathematics, as arbitrage strategies can be found in most parameterisations (see [122, 123] for the definition or such arbitrages in fractional Bachelier and fractional Black & Scholes models), therefore leading to market incompleteness. It has been also found [119, 120] that straightforward application of these integration theories on self-financed portfolio equations led to inconsistencies in results. Indeed, Stratonovitch integration implies clairvoyance of the investors when constructing their portfolios (by evaluating the integrand midpoint on every infinitesimal interval), leading to a degenerated form of the option price, without any random character - the option is equal to its discounted intrinsic value. This fact is well known in Physics, where on some applications (e.g. financial mathematics), the choice of integration is more than a simple calculus convention, but needs to match economical meaning. Later on, it was proven by Cheridito [123] that the existence of a minimal period of time - be it arbitrarily small - between two consecutive transactions (which theoretically ensures that there are other transactions in between) excludes the feasibility of such strategies, as they relied on continuously adjusted replicating portfolio. In other words, this assumption states that no investors can trade continuously as fast as the market. However, this restriction - which can be considered realistic - still implies the non-uniqueness of a risk neutral measure, as the dynamic hedging argument breaks down, and a discretionary choice would have to be made, for example based on an risk utility based approach [120]. The approach we are going to use here, is the one described by Rostek [120]. We will remind the framework below.

C.2 Equilibrium based approach for valuation with expectation

Giving up on continuous tradability, and unicity of Risk Neutral measure, the most natural approach is using risk preferences, wherein the market has to satisfy some equilibrium conditions. Assuming risk-neutral investors, taking advantage of all the information of the past, will lead to an expression of the price under the form of a certain conditional expectation, allowing to deal with path-dependent payoffs as well. The main object of interest will be the fBM conditioned on all or partial information of the past:

$$\hat{B}^H_{t,T} = \mathbb{E}\left[B^H_T | \mathcal{F}^H_t\right] \tag{C.3}$$

where $\mathcal{F}^H_t = \sigma(B^H_s, s \leq t)$ is the σ-field generated by all paths terminating at time t. Is is a random variable itself, the projection of B^H_T on the space described above. Nuzman and Poor expressed the conditional fBM in a convenient form [124]:

$$\hat{B}^H_{t,T} = \mathbb{E}\left[B^H_T | \mathcal{F}^H_t\right] = B^H_t + (T-t)^{H+\frac{1}{2}} \int_{-\infty}^{t} g(T,t,s)ds \tag{C.4}$$

where

$$g(T,t,s) = \frac{\sin(\pi(H-\frac{1}{2}))(B^H_s - B^H_t)}{\pi(t-s)^{H+\frac{1}{2}}(T-s)} \tag{C.5}$$

This representation proves that the conditional fBM remains normal, and consists in two parts, the first being the current value of the process, and the second being an (random) adjustment accounting for the historical evolution of the process. It leads them to compute the present value of a contingent claim (here, a call option) in the form:

$$C_H(t,T,K) = E\left[(S_T - K)^+ | \mathcal{F}^H_t\right] \tag{C.6}$$

where the expectation has to be taken under a measure of our choice, which leads to forced assumptions on the risk preferences of the investors. In (see [120]), a certain (intuitive) assumption on the pricing measure leads to a Black & Scholes type formula for the price of a Call (and similarly for a Put) under this setting:

$$c_{t,h} = S_t\phi(d_{1,h}) - Ke^{-r(T-t)}\phi(d_{2,h}) \tag{C.7}$$

with,

$$d_{1/2,h} = \frac{\ln\left(\frac{S_t}{K}\right) + r(T-t) \pm \frac{\sigma^2}{2}\rho_h(T-t)^{2h}}{\sigma\sqrt{\rho_h}(T-t)^h} \tag{C.8}$$

and

$$\rho_h = \frac{\sin(\pi(h-1/2))\Gamma(3/2-h)^2}{\pi(h-1/2)\Gamma(2-2h)} \tag{C.9}$$

whereas as mentioned above, careless application of a delta hedging led to a similarly appealing closed form for the option price (see [125]):

$$c_{t,h} = S_t\phi(d_{1,h}^{NEC}) - Ke^{-r(T-t)}\phi(d_{2,h}^{NEC}) \tag{C.10}$$

with,

$$d_{1/2,h} = \frac{\ln(\frac{S_t}{K}) + r(T-t) \pm \frac{\sigma^2}{2}(T^{2H} - t^{2h})}{\sigma\sqrt{T^{2H} - t^{2h}}} \tag{C.11}$$

which looses the property of being stationary: for everything else equal, two options of the same maturity, struck at two different times, will have two different prices, forcing the user to model the line of time in absolute rather than relative values. While this assumption of non-continuous trading strategies does not seem to be too restrictive when thinking of real financial markets, it entails one problem: Though having excluded arbitrage, the traditional no arbitrage option pricing approaches continue to fail, as now the possibility of a continuous adjustment of the replicating portfolio is no longer given. Dynamical hedging and replication methods are no longer available to derive prices of derivative assets. The consequence to which one may come, is to abstain from this kind of setting [126].

C.3 One-touch call option pricing

A One-touch call option is an option paying 1to the buyer, when the stock price reaches a certain barrier K (lower than the spot for a binary put, higher than the spot for a binary call):

$$c_t(K,T) = \mathrm{E}\left[e^{-r(\tau-t)}|\mathcal{F}_t^H\right] , \tag{C.12}$$

$$\tau = \mathrm{argmin}_{t\in[0,T]}\{S_t > K\} \tag{C.13}$$

These contracts fall into the class of once exotic now vanilla, due to their popularity. They are particularly useful for hedging other contracts that also have a payoff that depends on whether or not the specified level is reached. Since they are American-style options we must decide as part of the solution when to exercise optimally. They would clearly be exercised as soon as the level is reached. This makes an otherwise complicated free boundary problem into a rather simple fixed boundary problem. For a one-touch call, we compute the previous expectancy using the first passage time distribution of a drifted brownian motion or fractional brownian motion.

C.3.1 Brownian environment

The first passage time distribution of a drifted Brownian motion $\mu t + \sigma B_t$ starting in 0 and reaching a barrier m reads:

$$G(m,t) = \frac{|m|}{\sqrt{2\pi}\sigma t^{3/2}} e^{-\frac{(m-\mu t)^2}{2\sigma^2 t}} \tag{C.14}$$

the solution of this problem is:

$$c_t = \frac{S_t}{K} N(d_1) + \left(\frac{K}{S_t}\right)^{\frac{2\mu}{\sigma^2}} N(d_2) \tag{C.15}$$

where K is the strike price, S_t the price at time t, T the maturity, μ the risk-free rate, σ the volatility and $N(x) = \frac{1}{\sqrt{2\pi}} \int_{-\infty}^{x} e^{-\frac{u^2}{2}} \mathrm{d}u$. With:

$$d_1 = \frac{\ln\left(\frac{S_t}{K}\right) + \left(\mu + \frac{\sigma^2}{2}\right)(T-t)}{\sigma\sqrt{T-t}}, \tag{C.16}$$

$$d_2 = \frac{\ln\left(\frac{S_t}{K}\right) - \left(\mu + \frac{\sigma^2}{2}\right)(T-t)}{\sigma\sqrt{T-t}}. \tag{C.17}$$

C.3.2 Fractional Brownian environment

Using the distribution $G_h(m,t)$, one can say that:

$$c_t = \int_t^T e^{-\mu(\tau-t)} G_h\left(\ln\left(\frac{S_t}{K}\right), \tau\right) \mathrm{d}\tau \tag{C.18}$$

We use below a perturbative approach on the path integral of fBm to provide a perturbative closed formula for the first passage time distribution for the drifted process G_h C.93 and the price of an American digital option of a fBm underlying. But first let recall the basics of a first passage time distribution.

C.3.3 Diffusion and first passage time of a standard brownian motion

The random walk and its continuum limit of diffusion called the Brownian motion is very important in statistical physics. The Brownian motion of a particle immersed in a liquid is the motion resulting on the multiple collision of small particles on the tracked particle.

Discrete case

We start by considering the random walk case on a 1D lattice. At each step the particle can moves of a fixed distance to the left with the probability p and to the right with the probability $1-p$. Consider a sequence of independent random variables ϵ_i that assume

values $+1$ and -1 with probability $\frac{1}{2}$. In a random walk model, the particle takes unit step up or down at regular intervals, and the position of the particle at the nth step is given by:

$$S_n = \epsilon_1 + ... + \epsilon_n \ , \ S_0 = 0 \ . \tag{C.19}$$

We set $N_{z,n}$ to be the number of path starting from the origin to z after n steps. We note p the number of positive occurence in the random walk and q the negative ones. Therefore $n = p + q$ and $z = p - q$. The number of path is simply the combination of positive occurence within n random draw.[127]

$$N_{z,n} = \binom{n}{p} = \binom{n}{\frac{n+z}{2}} \ . \tag{C.20}$$

The probability for the particle of being at z after n step is then:

$$P(S_n = z) = 2^{-n} \binom{n}{\frac{n+z}{2}} \ . \tag{C.21}$$

One can check that for $z \to \infty$, by using the De Moivre-Laplace Theorem, we obtain the gaussian approximation of the random walk:

$$P(S_n = z) \sim \sqrt{\frac{2}{\pi n}} \exp\left(-\frac{z^2}{2n}\right) \ . \tag{C.22}$$

The probability to return at the origin after $2n$ steps (this probability is zero for an odd number of steps) is simply:

$$a_{2n} = P(S_n = 0) = 2^{-n} \binom{2n}{n} \sim \frac{1}{\sqrt{2\pi n}} \ . \tag{C.23}$$

Among all the returns to the origin, the first return time has a specific behaviour. A first return at the origin occurs after $2n$ steps, if $S_1 \neq 0 ... S_{2n-1} \neq 0 \ , S_{2n} = 0$. The probability of this event is b_{2n}. The probability a_{2n} and b_{2n} are linked. Indeed, the visit at the origin after $2n$ step can be either the first one or the first one occurs earlier after $2k < 2n$ steps with the probability v_{2k} and therefore it returns to the origin after $2(n-k)$ steps with the probability $a_{2(n-k)}$ and this $\forall k \in [\![1, n]\!]$. Eventually we obtain the following relation:

$$a_{2n} = \sum_{k=1}^{n} b_{2k} a_{2(n-k)} \ . \tag{C.24}$$

We define the moment generating function of a sequence $\{a_{2n}\}$ and compute it in this case:

$$A(t) = 1 + \sum_{n=1}^{\infty} a_{2n} t^{2n} = \sum_{n=0}^{\infty} (-1)^n \binom{-1/2}{n} t^n = \frac{1}{\sqrt{1-t^2}} \ , \tag{C.25}$$

Applying this transformation to the equation Eq.[C.24], one gets:

$$B(t) = 1 - \frac{1}{A(t)} = 1 - \sqrt{1-t^2} \ , \tag{C.26}$$

from this relation one can compute the $2n$th moment:

$$b_{2n} = \frac{1}{2n-1} u_{2n} = \frac{2^{-n}}{2n-1} \binom{2n}{n} \sim \frac{1}{\sqrt{4\pi n^3}} \tag{C.27}$$

The law of the n_i for $i > 1$ is given by the sequence $\{b_{2n}\}$. The probability q_n for the random walk of reaching for the first time z of its path after n steps starting from the origin is called a first passage time, the sequence $\{q_n\}$ gives the distribution of n_1. By the reflection principle we know that:

$$P(S_n = z + k) = P(S_n = z + k | n_1 \leq n) = P(S_n = z - k | n_1 \leq n) \ , \tag{C.28}$$

therefore:

$$P(n_1 \leq n) = \sum_{k=-\infty}^{+\infty} P(S_n = z + k | n_1 \leq n) = P(S_n = z) + 2P(S_n > z) \ . \tag{C.29}$$

Eventually one gets :

$$q_n(z) = \frac{1}{2} \left(P(S_{n-1} = z - 1) - P(S_{n-1} = z + 1) \right) \ , \tag{C.30}$$

or,

$$q_n(z) = 2^{-n} \frac{z}{n} \binom{n}{\frac{n+z}{2}} \ , \tag{C.31}$$

with $q_n = 0$ if $\frac{n+z}{2}$ is odd. At large z, we recover the distribution of first passage time for the brownian motion:

$$q_n \sim \sqrt{\frac{2}{\pi n^3}} z \exp(-\frac{z^2}{2n}) \ . \tag{C.32}$$

The moment generating function also reads:

$$N_1(t) = \left(\frac{1 - \sqrt{1-t^2}}{t} \right)^z \tag{C.33}$$

Continuous limit

In the continuous limit of diffusion, the first passage density is computed directly from the probability of going from z to z_1 during a time t without touching the interfaces. This density is noted $P_c\left(z_1, t | z, 0\right)$ and verifies the diffusion equation with absorbing boundary

conditions at $z = 0$:

$$\partial_t P_c = D\Delta P_c \ , \tag{C.34}$$

$$P_c(z = 0) = 0 \tag{C.35}$$

if we integrate $P_c\,(z_1, t|z, 0)$ from its starting position in $z = h$ to $z = 0$ where it is absorbed one gets the survival probability $S(t)$ to the boundary $z = 0$. The first passage time distribution is simply:

$$f(t) = -\frac{\mathrm{d}S(t)}{\mathrm{d}t} \tag{C.36}$$

One can solve the diffusion equation and gets:

$$f(t) = \frac{h}{\sqrt{2\pi t^3}} \exp\left(-\frac{h^2}{2t}\right) \tag{C.37}$$

This expression is similar to the discrete case (C.32).

C.3.4 Fractional brownian motion

In the following the fractional brownian motion–fBm–is considered with a linear and non linear drift:

$$z_t = x_t + \mu t + \nu t^{2H}, \tag{C.38}$$

where x_t is the standard fBm, with a mean value:

$$\langle x_t \rangle = 0 \ , \tag{C.39}$$

and a two-time correlation:

$$\langle x_{t_1} x_{t_2} \rangle = |t_1|^{2H} + |t_2|^{2H} - |t_1 - t_2|^{2H} \ . \tag{C.40}$$

The process x_t is a gaussian process for all values of H, and only markovian for $H = 1/2$. Therefore one can expand the action of this gaussian process around $H = 1/2$. The statistical weight of a path x_t is proportional to $\exp(-S[x])$ where $S[x]$ is the action given by:

$$S[x] = \int_0^t \mathrm{d}t_1 \int_0^t \mathrm{d}t_2 \frac{1}{2} x(t_1) G(t_1, t_2) x(t_2) \ , \tag{C.41}$$

the kernel of the action $G(t_1, t_2)$ is related to the autocorrelation function via:

$$G^{-1}(t_1, t_2) = \langle x(t_1) x(t_2) \rangle. \tag{C.42}$$

In order to have the perturbative action of the fractional brownian motion we have first to expand the autocorrelation function (Eq.C.40) around $H = 1/2$.

$$G^{-1}(t_1, t_2) = [G^{(0)}]^{-1} + \epsilon K(t_1, t_2) + o(\epsilon) \ , \tag{C.43}$$

with

$$[G^{(0)}]^{-1} = 2\min(t_1, t_2) \ , \tag{C.44}$$

and

$$K(t_1, t_2) = 2\left(t_1 \ln(t_1) + t_2 \ln(t_2) - |t_1 - t_2| \ln|t_1 - t_2|\right) \ . \tag{C.45}$$

Inverting Eq.C.43, one gets:

$$G = G^{(0)} + \epsilon G^{(1)} + o(\epsilon) \ , \tag{C.46}$$

That leads directly to:

$$G^1 = -G^{(0)}[G^{(0)}]^{-1} G^{(0)} \ , \tag{C.47}$$

where

$$\int_0^\infty \mathrm{d}t G^{(0)}(t_1, t)[G^{(0)}]^{-1}(t, t_2) = \delta(t_1 - t_2) \ , \tag{C.48}$$

therefore one can check that:

$$G^{(0)}(t_1, t_2) = -\frac{1}{2}\delta''(t_1 - t_2) \ , \tag{C.49}$$

and

$$G^1(t_1, t_2) = -\frac{1}{2}\int_0^t \mathrm{d}t' \int_0^t \mathrm{d}t'' \delta'(t_1 - t') \frac{1}{|t' - t''|} \delta'(t_2 - t'') - 2(1 + \ln(\tau))[G^{(0)}]^{-1}(t_1, t_2) \ , \tag{C.50}$$

with τ considered as the time discretization limit of the path integral.
The action of the standard fBm is therefore:

$$S[x] = \int_0^T \mathrm{d}t \frac{\dot{x}(t)^2}{4D_\epsilon} - \frac{\epsilon}{2}\int_{0<t_1<t_2<T} \frac{\dot{x}(t_1)\dot{x}(t_2)}{|t_1 - t_2|} \mathrm{d}t_1 \mathrm{d}t_2 \ . \tag{C.51}$$

There is a short time cutoff in the last integral $|t_1 - t_2| > \tau$, this cutoff appear in the diffusion coefficient.

$$D_\epsilon = 2H\tau^{2H-1}. \tag{C.52}$$

C.4 Path integral of the drifted fBm

The path integral formulation for the first passage time is:

$$G\left(m,T\right)=\lim_{x_0\to 0}\frac{1}{x_0}\int_{z(0)=m}^{x(T)=x_0}\mathcal{D}\left[z\right]\exp\left(-S\left[z\right]\right). \tag{C.53}$$

Replacing $\dot{x}(t)$ by :

$$\dot{x}(t)=\dot{z}(t)-\mu-\nu-2\epsilon\nu(1+\ln(t))\ , \tag{C.54}$$

A short-distance cutoff $|t_1-t_2|>\tau$ in the last integral is implicit, reflected in the diffusion constant. Inserting the definition of the action, we arrive at:

$$\begin{aligned}\mathcal{S}[z] &= \int_0^T \mathrm{d}t\,\frac{\dot{z}_t^2}{4D_\epsilon}+\frac{\epsilon}{2}\dot{z}_t\left[(\mu+\nu)\ln\left(\frac{t(T-t)}{\tau^2}\right)-2\nu\ln(t)\right]-\frac{\epsilon}{2}\int_\tau^T \mathrm{d}t_2\int_0^{t_2-\tau}\mathrm{d}t_1\frac{\dot{z}_{t_1}\dot{z}_{t_2}}{|t_1-t_2|}\\ &\quad -\frac{z_T-z_0}{2D_\epsilon}\Big[\mu+\nu(1+2\epsilon)\Big]+\frac{1}{4}T(\mu+\nu)^2+\frac{1}{2}T\epsilon\left(\nu^2-\mu^2\right)\ln(T)+\ \mathcal{O}(\epsilon^2)\ .\end{aligned} \tag{C.55}$$

Let us do some checks. In absence of boundaries, we know the exact free propagator,

$$P(0,z,T)=\frac{1}{2\sqrt{\pi}T^H}\mathrm{e}^{-\frac{(z-\mu T-\nu T^{2H})^2}{4T^{2H}}}=\frac{1}{2\sqrt{\pi}T^H}\exp\left(\frac{z^2}{4T^{2H}}-\frac{z}{2}\Big[\nu+\mu T^{-2\epsilon}\Big]+\ \frac{T^{2H}}{4}\Big[\nu+\mu T^{-2\epsilon}\Big]\right)\ . \tag{C.56}$$

Now since the above formalism has variables $\dot{z}$ only, the term $\sim z^2$ is given by the drift-free perturbation theory. We can further check that if we replace in the action $\dot{z}(t)$ by its "classical trajectory", i.e. $\dot{z}(t)\to[z(T)-z(0)]/T$, then both the normalisation and the drift term agree with the exact propagator. Let us specify to the two cases of interest: For a fBm with *linear drift* as given in Eq. (C.38) with $\nu=0$, we have

$$\mathcal{S}^{\mathrm{ld}}[z] = \int_0^T \mathrm{d}t\,\frac{\dot{z}_t^2}{4D_\epsilon}-\frac{\mu}{2D_\epsilon}(z_T-z_0)+\frac{T^{1-2\epsilon}}{4}\mu^2-\frac{\epsilon}{2}\int_{0<t_1<t_2<T}\frac{\dot{z}(t_1)\dot{z}(t_2)}{|t_1-t_2|} \tag{C.57}$$

$$+\frac{\epsilon\mu}{2}\int_0^T \mathrm{d}t\,\dot{z}(t)\ln\left(\frac{[T-t]t}{\tau^2}\right) \tag{C.58}$$

For a fBm with *non-linear drift* as given in Eq. (C.38) with $\mu=0$, we have

$$\mathcal{S}^{\mathrm{nld}}[z] = \int_0^T \mathrm{d}t\,\frac{\dot{z}_t^2}{4D_\epsilon}-\frac{\nu}{2}(z_T-z_0)+\frac{T^{1+2\epsilon}}{4}\nu^2-\frac{\epsilon}{2}\int_{0<t_1<t_2<T}\frac{\dot{z}(t_1)\dot{z}(t_2)}{|t_1-t_2|} \tag{C.59}$$

$$+\frac{\epsilon\nu}{2}\int_0^T \mathrm{d}t\,\dot{z}(t)\ln\left(\frac{[T-t]}{t}\right) \tag{C.60}$$

Note the appearance of the diffusion constant in the "bias" (Girsanov) term $z_T - z_0$ for a linear drift, and its absence for a non-linear drift. In the following we define

$$\alpha := \mu - \nu \ , \qquad \beta := \mu + \nu \tag{C.61}$$

This comes with the last terms grouped as

$$\mathcal{S}^{\alpha}[z] := \epsilon\alpha \int_0^T \mathrm{d}t\, \dot{z}(t) \ln\left(\frac{t}{\tau}\right) \tag{C.62}$$

$$\mathcal{S}^{\beta}[z] := \epsilon\beta \int_0^T \mathrm{d}t\, \dot{z}(t) \ln\left(\frac{T-t}{\tau}\right) \tag{C.63}$$

C.5 First passage time distribution

C.5.1 General formulas and order 0

At the first order in ϵ for G,

$$\begin{aligned} G(m,T) := \ & \exp\left(-\frac{m}{2}\left(\frac{\mu}{D_\epsilon}+\nu\right) - \frac{T}{4}\left(\mu^2 T^{-2\epsilon} + \nu^2 T^{2\epsilon}\right)\right) \\ & \times \left\{ G_0(m,T) + 2\epsilon\Big[G_1(m,T) - \alpha\, G_{2\alpha}(m,T) - \beta G_{2\beta}(m,T)\Big]\right\} \end{aligned} \tag{C.64}$$

The order-0 contribution is

$$\tilde{G}_0(m,s) = \mathrm{e}^{-m\sqrt{s}} \ , \qquad G_0(m,t) = \frac{m e^{-\frac{m^2}{4t}}}{2\sqrt{\pi} t^{3/2}} \tag{C.65}$$

C.5.2 Order ϵ, first diagram

The first diagram in Laplace is obtained from the one without drift.

$$\begin{aligned} \tilde{G}_1(m,s) &= \frac{1}{x_0}\int_0^\Lambda \mathrm{d}y \int_{x_1>0}\int_{x_2>0} \tilde{P}_+(m,x_1,s)\partial_{x_1}\tilde{P}_+(x_1,x_2,s+y)\partial_{x_2}\tilde{P}_+(x_2,x_0,s) \\ &= \int_0^\Lambda \mathrm{d}y \frac{\sqrt{s}\left(e^{-m\sqrt{s}}\left(my - 2\sqrt{s+y}\right) + 2\sqrt{s+y}e^{-m\sqrt{s+y}}\right)}{2y^2} \\ &= \frac{1}{2}\Bigg[e^{m\sqrt{s}}\left(m\sqrt{s}+1\right)\mathrm{Ei}\left(-2m\sqrt{s}\right) + m\sqrt{s}e^{-m\sqrt{s}}\left[\ln\left(\frac{m^2}{2\tau}\right) - 1\right] \qquad \text{(C.66)} \\ &\quad + e^{-m\sqrt{s}}\left[\ln\left(\frac{\tau^2}{2x_0^4}\right) - 3\gamma_{\mathrm{E}} + 4\right] \\ &\quad - e^{-m\sqrt{s}}\left(m\sqrt{s}+1\right)\ln\left(m\sqrt{s}\right)\Bigg] \qquad \text{(C.67)} \end{aligned}$$

For the inverse Laplace transform we find

$$\begin{aligned} G_1(m,t) &= \frac{me^{-\frac{m^2}{4t}}\mathcal{I}\left(\frac{m}{\sqrt{2t}}\right)}{4\sqrt{\pi}t^{3/2}} + \frac{me^{-\frac{m^2}{4t}}}{8\sqrt{\pi}t^{5/2}}\Big[\left(m^2-4t\right)\ln\left(\Lambda m^2\right) + (2\gamma_{\mathrm{E}}-1)m^2 + 2t\ln(\Lambda t) - 2(1+3\gamma_{\mathrm{E}})t\Big] \\ &= G_0(m,t)\left[\frac{1}{2}\mathcal{I}\left(\frac{m}{\sqrt{2t}}\right) + \left(\frac{m^2}{4t}-1\right)\ln\left(\Lambda m^2\right)\right. \qquad \text{(C.68)} \\ &\quad \left. + \frac{(2\gamma_{\mathrm{E}}-1)m^2 + 2(3-7\gamma_{\mathrm{E}})t}{4t} + \frac{1}{2}\ln\left(\frac{t}{\Lambda x_0^4}\right)\right] \qquad \text{(C.69)} \end{aligned}$$

The special function $\mathcal{I}$ appearing in this expression is

$$\mathcal{I}(z) = \frac{z^4}{6}\,{}_2F_2\left(1,1;\frac{5}{2},3;\frac{z^2}{2}\right) + \pi(1-z^2)\,\mathrm{erfi}\left(\frac{z}{\sqrt{2}}\right) - 3z^2 + \sqrt{2\pi}e^{\frac{z^2}{2}}z + 2 \qquad \text{(C.70)}$$

Using $\Lambda = e^{-\gamma_{\mathrm{E}}}/\tau$, Eq. (C.68) can be rewritten as

$$\begin{aligned} G_1(z) &= \frac{1}{2}G_0(z)\Big\{\mathcal{I}(z) + \left(z^2-1\right)\left[\ln\left(\frac{t}{\tau}\right)-1\right] + \ln\left(\frac{\tau^2}{4x_0^4z^4}\right) \qquad \text{(C.71)} \\ &\quad + z^2\Big[\ln\left(2z^2\right)+\gamma_{\mathrm{E}}\Big] - 4\gamma_{\mathrm{E}} + 2\Big\} \qquad \text{(C.72)} \\ z &:= \frac{m}{\sqrt{2t}} \qquad \text{(C.73)} \end{aligned}$$

If we take the limit of $x_0 \to 0$ first, then the result changes:

$$\tilde{G}_1^{x_0\to 0}(m,s) = \tilde{G}_1(m,s) + \mathrm{e}^{-m\sqrt{s}}\Big[\ln\left(\Lambda x_0^2\right) + 2(\gamma_{\mathrm{E}}-1)\Big] \qquad \text{(C.74)}$$

This change is proportional to the order-0 contribution, thus should disappear in a change of normalisation.

C.5.3 Order ϵ, diagram $G_{2\alpha}$

We use that

$$\ln\left(\frac{t}{\tau}\right) = \int_0^\infty \frac{\mathrm{d}y}{y}\left[\mathrm{e}^{-\tau y} - \mathrm{e}^{-ty}\right] \qquad \text{(C.75)}$$

This gives

$$\begin{aligned}\tilde{G}_{2a}(m,s) &= \lim_{x_0\to 0}\frac{1}{x_0}\int_0^\Lambda \frac{\mathrm{d}y}{y}\int_{x_1>0}\Big[\tilde{P}_+(m,x_1,s)\mathrm{e}^{-\tau y}-\tilde{P}_+(m,x_1,s+y)\Big]\partial_{x_1}\tilde{P}_+(x_1,x_0,s)\\ &= \int_0^{\Lambda/s}\mathrm{d}y\left[\frac{e^{-m\sqrt{s}}}{\sqrt{s}y^2}-\frac{e^{-m\sqrt{s}\sqrt{y+1}}}{\sqrt{s}y^2}-\frac{me^{-m\sqrt{s}-s\tau y}}{2y}\right]\\ &= \frac{1}{4}me^{-m\sqrt{s}}\left[2e^{2m\sqrt{s}}\mathrm{Ei}\left(-2m\sqrt{s}\right)+\ln\left(\frac{4s\tau^2}{m^2}\right)+2\right]+O(\Lambda^{-1}) \qquad \text{(C.76)}\end{aligned}$$

We checked that the y integrand is convergent, at least as $1/y^2$ for large y, and finite for $y\to 0$, thus x_0 is not necessary as an UV cutoff, and the y-integral is finite.

$$G_{2\alpha}(m,t)=\frac{e^{-\frac{z^2}{2}}z^2\left[\mathcal{I}(z)-2\right]}{2\sqrt{\pi t}(1-z^2)}+\frac{z\,\mathrm{erfc}(\frac{z}{\sqrt{2}})}{\sqrt{2t}\,(z^2-1)}-\frac{e^{-\frac{z^2}{2}}z^2\Big[\ln\Big(\frac{2tz^2}{\tau}\Big)+\gamma_{\mathrm{E}}-1\Big]}{2\sqrt{\pi t}} \qquad \text{(C.77)}$$

C.5.4 Order ϵ, diagram $G_{2\beta}$

$$\begin{aligned}\tilde{G}_{2\beta}(m,s) &= \lim_{x_0\to 0}\frac{1}{x_0}\int_0^\Lambda\frac{\mathrm{d}y}{y}\int_{x_1>0}\tilde{P}_+(m,x_1,s)\,\partial_{x_1}\Big[\tilde{P}_+(x_1,x_0,s)\mathrm{e}^{-\tau y}-\tilde{P}_+(x_1,x_0,s+y)\Big]\\ &= \int_0^\infty\mathrm{d}y\left[\frac{\sqrt{y+1}e^{-m\sqrt{s}}}{\sqrt{s}y^2}-\frac{\sqrt{y+1}e^{-m\sqrt{s}\sqrt{y+1}}}{\sqrt{s}y^2}-\frac{me^{-m\sqrt{s}-s\tau y}}{2y}\right]\\ &= \frac{e^{-m\sqrt{s}}\left(-m\sqrt{s}\ln\left(\frac{m^2}{4s\tau^2}\right)+\ln\left(m^2s\right)+2m\sqrt{s}+2\gamma_{\mathrm{E}}+\ln(4)\right)}{4\sqrt{s}} \qquad \text{(C.78)}\\ &\quad -\frac{e^{m\sqrt{s}}\left(m\sqrt{s}+1\right)\mathrm{Ei}\left(-2m\sqrt{s}\right)}{2\sqrt{s}} \qquad \text{(C.79)}\end{aligned}$$

We checked that the y integrand is convergent, at least as $1/y^{3/2}$ for large y, and finite for $y\to 0$, thus x_0 or Λ are not necessary as an UV cutoff, and the y-integral is finite. Doing the inverse Laplace transform, we get with z defined in Eq. (C.73)

$$G_{2\beta}(m,t)=\frac{e^{-\frac{z^2}{2}}\left[\mathcal{I}(z)-2\right]}{2\sqrt{\pi t}\,(1-z^2)}+\frac{z\,\mathrm{erfc}(\frac{z}{\sqrt{2}})}{\sqrt{2t}\,(z^2-1)}+\frac{e^{-\frac{z^2}{2}}z^2\left[1-\ln(\frac{t}{\tau})\right]}{2\sqrt{\pi t}} \qquad \text{(C.80)}$$

C.5.5 Results

In this part we resume all the results computed above.

$$G_0(m,t) = \frac{e^{-\frac{z^2}{2}}z}{\sqrt{2\pi}t} \tag{C.81}$$

$$G_1(m,t) = \frac{e^{-\frac{z^2}{2}}z}{2\sqrt{2\pi}t}\Bigg[\mathcal{I}(z)+\left(z^2-1\right)\left(\ln\left(\frac{t}{\tau}\right)-1\right)+\ln\left(\frac{\tau^2}{4x_0^4z^4}\right) \tag{C.82}$$

$$+z^2\left(\ln\left(2z^2\right)+\gamma_{\rm E}\right)-4\gamma_{\rm E}+2\Bigg] \tag{C.83}$$

$$G_{2\mu}(m,t) = \frac{1}{2}\Big[G_{2\alpha}(m,t)+G_{2\beta}(m,t)\Big] = -\frac{e^{-\frac{z^2}{2}}\left(z^2+1\right)\left[\mathcal{I}(z)-2\right]}{4\sqrt{\pi t}\left(z^2-1\right)} \tag{C.84}$$

$$+\frac{z\,\mathrm{erfc}(\frac{z}{\sqrt{2}})}{\sqrt{2t}(z^2-1)}-\frac{e^{-\frac{z^2}{2}}z^2\left[\ln\left(\frac{2t^2z^2}{\tau^2}\right)+\gamma_{\rm E}-2\right]}{4\sqrt{\pi t}} \tag{C.85}$$

$$G_{2\nu}(m,t) = \frac{1}{2}\Big[G_{2\beta}(m,t)-G_{2\alpha}(m,t)\Big] = \frac{e^{-\frac{z^2}{2}}\left[\mathcal{I}(z)-2\right]}{4\sqrt{\pi t}} \tag{C.86}$$

$$+\frac{e^{-\frac{z^2}{2}}z^2\left[\ln(2z^2)+\gamma_{\rm E}\right]}{4\sqrt{\pi t}} \tag{C.87}$$

They group together as

$$G(m,T) := \exp\left(-\frac{m}{2}\left(\frac{\mu}{D_\epsilon}+\nu\right)-\frac{T}{4}\left(\mu^2T^{-2\epsilon}+\nu^2T^{2\epsilon}\right)\right) \times\Big\{G_0(m,T)+2\epsilon\Big[G_1(m,T)-\mu\,G_{2\mu}(m,T)-\nu G_{2\nu}(m,T)\Big]\Big\} \tag{C.88}$$

It should be extrapolated as

$$G(m,T) := \exp\left(-\frac{m}{2}\left(\frac{\mu}{D_\epsilon}+\nu\right)-\frac{T}{4}\left(\mu^2T^{-2\epsilon}+\nu^2T^{2\epsilon}\right)\right)G_0(m,T) \times\exp\left(2\epsilon\frac{G_1(m,T)-\mu\,G_{2\mu}(m,T)-\nu G_{2\nu}(m,T)}{G_0(m,T)}\right) \tag{C.89}$$

This expression is

C.6 History dependence

In this part we will compute the first passage time distribution conditional to the knowledge of a part of the previous trajectory, the fact that fBm is non-Markovian, the memory of the past trajectory will modify the distribution.

C.6.1 Additional terms in the action

Suppose that we know the trajectory from time $t = -h$ to $t = 0$. This adds an additional term $\delta\mathcal{S}_\mathrm{h}$ (h for "history") to the action

$$\delta\mathcal{S}_\mathrm{h}[x] = -\frac{\epsilon}{2}\int_{-h}^{0}\mathrm{d}t'\int_{0}^{T}\mathrm{d}t\,\frac{\dot{x}(t')\dot{x}(t)}{|t-t'|} + \mathcal{O}(\epsilon^2)\ . \tag{C.90}$$

We did not write the term where both times are smaller than 0, since this term will drop with the normalisation: After all, the propagator for $T \to 0$ must reduce to a δ-distribution. It yields to

$$\delta\mathcal{S}_\mathrm{h}[x] = \frac{\epsilon}{2}(\mu+\nu)\int_{-h}^{0}\mathrm{d}t'\ln\left(1-\frac{T}{t'}\right)\dot{x}(t') - \frac{\epsilon}{2}\int_{-h}^{0}\mathrm{d}t'\int_{0}^{T}\mathrm{d}t\,\frac{\dot{x}(t')\dot{z}(t)}{|t-t'|} + \mathcal{O}(\epsilon^2)\ . \tag{C.91}$$

C.6.2 Translation into perturbative expansion

The last term in (C.91) leads to the following additional terms, as compared to (C.64):

$$\begin{aligned} G_\mathrm{h}(m,T) &= G(m,T)\times\exp\left(-\frac{\epsilon}{2}(\mu+\nu)\int_{-h}^{0}\mathrm{d}t'\ln\left(1-\frac{T}{t'}\right)\dot{x}(t')\right) && \text{(C.92)}\\ &\quad\times\exp\Big(\epsilon\,\delta G_\mathrm{h}(m,T)/G_0(m,T)\Big) && \text{(C.93)}\end{aligned}$$

The first term changes the normalisation. The second term is a diagram similar to G_{2a} and G_{2b}:

$$\begin{aligned} \delta\tilde{G}_\mathrm{h}(m,s) &= \int_0^\Lambda \mathrm{d}y\,\tilde{g}(y)\,\tilde{P}_+(m,x_1,s+y)\,\partial_{x_1}\tilde{P}_+(x_1,x_0,s) && \text{(C.94)}\\ \tilde{g}(y) &:= \int_{-h}^{0}\mathrm{d}t'\mathrm{e}^{yt'}\dot{x}(t') && \text{(C.95)}\end{aligned}$$

We have introduced an UV cutoff Λ out of precaution. Some examples for $\tilde{g}(y)$

$$\dot{x}(t') = 1 \qquad \Leftrightarrow \qquad \tilde{g}(y) = \frac{1-e^{-hy}}{y} \tag{C.96}$$

$$\begin{aligned} &\exp\left(-\frac{\epsilon}{2}(\mu+\nu)\int_{-h}^{0}\mathrm{d}t'\ln\left(1-\frac{T}{t'}\right)\dot{x}(t')\right) && \text{(C.97)}\\ &= \exp\left(-\frac{1}{2}\epsilon(\mu+\nu)\left[h\ln\left(\frac{T}{h}\right)+(h+T)\ln\left(\frac{h+T}{T}\right)\right]\right) && \text{(C.98)}\end{aligned}$$

We find

$$\begin{aligned}\delta\tilde{G}_{\rm h}(m,s) &= \sqrt{s}\int_0^{\Lambda s}\frac{{\rm d}y}{y^2}\left[e^{-m\sqrt{s}-hy}-e^{-m\sqrt{s+y}-hy}-e^{-m\sqrt{s}}+e^{-m\sqrt{s+y}}\right]\\ &= \sqrt{s}\int_0^{\Lambda s}\frac{{\rm d}y}{y^2}\left[e^{-m\sqrt{s+y}}-e^{-m\sqrt{s}}\right]\left[1-{\rm e}^{-hy}\right] \qquad \text{(C.99)}\end{aligned}$$

We can compute this integral as follows:

$$\frac{1}{\sqrt{s}} = \int_0^\infty {\rm d}t\,{\rm e}^{-ts}\frac{1}{\sqrt{t\pi}} = {\rm LT}_{t\to s}\frac{1}{\sqrt{t\pi}} \qquad \text{(C.100)}$$

$${\rm LT}^{-1}_{s\to t}\int_0^{\Lambda s}\frac{{\rm d}y}{y^2}\left[e^{-m\sqrt{s+y}}-e^{-m\sqrt{s}}\right]\left[1-{\rm e}^{-hy}\right]$$

$$= -\int_0^\infty {\rm d}y\,\frac{m\left(1-e^{-hy}\right)e^{-\frac{m^2}{4t}}\left(1-e^{-ty}\right)}{2\sqrt{\pi}t^{3/2}y^2} \qquad \text{(C.101)}$$

$$= -\frac{me^{-\frac{m^2}{4t}}\left[h\ln(\frac{h}{h+t})+t\ln(\frac{t}{h+t})\right]}{2\sqrt{\pi}t^{3/2}} \qquad \text{(C.102)}$$

$$\delta G_{\rm h}(m,t) = \int_0^t {\rm d}t'\,\frac{1}{\sqrt{(t-t')\pi}}\partial_{t'}\frac{me^{-\frac{m^2}{4t'}}\left[h\ln(\frac{h}{h+t'})+t'\ln(\frac{t'}{h+t'})\right]}{2\sqrt{\pi}t'^{3/2}} \qquad \text{(C.103)}$$

This can be rewritten as

$$\begin{aligned}\delta G_{\rm h}(m,t) &= \frac{e^{-\frac{m^2}{4t}}}{8\pi t^3}\int_0^\infty {\rm d}x\frac{e^{-\frac{m^2x}{4t}}}{\sqrt{x}}\Big[m\Big(h(x+1)\left(6t-m^2(x+1)\right) \qquad \text{(C.104)}\\ &\quad -m^2t(x+1)+2t^2\Big)\ln\left(\frac{hx+h+t}{t}\right)\\ &\quad +hm(x+1)\left(m^2(x+1)-6t\right)\ln\left(\frac{h(x+1)}{t}\right)\Big] \qquad \text{(C.105)}\end{aligned}$$

Using that $\ln(x)=\partial_a x^a|_{a=0}$, this integral can indeed be done. In a first step, one obtains ${}_1F_1$ hypergeometric functions. They are derived w.r.t. their first and second argument. Studying their defining series expansion, taking their derivative, and resuming, we finally obtain:

$$\delta G_{\mathrm{h}}(m,t) = \frac{e^{-\frac{z^2}{2}}}{2\sqrt{\pi t}}\Bigg[\chi\left(3-z^2\right)z^2\,{}_2F_2\left(1,1;\frac{3}{2},2;\frac{z^2}{2}\right) \tag{C.106}$$

$$+\frac{(\chi+1)z^2\left(-3\chi+(\chi+1)z^2-1\right)\,{}_2F_2\left(1,1;\frac{3}{2},2;\frac{z^2(\chi+1)}{2\chi}\right)}{\chi}$$

$$+\chi\,{}_2F_2\left(1,1;-\frac{1}{2},2;\frac{z^2}{2}\right)-(\chi+1)\,{}_2F_2\left(1,1;-\frac{1}{2},2;\frac{z^2(\chi+1)}{2\chi}\right)$$

$$-\chi\left(3-2z^2\right)\,{}_2F_2\left(1,1;\frac{1}{2},2;\frac{z^2}{2}\right) \tag{C.107}$$

$$-\frac{(\chi+1)\left((2\chi+1)z^2-3\chi\right)\,{}_2F_2\left(1,1;\frac{1}{2},2;\frac{z^2(\chi+1)}{2\chi}\right)}{\chi}$$

$$+\pi\chi\left(z^2-1\right)\operatorname{erfi}\left(\frac{z}{\sqrt{2}}\right)-\pi\left((\chi+1)z^2-\chi\right)\operatorname{erfi}\left(\frac{\sqrt{\frac{1}{\chi}+1}z}{\sqrt{2}}\right)$$

$$-\sqrt{2\pi}e^{\frac{z^2}{2}}z\left(\sqrt{\chi(\chi+1)}e^{\frac{z^2}{2\chi}}-\chi\right)+z^2\ln\left(\frac{2z^2}{\chi}\right)+\gamma_{\mathrm{E}}z^2-2\Bigg] \tag{C.108}$$

The variables are

$$\chi = \frac{h}{t} \tag{C.109}$$

$$z = \frac{m}{\sqrt{2t}} \tag{C.110}$$

$$G_0(m,t) = \frac{e^{-\frac{z^2}{2}}z}{\sqrt{2\pi}t} \tag{C.111}$$

$$\begin{aligned}\frac{\delta G_{\rm h}(m,t)}{G_0(m,t)} &= \frac{t}{m}\Bigg[\chi\left(3-z^2\right)z^2\,{}_2F_2\left(1,1;\frac{3}{2},2;\frac{z^2}{2}\right) \\ &+\frac{(\chi+1)z^2\left(-3\chi+(\chi+1)z^2-1\right)\,{}_2F_2\left(1,1;\frac{3}{2},2;\frac{z^2(\chi+1)}{2\chi}\right)}{\chi} \\ &+\chi\,{}_2F_2\left(1,1;-\frac{1}{2},2;\frac{z^2}{2}\right)-(\chi+1)\,{}_2F_2\left(1,1;-\frac{1}{2},2;\frac{z^2(\chi+1)}{2\chi}\right) \\ &-\chi\left(3-2z^2\right)\,{}_2F_2\left(1,1;\frac{1}{2},2;\frac{z^2}{2}\right)-\frac{(\chi+1)\left((2\chi+1)z^2-3\chi\right)\,{}_2F_2\left(1,1;\frac{1}{2},2;\frac{z^2(\chi+1)}{2\chi}\right)}{\chi} \\ &+\pi\chi\left(z^2-1\right)\mathrm{erfi}\left(\frac{z}{\sqrt{2}}\right)+\pi\left((\chi+1)z^2-\chi\right)\mathrm{erfi}\left(\frac{\sqrt{\frac{1}{\chi}+1}z}{\sqrt{2}}\right) \\ &-\sqrt{2\pi}e^{\frac{z^2}{2}}z\left(\sqrt{\chi(\chi+1)}e^{\frac{z^2}{2\chi}}-\chi\right)+z^2\ln\left(\frac{2z^2}{\chi}\right)+\gamma_{\rm E}z^2-2\Bigg]\end{aligned} \tag{C.112}$$

For $\chi\to\infty$, this gives

$$\begin{aligned}\frac{\delta G_{\rm h}(m,t)}{G_0(m,t)} &= \frac{t}{m}\Bigg[-z^2\,{}_2F_2\left(1,1;\frac{1}{2},2;\frac{z^2}{2}\right)+\left(z^4-z^2\right)\,{}_2F_2\left(1,1;\frac{3}{2},2;\frac{z^2}{2}\right) \\ &\quad +z^2\left(-\pi\mathrm{erfi}\left(\frac{z}{\sqrt{2}}\right)+\ln\left(\frac{2z^2}{\chi}\right)+\gamma_{\rm E}-1\right)+\sqrt{2\pi}e^{\frac{z^2}{2}}z\Bigg]+\mathcal{O}(1/\chi) \\ &= \frac{m}{2}\Bigg[-\,{}_2F_2\left(1,1;\frac{1}{2},2;\frac{z^2}{2}\right)+\left(z^2-1\right)\,{}_2F_2\left(1,1;\frac{3}{2},2;\frac{z^2}{2}\right) \\ &\quad -\pi\,\mathrm{erfi}\left(\frac{z}{\sqrt{2}}\right)+\ln\left(\frac{2z^2}{\chi}\right)+\gamma_{\rm E}-1+\frac{\sqrt{2\pi}}{z}e^{\frac{z^2}{2}}\Bigg]+\mathcal{O}(1/\chi)\end{aligned} \tag{C.114}$$

Now suppose we had a sharp up- or down-rise at time $t=-h$. Then (up to the amplitude)

$$\dot{x}(t)=\delta(t+h) \qquad \Leftrightarrow \qquad \tilde{g}(y)=e^{-hy} \tag{C.115}$$

We find

$$\delta\tilde{G}_{\rm h}(m,s) = \sqrt{s}\int_0^{\Lambda s}\frac{{\rm d}y}{y}\left[e^{-m\sqrt{s+y}}-e^{-m\sqrt{s}}\right]{\rm e}^{-hy} \tag{C.116}$$

This integral being nasty, we can also take the h derivative of our former result. We can take one more derivative, to obtain

$$\dot{x}(t) = \delta'(t+h) \qquad \Leftrightarrow \qquad \tilde{g}(y) = -y\, e^{-hy} \tag{C.117}$$

This yields

$$\delta\tilde{G}_{\mathrm{h}}(m,s) \;=\; -\sqrt{s}\int_0^{\Lambda s} \mathrm{d}y\, \left[e^{-m\sqrt{s+y}} - e^{-m\sqrt{s}}\right] \mathrm{e}^{-hy} \tag{C.118}$$

$$\delta G_{\mathrm{h}}(m,t) \;=\; \frac{e^{-\frac{z^2}{2}} z^2}{2\sqrt{\pi}t^{5/2}\chi(\chi+1)} - \frac{z\, e^{\frac{z^2}{2\chi}}\, \mathrm{erfc}\left(\frac{\sqrt{\chi+1}}{\sqrt{2\chi}}z\right)}{2\sqrt{2}t^{5/2}\chi^{3/2}(\chi+1)^{3/2}} \tag{C.119}$$

Bibliography

[1] T. H. Havelock, The propagation of groups of waves in dispersive media, with application to waves on water produced by a traveling disturbance. *Proc. R. Soc. A*, 1908, vol. 95, page 354.

[2] L. Landau, Em lifshitz, fluid mechanics. *Course of Theoretical Physics*, 1959, vol. 6.

[3] H. Lamb. *Hydrodynamics*. Cambridge university press, 1932.

[4] R. P. Feynman, R. B. Leighton and M. Sands. *The Feynman lectures on physics, vol. 2: Mainly electromagnetism and matter*. Addison-Wesley, 1979.

[5] J. J. Stoker. *Water waves: The mathematical theory with applications*, vol. 36. John Wiley & Sons, 2011.

[6] R. S. Johnson. *A modern introduction to the mathematical theory of water waves*, vol. 19. Cambridge university press, 1997.

[7] A. Chepelianskii, F. Chevy and E. Raphael, Capillary-gravity waves generated by a slow moving object. *Physical review letters*, 2008, vol. 100, numéro 7, page 074504.

[8] J. V. Wehausen and E. V. Laitone. Surface waves. *In Fluid Dynamics/Strömungsmechanik*, pages 446–778. Springer, 1960.

[9] F. Closa, A. Chepelianskii and E. Raphael, Capillary-gravity waves generated by a sudden object motion. *Physics of Fluids*, 2010, vol. 22, numéro 5, page 052107.

[10] M. Le Merrer, C. Clanet, D. Quéré, É. Raphaël and F. Chevy, Wave drag on floating bodies. *Proceedings of the National Academy of Sciences*, 2011, vol. 108, numéro 37, pages 15064–15068.

[11] E. Părău and F. Dias, Nonlinear effects in the response of a floating ice plate to a moving load. *Journal of Fluid Mechanics*, 2002, vol. 460, pages 281–305.

[12] E. I. Părău and J.-M. Vanden-Broeck, Three-dimensional waves beneath an ice sheet due to a steadily moving pressure. *Philosophical Transactions of the Royal Society of London A: Mathematical, Physical and Engineering Sciences*, 2011, vol. 369, numéro 1947, pages 2973–2988.

[13] C. DUPRAT, J. M. ARISTOFF and H. A. STONE, Dynamics of elastocapillary rise. *Journal of Fluid Mechanics*, 2011, vol. 679, pages 641–654.

[14] D. Pihler-Puzović, P. ILLIEN, M. HEIL and A. JUEL, Suppression of complex fingerlike patterns at the interface between air and a viscous fluid by elastic membranes. *Phys. Rev. Lett.*, 2012, vol. 108, page 074502, DOI : 10.1103/PhysRevLett.108.074502, [URL direct].

[15] T. T. AL-HOUSSEINY, I. C. CHRISTOV and H. A. STONE, Two-phase fluid displacement and interfacial instabilities under elastic membranes. *Physical review letters*, 2013, vol. 111, numéro 3, page 034502.

[16] H. A. STONE and C. DUPRAT, Model problems coupling elastic boundaries and viscous flows. *Fluid-Structure Interactions in Low-Reynolds-Number Flows*, 2015, page 78.

[17] J. SEIWERT, D. QUÉRÉ and C. CLANET, Flexible scraping of viscous fluids. *Journal of Fluid Mechanics*, 2013, vol. 715, pages 424–435.

[18] J. M. SKOTHEIM and L. MAHADEVAN, Soft lubrication. *Phys. Rev. Lett.*, 2004, vol. 92, page 245509.

[19] J. H. SNOEIJER, J. EGGERS and C. H. VENNER, Similarity theory of lubricated hertzian contacts. *Physics of Fluids*, 2013, vol. 25, numéro 10, page 101705.

[20] T. SALEZ and L. MAHADEVAN, Elastohydrodynamics of a sliding, spinning and sedimenting cylinder near a soft wall. *Journal of Fluid Mechanics*, 2015, vol. 779, page 181.

[21] K. SEKIMOTO and L. LEIBLER, A mechanism for shear thickening of polymer-bearing surfaces: elasto-hydrodynamic coupling. *Europhys. Lett.*, 1993, vol. 23, page 113.

[22] A. PANDEY, S. KARPITSCHKA, C. H. VENNER and J. H. SNOEIJER, Lubrication of soft viscoelastic solids. *Journal of Fluid Mechanics*, 2016, vol. 799, pages 433–447, DOI : 10.1017/jfm.2016.375, [URL direct].

[23] B. SAINTYVES, T. JULES, T. SALEZ and L. MAHADEVAN, Self-sustained lift and low friction via soft lubrication. *Proceedings of the National Academy of Sciences of the USA*, 2016, vol. 113, page 5847.

[24] A. CARLSON, S. MANDRE and L. MAHADEVAN, Elastohydrodynamics of contact in adherent sheets. *arXiv preprint arXiv:1508.06234*, 2015.

[25] A. CARLSON and L. MAHADEVAN, Similarity and singularity in adhesive elastohydrodynamic touchdown. *Physics of Fluids (1994-present)*, 2016, vol. 28, numéro 1, page 011702.

[26] M. G. BLYTH, E. I. PĂRĂU and J.-M. VANDEN-BROECK, Hydroelastic waves on fluid sheets. *Journal of Fluid Mechanics*, 2011, vol. 689, pages 541–551.

[27] P. Guyenne and E. I. Părău, Forced and unforced flexural-gravity solitary waves. *Procedia IUTAM*, 2014, vol. 11, pages 44–57.

[28] R. Villey, E. Martinot, C. Cottin-Bizonne, M. Phaner-Goutorbe, L. Léger, F. Restagno and E. Charlaix, Effect of surface elasticity on the rheology of nanometric liquids. *Phys. Rev. Lett.*, 2013, vol. 111, page 215701, DOI : 10.1103/PhysRevLett.111.215701, [URL direct].

[29] L. D. Landau and E. Lifshitz, Theory of elasticity, vol. 7. *Course of Theoretical Physics*, 1986, vol. 3, page 109.

[30] J. Flitton and J. King, Moving-boundary and fixed-domain problems for a sixth-order thin-film equation. *European Journal of Applied Mathematics*, 2004, vol. 15, numéro 06, pages 713–754.

[31] R. Ledesma-Alonso, M. Benzaquen, T. Salez and E. Raphaël, Wake and wave resistance on viscous thin films. *Journal of Fluid Mechanics*, 2016, vol. 792, pages 829–849.

[32] Havelock, The theory of wave resistance. *Proceedings of the Royal Society of London. Series A, Containing Papers of a Mathematical and Physical Character*, 1932, vol. 138, numéro 835, pages 339–348.

[33] E. Raphaël and P.-G. De Gennes, Capillary gravity waves caused by a moving disturbance: wave resistance. *Physical Review E*, 1996, vol. 53, numéro 4, page 3448.

[34] R. B. Suter, Spider locomotion on the water surface: biomechanics and diversity. *Journal of Arachnology*, 2013, vol. 41, numéro 2, pages 93–101.

[35] M. W. Denny, Paradox lost: answers and questions about walking on water. *Journal of experimental biology*, 2004, vol. 207, numéro 10, pages 1601–1606.

[36] J. W. Bush and D. L. Hu, Walking on water: Biolocomotion at the interface. *Annu. Rev. Fluid Mech.*, 2006, vol. 38, pages 339–369.

[37] S. Vogel. *Comparative biomechanics: life's physical world*. Princeton University Press, 2013.

[38] J. S. Koh, E. Yang, G. P. Jung, S. P. Jung, J. H. Son, S. I. Lee and K. J. Cho, Jumping on water: Surface tension–dominated jumping of water striders and robotic insects. *Science*, 2015, vol. 349, numéro 6247, pages 517–521.

[39] V. M. Ortega-Jimenez, L. von Rabenau and R. Dudley, Escape jumping by three age-classes of water striders from smooth, wavy and bubbling water surfaces. *Journal of experimental biology*, 2017, vol. 220, numéro 15, pages 2809–2815.

[40] D. L. Hu, M. Prakash, B. Chan and J. W. M. Bush, Water-walking devices. *Experiments in Fluids*, 2007, vol. 43, pages 769–778.

[41] J. YUAN and S. K. CHO, Bio-inspired micro/mini propulsion at air-water interface: A review. *Journal of mechanical science and technology*, 2012, vol. 26, numéro 12, pages 3761–3768.

[42] E. YANG, J. H. SON, P. G. JABLONSKI and H. Y. KIM, Water striders adjust leg movement speed to optimize takeoff velocity for their morphology. *Nature communications*, 2016, vol. 7, numéro 13698.

[43] K. YANG, G. LIU, J. YAN, T. WANG, X. ZHANG and J. ZHAO, A water-walking robot mimicking the jumping abilities of water striders. *Bioinspiration and biomimetics*, 2016, vol. 11, numéro 6, page 066002.

[44] E. RAPHAËL and P.-G. de GENNES, Capillary gravity waves caused by a moving disturbance: wave resistance. *Phys. Rev. E*, 1996, vol. **53**, numéro 4, page 3448.

[45] D. L. HU, B. CHAN and J. W. BUSH, The hydrodynamics of water strider locomotion. *Nature*, 2003, vol. 424, numéro 6949, page 663.

[46] O. BÜHLER, Impulsive fluid forcing and water strider locomotion. *Journal of Fluid Mechanics*, 2007, vol. 573, pages 211–236.

[47] P. GAO and J. J. FENG, A numerical investigation of the propulsion of water walkers. *Journal of Fluid Mechanics*, 2011, vol. 668, pages 363–383.

[48] J. ZHENG, K. YU, J. ZHANG, J. WANG and C. LI, Modeling of the propulsion hydrodynamics for the water strider locomotion on water surface. *Procedia Engineering*, 2015, vol. 126, pages 280–284.

[49] D. L. HU and J. W. BUSH, The hydrodynamics of water-walking arthropods. *Journal of Fluid Mechanics*, 2010, vol. 644, pages 5–33.

[50] A. RINOSHIKA, Vortical dynamics in the wake of water strider locomotion. *Journal of Visualization*, 2011, vol. 15, pages 145–153.

[51] R. S. WILCOX, Communication by surface waves. *Journal of Comparative Physiology A: Neuroethology, Sensory, Neural, and Behavioral Physiology*, 1972, vol. 80, numéro 3, pages 255–266.

[52] K. WIESE, The mechanoreceptive system of prey localization innotonecta. *Journal of Comparative Physiology A: Neuroethology, Sensory, Neural, and Behavioral Physiology*, 1974, vol. 92, numéro 3, pages 317–325.

[53] H. BLECKMANN, M. BORCHARDT, P. HORN and P. GÖRNER, Stimulus discrimination and wave source localization in fishing spiders (dolomedes triton and d. okefinokensis). *Journal of Comparative Physiology A: Neuroethology, Sensory, Neural, and Behavioral Physiology*, 1994, vol. 174, numéro 3, pages 305–316.

[54] T. STEINMANN, M. ARUTKIN, P. COCHARD, E. RAPHAËL, J. CASAS and M. BENZAQUEN, Unsteady wave pattern generation by water striders. *Journal of Fluid Mechanics*, 2018, vol. 848, pages 370–387.

[55] H. Lamb. Hydrodynamics, cambridge mathematical library, 1993.

[56] F. Moisy, M. Rabaud and K. Salsac, A synthetic schlieren method for the measurement of the topography of a liquid interface. *Experiments in Fluids*, 2009, vol. 46, numéro 6, page 1021.

[57] J. B. Keller, Gravity waves on ice-covered water. *Journal of Geophysical Research: Oceans*, 1998, vol. 103, numéro C4, pages 7663–7669.

[58] K. Binder and W. Kob. *Glassy materials and disordered solids: An introduction to their statistical mechanics*. World Scientific, 2011.

[59] T. Salez, J. Salez, K. Dalnoki-Veress, E. Raphaël and J. A. Forrest, Cooperative strings and glassy interfaces. *Proceedings of the National Academy of Sciences*, 2015, vol. 112, numéro 27, pages 8227–8231.

[60] M. Arutkin, E. Raphaël, J. A. Forrest and T. Salez, Cooperative strings in glassy nanoparticles. *Soft matter*, 2016, vol. 13, numéro 1, pages 141–146.

[61] C. A. Angell, Formation of glasses from liquids and biopolymers. *Science*, 1995, vol. 267, numéro 5206, pages 1924–1935.

[62] G. Adam and J. H. Gibbs, On the temperature dependence of cooperative relaxation properties in glass-forming liquids. *The journal of chemical physics*, 1965, vol. 43, numéro 1, pages 139–146.

[63] M. H. Cohen and D. Turnbull, Molecular transport in liquids and glasses. *The Journal of Chemical Physics*, 1959, vol. 31, numéro 5, pages 1164–1169.

[64] W. Götze, Recent tests of the mode-coupling theory for glassy dynamics. *Journal of Physics: condensed matter*, 1999, vol. 11, numéro 10A, page A1.

[65] C. Donati, J. F. Douglas, W. Kob, S. J. Plimpton, P. H. Poole and S. C. Glotzer, Stringlike cooperative motion in a supercooled liquid. *Physical review letters*, 1998, vol. 80, numéro 11, page 2338.

[66] B. A. Pazmiño Betancourt, J. F. Douglas and F. W. Starr, String model for the dynamics of glass-forming liquids. *The Journal of chemical physics*, 2014, vol. 140, numéro 20, page 204509.

[67] Z. Zhang, P. J. Yunker, P. Habdas and A. Yodh, Cooperative rearrangement regions and dynamical heterogeneities in colloidal glasses with attractive versus repulsive interactions. *Physical review letters*, 2011, vol. 107, numéro 20, page 208303.

[68] A. S. Keys, A. R. Abate, S. C. Glotzer and D. J. Durian, Measurement of growing dynamical length scales and prediction of the jamming transition in a granular material. *Nature physics*, 2007, vol. 3, numéro 4, page 260.

[69] H. Vogel, The law of the relation between the viscosity of liquids and the temperature. *Phys. Z*, 1921, vol. 22, pages 645–646.

[70] G. S. FULCHER, Analysis of recent measurements of the viscosity of glasses. *Journal of the American Ceramic Society*, 1925, vol. 8, numéro 6, pages 339–355.

[71] G. TAMMANN and W. HESSE, Die abhängigkeit der viscosität von der temperatur bie unterkühlten flüssigkeiten. *Zeitschrift für anorganische und allgemeine Chemie*, 1926, vol. 156, numéro 1, pages 245–257.

[72] E. DONTH, Characteristic length of the glass transition. *Journal of Polymer Science Part B: Polymer Physics*, 1996, vol. 34, numéro 17, pages 2881–2892.

[73] C. L. JACKSON and G. B. MCKENNA, The melting behavior of organic materials confined in porous solids. *The Journal of Chemical Physics*, 1990, vol. 93, numéro 12, pages 9002–9011.

[74] S. FENG, Z. LI, R. LIU, B. MAI, Q. WU, G. LIANG, H. GAO and F. ZHU, Glass transition of polystyrene nanospheres under different confined environments in aqueous dispersions. *Soft Matter*, 2013, vol. 9, numéro 18, pages 4614–4620.

[75] Y. RHARBI, Reduction of the glass transition temperature of confined polystyrene nanoparticles in nanoblends. *Physical Review E*, 2008, vol. 77, numéro 3, page 031806.

[76] C. ZHANG, Y. GUO and R. D. PRIESTLEY, Glass transition temperature of polymer nanoparticles under soft and hard confinement. *Macromolecules*, 2011, vol. 44, numéro 10, pages 4001–4006.

[77] Z. FAKHRAAI and J. FORREST, Measuring the surface dynamics of glassy polymers. *Science*, 2008, vol. 319, numéro 5863, pages 600–604.

[78] M. EDIGER and J. FORREST, Dynamics near free surfaces and the glass transition in thin polymer films: a view to the future. *Macromolecules*, 2013, vol. 47, numéro 2, pages 471–478.

[79] Z. YANG, Y. FUJII, F. K. LEE, C.-H. LAM and O. K. TSUI, Glass transition dynamics and surface layer mobility in unentangled polystyrene films. *Science*, 2010, vol. 328, numéro 5986, pages 1676–1679.

[80] Y. CHAI, T. SALEZ, J. D. MCGRAW, M. BENZAQUEN, K. DALNOKI-VERESS, E. RAPHAËL and J. A. FORREST, A direct quantitative measure of surface mobility in a glassy polymer. *Science*, 2014, vol. 343, numéro 6174, pages 994–999.

[81] H. YOON and G. B. MCKENNA, Substrate effects on glass transition and free surface viscoelasticity of ultrathin polystyrene films. *Macromolecules*, 2014, vol. 47, numéro 24, pages 8808–8818.

[82] J. D. STEVENSON, J. SCHMALIAN and P. G. WOLYNES, The shapes of cooperatively rearranging regions in glass-forming liquids. *Nature Physics*, 2006, vol. 2, numéro 4, pages 268–274.

[83] R. Courant and D. Hilbert. *Methods of mathematical physics*, vol. 1. CUP Archive, 1966.

[84] M. Kac, Can one hear the shape of a drum? *The american mathematical monthly*, 1966, vol. 73, numéro 4, pages 1–23.

[85] D. S. Grebenkov and B.-T. Nguyen, Geometrical structure of laplacian eigenfunctions. *SIAM Review*, 2013, vol. 55, numéro 4, pages 601–667.

[86] J. Forrest, What can we learn about a dynamical length scale in glasses from measurements of surface mobility? *The Journal of chemical physics*, 2013, vol. 139, numéro 8, page 084702.

[87] J. Forrest and K. Dalnoki-Veress, When does a glass transition temperature not signify a glass transition? *ACS Macro Letters*, 2014, vol. 3, numéro 4, pages 310–314.

[88] A. Raegen, M. Massa, J. Forrest and K. Dalnoki-Veress, Effect of atmosphere on reductions in the glass transition of thin polystyrene films. *The European Physical Journal E*, 2008, vol. 27, numéro 4, pages 375–377.

[89] C. B. Roth and J. R. Dutcher, Glass transition and chain mobility in thin polymer films. *Journal of Electroanalytical Chemistry*, 2005, vol. 584, numéro 1, pages 13–22.

[90] H.-S. L. Cole, Beck. *Heat conduction using Green's functions*. Taylor & Francis, 2010.

[91] A. Haji-Sheikh and J. V. Beck, An efficient method of computing eigenvalues in heat conduction. *Numerical Heat Transfer: Part B: Fundamentals*, 2000, vol. 38, numéro 2, pages 133–156.

[92] P. De Gennes, Glass transitions in thin polymer films. *The European Physical Journal E: Soft Matter and Biological Physics*, 2000, vol. 2, numéro 3, pages 201–205.

[93] S. T. Milner and J. E. Lipson, Delayed glassification model for free-surface suppression of t g in polymer glasses. *Macromolecules*, 2010, vol. 43, numéro 23, pages 9865–9873.

[94] J. Lipson and S. Milner, Percolation model of interfacial effects in polymeric glasses. *The European Physical Journal B-Condensed Matter and Complex Systems*, 2009, vol. 72, numéro 1, pages 133–137.

[95] S. F. Edwards, The statistical mechanics of polymers with excluded volume. *Proceedings of the Physical Society*, 1965, vol. 85, numéro 4, page 613.

[96] M. Doi and S. F. Edwards. *The theory of polymer dynamics*, vol. 73. oxford university press, 1988.

[97] P.-G. DE GENNES. *Scaling concepts in polymer physics*. Cornell university press, 1979.

[98] T. KAWAKATSU. *Statistical physics of polymers: an introduction*. Springer Science & Business Media, 2013.

[99] J. A. FORREST and K. DALNOKI-VERESS, The glass transition in thin polymer films. *Advances in Colloid and Interface Science*, 2001, vol. 94, numéro 1, pages 167–195.

[100] J. L. KEDDIE, R. A. JONES and R. A. CORY, Size-dependent depression of the glass transition temperature in polymer films. *EPL (Europhysics Letters)*, 1994, vol. 27, numéro 1, page 59.

[101] K. NGAI, A. RIZOS and D. PLAZEK, Reduction of the glass temperature of thin freely standing polymer films caused by the decrease of the coupling parameter in the coupling model. *Journal of non-crystalline solids*, 1998, vol. 235, pages 435–443.

[102] P. SCHEIDLER, W. KOB and K. BINDER, The relaxation dynamics of a simple glass former confined in a pore. *EPL (Europhysics Letters)*, 2000, vol. 52, numéro 3, page 277.

[103] D. LONG and F. LEQUEUX, Heterogeneous dynamics at the glass transition in van der waals liquids, in the bulk and in thin films. *The European Physical Journal E: Soft Matter and Biological Physics*, 2001, vol. 4, numéro 3, pages 371–387.

[104] S. HERMINGHAUS, K. JACOBS and R. SEEMANN, The glass transition of thin polymer films: some questions, and a possible answer. *The European Physical Journal E*, 2001, vol. 5, numéro 1, pages 531–538.

[105] F. VARNIK, J. BASCHNAGEL and K. BINDER, Reduction of the glass transition temperature in polymer films: A molecular-dynamics study. *Physical Review E*, 2002, vol. 65, numéro 2, page 021507.

[106] J. BASCHNAGEL and F. VARNIK, Computer simulations of supercooled polymer melts in the bulk and in confined geometry. *Journal of Physics: Condensed Matter*, 2005, vol. 17, numéro 32, page R851.

[107] C.-H. LAM and O. K. TSUI, Crossover to surface flow in supercooled unentangled polymer films. *Physical Review E*, 2013, vol. 88, numéro 4, page 042604.

[108] S. MIRIGIAN and K. S. SCHWEIZER. Communication: Slow relaxation, spatial mobility gradients, and vitrification in confined films, 2014.

[109] P. Z. HANAKATA, B. A. PAZMIÑO BETANCOURT, J. F. DOUGLAS and F. W. STARR, A unifying framework to quantify the effects of substrate interactions, stiffness, and roughness on the dynamics of thin supported polymer films. *The Journal of chemical physics*, 2015, vol. 142, numéro 23, page 234907.

[110] G. Barton. *Elements of Green's functions and propagation: potentials, diffusion, and waves*. Oxford University Press, 1989.

[111] P. L. Krapivsky, S. Redner and E. Ben-Naim. *A kinetic view of statistical physics*. Cambridge University Press, 2010.

[112] S. Redner. *A guide to first-passage processes*. Cambridge University Press, 2001.

[113] K. J. Wiese, S. N. Majumdar and A. Rosso, Perturbation theory for fractional brownian motion in presence of absorbing boundaries. *Physical Review E*, 2011, vol. 83, numéro 6, page 061141.

[114] M. Delorme and K. J. Wiese, Perturbative expansion for the maximum of fractional brownian motion. *Physical Review E*, 2016, vol. 94, numéro 1, page 012134.

[115] B. B. Mandelbrot. The variation of certain speculative prices. *In Fractals and scaling in finance*, pages 371–418. Springer, 1997.

[116] R. Cont. Long range dependence in financial markets. *In Fractals in engineering*, pages 159–179. Springer, 2005.

[117] B. B. Mandelbrot and J. W. Van Ness, Fractional brownian motions, fractional noises and applications. *SIAM review*, 1968, vol. 10, numéro 4, pages 422–437.

[118] Y. Hu and B. Øksendal, Fractional white noise calculus and applications to finance. *Infinite dimensional analysis, quantum probability and related topics*, 2003, vol. 6, numéro 01, pages 1–32.

[119] S. Rostek and R. Schöbel, A note on the use of fractional brownian motion for financial modeling. *Economic Modelling*, 2013, vol. 30, pages 30–35.

[120] S. Rostek. Fractional integration calculus. *In Option Pricing in Fractional Brownian Markets*, pages 5–31. Springer, 2009.

[121] C. Bender *et al.*, An s-transform approach to integration with respect to a fractional brownian motion. *Bernoulli*, 2003, vol. 9, numéro 6, pages 955–983.

[122] L. C. G. Rogers, Arbitrage with fractional brownian motion. *Mathematical Finance*, 1997, vol. 7, numéro 1, pages 95–105.

[123] P. Cheridito, Arbitrage in fractional brownian motion models. *Finance and Stochastics*, 2003, vol. 7, numéro 4, pages 533–553.

[124] C. J. Nuzman and H. V. Poor, Linear estimation of self-similar processes via lamperti's transformation. *Journal of Applied Probability*, 2000, vol. 37, numéro 2, pages 429–452.

[125] C. Necula, Option pricing in a fractional brownian motion environment. 2002.

[126] C. Bender, T. Sottinen and E. Valkeila, Arbitrage with fractional brownian motion? 2007.

[127] W. FELLER. *An introduction to probability theory and its applications*, vol. 1. Wiley, New York, 1968.

[128] P. WILMOTT. *Paul Wilmott on quantitative finance*. John Wiley & Sons, 2013.

[129] T. E. DUNCAN and B. PASIK-DUNCAN. Stochastic linear-quadratic control for systems with a fractional brownian motion. *In Decision and Control (CDC), 2010 49th IEEE Conference on*, pages 6163–6168. IEEE, 2010.

Acknowledgments

Ces trois années de thèse furent riches en rencontres et je voudrais ici remercier les personnes impliquées dans cette experience. Je voudrais tout d'abord remercier Anne Tanguy et Isabelle Cantat pour avoir acceptées d'être les rapporteurs de ma thèse et pour leurs nombreuses remarques qui ont permis d'améliorer ce manuscrit. Merci à Jörg Baschnagel d'avoir présidé le jury. Ainsi qu'à Kay Wiese et Christophe Clanet pour avoir acceptés de compléter le jury de la soutenance. Un grand merci à Elie Raphael et Thomas Salez pour avoir acceptés de diriger ma thèse. J' ai beaucoup appris à leurs cotés, à être persévérant devant des problèmes complexes et pour les attaquer du bon angle. Un très grand merci à Michael Benzaquen, Jerôme Casas et Thomas Steinmann avec qui j' ai eu la chance de travailler. Je tiens aussi à remercier chaleureusement James Forrest qui m'a accueilli au Perimeter Institute, où j'ai pu découvrir un lieu exceptionnel dédié à la physique, et avec qui j'ai pu découvrir les mystères de la transition vitreuse. J' ai été amené à travailler avec Kay Wiese que j' aimerais remercier particulièrement, pour tout le temps passé à discuter dans son bureau, et pour la justesse qu' il a montré dans sa manière de me guider à travers une belle aventure scientifique à la recherche du mouvement Brownien fractionnaire et de ses merveilles. Je remercie également mes professeurs de sciences qui ont su éveiller en moi un intérêt pour les sciences, en particulier François Vandenbrouck, dont les cours en prépa m'ont permis d'en arriver là. Finalement je tiens à profiter de cette espace de remerciements qui m'est offert pour redire mon affection aux personnes qui me sont chères. Merci ainsi à tous mes amis parisiens, en particulier Ulysse, Romain et Alexandre pour votre aide précieuse, et votre amitié sincère, Théo pour ton soutien, ta patience, mes amis de toujours Jules, Julien et Gauthier pour toutes ces années. Merci à ma famille, avec un affection particulière pour Arthur et Alice mes extraordinaires frère et soeur.

Maxence Arutkin
Paris, December 5th 2018

Résumé

Cette thèse se divise en deux parties, la première partie aborde la physique des sillages.
Lorsqu'un objet se déplace à la surface d'un liquide des ondes sont générées et rayonnées. Lorsque l'objet se déplace à vitesse constante il résulte le fameux sillage en V de Kelvin qu'on peut observer derrière un bateau. Le rayonnement de ces ondes crée une force s'opposant au mouvement appelée resistance de vague. On établit ici la formule de Havelock de la résistance de vague pour un mouvement quelconque. Le sillage et la résistance de vague sont également étudiés en présence d'un couplage élastohydrodydamique à l'interface. Enfin on termine avec l'étude des vagues générées par une araignée d'eau lors de sa phase de propulsion.
Dans la seconde partie, on propose un modèle de chaines cooperatives en s'inspirant de la loi empirique d'Adam et Gibbs pour la transition vitreuse. Ce modèle nous permet d'étudier des anomalies de transition vitreuse en milieu confiné notamment la réduction de temperature de transition vitreuse dans les nano-films et nanoparticules de polystyrène. Enfin on aborde des calculs de statistiques de chaines polymèriques en milieux confinés et leurs dépendances exactes dans le poids moléculaire.

Mots Clés

Films minces, transition vitreuse, vagues, résistance de vague.

Abstract

This thesis is divided into two parts. In the first part, we study several properties of waves at the surface of a liquid ; in particular the wake generated at the interface by an object modelled by a pressure field. When an object with constant speed moves atop the surface, it generates a wake. The radiation of these waves results in a loss of energy for the operator putting the object in motion, which results in a resultant force opposite to the motion called the wave resistance, calculated by the Havelock formula. In the stationary regime, we propose here a demonstration of the Havelock formula for any movement on the surface. The wake and wave resistance are also studied using elastohydrodynamic coupling at the surface. We then model the waves generated by a water strider during its propulsion phase.
In the second part, we propose a model of cooperative strings inspired by the empirical law of Adam and Gibbs for the glass transition. This model allows us to study glass transition anomalies in a confined environment, in particular the reduction of glass transition temperature in thin films and nanoparticles of polystyrenes. Finally, we consider calculations of chain statistics in confined environments and their exact dependencies on molecular weight.

Keywords

Thin films , glass transition, water waves, wave resistance.